Holographic Wavefront Characterization of a
Frequency-Tripled High-Peak-Power Neodymium:
Glass Laser (Master's Thesis)

Terrance Jude Kessler

HOLOGRAPHIC WAVEFRONT CHARACTERIZATION OF A FREQUENCY-TRIPLED

HIGH-PEAK-POWER NEODYMIUM:GLASS LASER

by

Terrance Jude Kessler

Submitted in Partial Fulfillment

of the

Requirements for the Degree

MASTER OF SCIENCE

Supervised by Professor James M. Forsyth

Institute of Optics

College of Engineering and Applied Science

The University of Rochester

Rochester, New York

1984

ACKNOWLEDGEMENTS

ABSTRACT

Near-field amplitude and phase distributions from a high-peak-power, frequency converted Nd:glass laser (λ = 351nm) have been holographically recorded on silver-halide emulsions. Conventionally, the absence of a suitable reference beam forces one to use some type of shearing interferometry to obtain phasefront information, while the near-field and far-field distributions are recorded as intensity profiles. In this study, a spatially filtered, locally generated reference beam was created to holographically store the complex amplitude distribution of the pulsed laser beam, while reconstruction of the original wavefront was achieved with a continuous-wave laser. Reconstructed near-field and quasi-far-field intensity distributions closely resembled those obtained from conventional techniques, and accurate phasefront reconstruction was achieved. Furthermore, several two-beam interferometric techniques, not practicable with a high-peak-power laser, have been successfully implemented on a continuous-wave reconstruction of the pulsed laser beam.

TABLE OF CONTENTS

LIST OF FIGURES

LIST OF TABLES

INTRODUCTION

The high-peak-power neodymium, glass laser has been extensively developed, primarily for use as a laser driver in Inertial Confinement Fusion (ICF) research. Recent interest in shorter wavelength drivers by the ICF community has resulted in the efficient conversion of infrared radiation (λ = 1.054 μm) to the ultraviolet, third harmonic (λ =351 nm), by means of nonlinear frequency conversion with KDP crystals.[1]

Direct drive ICF, where the confinement time is between 100 ps and 1 ns, is achieved by irradiating spherical fuel pellets with a symmetrical array of overlapping laser beams, and requires a highly symmetric target implosion. A target irradiance uniformity of $\pm$ 1% is believed to be essential in obtaining a sufficiently symmetric fuel compression.[2] The uniformity of laser energy deposition on target has been analyzed using a spherical decomposition of the multibeam interference pattern.[3] The irradiation nonuniformities are understood in terms of two contributing factors from the laser driver. The first factor involves the multibeam geometry, i.e., the number of beams and their orientation, and the energy balance between beams. The second factor involves both the F-number of the focussing lenses and the energy deposition pattern from a single beam, which is determined by the intensity profile of each beam at it's area of contact with the target surface. Therefore, in addition to high peak powers, direct drive ICF requires

that each frequency converted laser beam have a high level of uniformity at the target plane.

Central to the uniformity issue is the need to determine the factors which control the quasi-far-field intensity distribution of the individual beam, and the extent to which they can be manipulated to optimize overall irradiation uniformity. Wavefront measurement techniques, which generate near-field intensity and phase distributions, as well as quasi-far-field intensity distributions of individual laser beams, are essential in fulfilling these objectives. The two near-field profiles, together with a two-dimensional beam propagation code, would constitute a predictive tool for the calculation of the intensity distribution at any given target plane. Furthermore, experimental corroboration would be made possible by the existence of a real time reproduction of the pulsed beam. Figure 1-1 schematically illustrates the relationship between the propagation code predictions and a holographically reconstructed far-field intensity distribution.

Near-field and quasi-far-field intensity distributions, of an infrared (λ = 1.054 μm) high peak power laser (HPPL) beam, have been photographically recorded, while the phase distribution has been measured with shearing interferometry.[2,4] However, photographically recorded focal plane profiles are often invalid (section 2.3), and limited success has been achieved in quantitatively utilizing shearing interferograms. Furthermore, no wavefront measurement techniques have been successfully implemented on the frequency converted HPPL beam (λ = 351 nm).

Wavefront Measurement

Recorded Wavefront
(Hologram)

CW Reconstruction

Near Field
Intensity

Phase

Electronic Detection and Image Processing

Propagation
Code

Far Field
Intensity
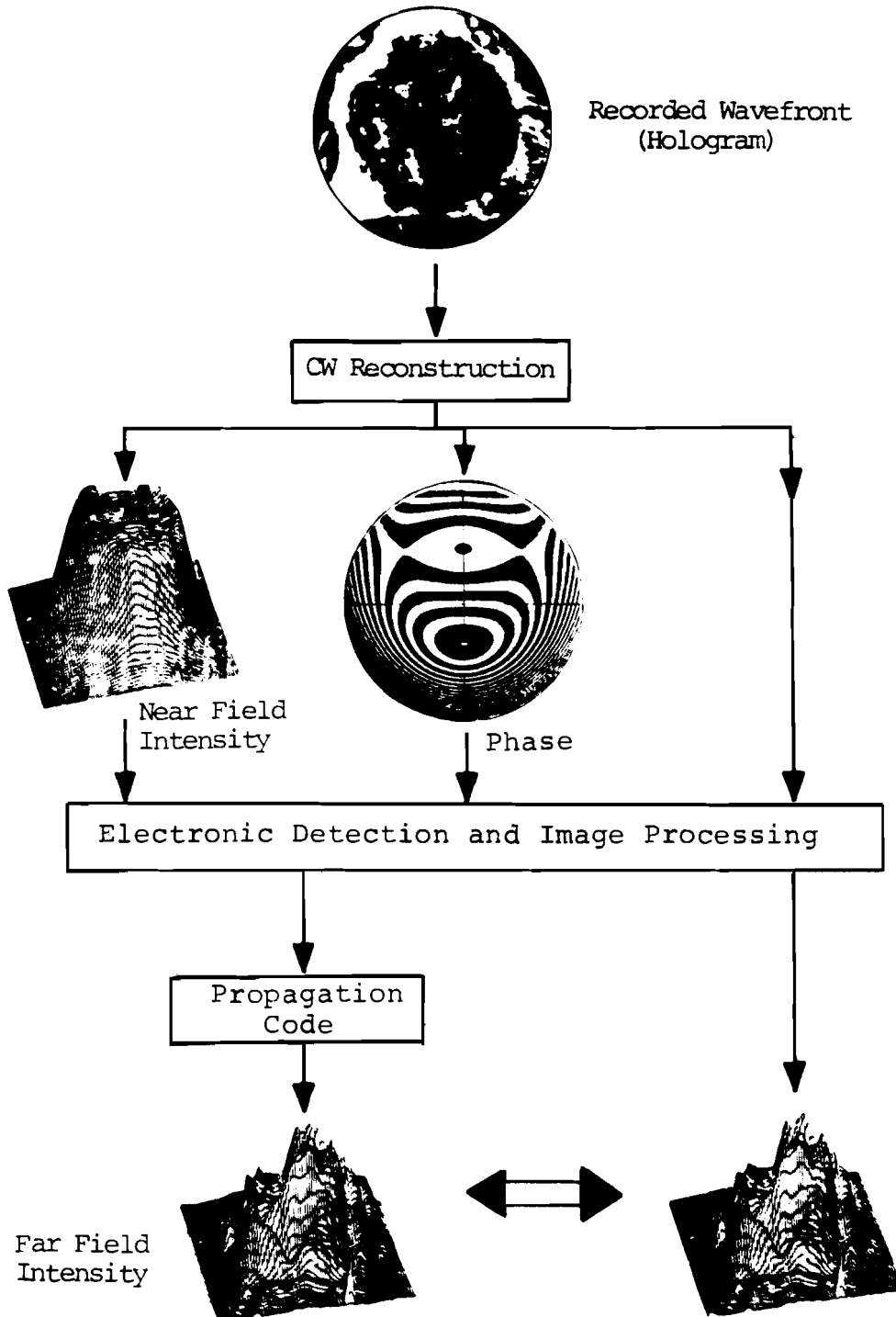
FIGURE 1-1

This thesis is based on the proposition that holographic methods can be implemented on an ultraviolet, frequency converted, high-peak-power laser, in order to obtain a reliable continuous-wave reconstruction for conventional wavefront measurement. Chapter II presents a description of the conventional and alternative wavefront measurement techniques. Chapter III contains a theoretical investigation of the feasibility of producing a locally generated reference beam, for use in holographically recording the wavefront of a HPPL. The demonstration of holographic techniques, and the application of conventional measurement techniques to both the pulsed laser beam and the continuous-wave reconstruction of the pulsed beam are contained in Chapter IV. Conclusions and suggestions for future research compose the final chapter.

REFERENCES

1) Seka W., Soures J.M., Jacobs S., Lund L., Craxton R.S.,
    "GDL: A High Power .35 um Laser", IEEE-J. of Q.E.,
    Sept.'81, Vol. Q.E.-17, #9, p.1689

2) LLE Review, "Uniformity Requirements for Direct Drive
    Laser Fusion", July'82-Sept.'82, Vol. 12,p.5

3) Skupsky S., Lee K., "Uniformity of Energy Deposition for
    Laser Driven Fusion", J.Applied Physics, 54(7), July'83
    p.3662

4) LLE Review, "Beam Uniformity Measurements on the OMEGA
    Laser", April'81-June'81, Vol.7,p.5

II. WAVEFRONT MEASUREMENT ALTERNATIVES

2.1 Introduction

A review of the previously used methods to measure the complex amplitude distribution in the near-field and the far-field intensity distribution of a high-peak-power laser (HPPL) is useful in establishing the many practical considerations which influence the final choice of a particular technique. The simplicity of design, operation, and interpretation as well as the versatility, accuracy and cost of the technique must be considered. This review begins with a general inquiry into the pulsed laser wavefront measurement alternatives, which includes useful techniques which have not yet been considered for the set of laser beam parameters (wavelength, pulsewidth, power, etc.) under investigation.

2.2 Phase Measurement

The Lateral Shearing Interferometer (LSI) has been an important tool in the phasefront measurement of the HPPL. This method involves the interference of two identical, but displaced, wavefronts which are derived from, and identical to, the original wavefront. The primary advantage is the fact that the wavefront is interfered with itself, thus eliminating the need for a separate reference wavefront. Figure 2.1 schematically illustrates the physical shear that occurs. The amplitude division of the incident wavefront can be obtained by means of reflecting surfaces, as utilized by the Murty, Bates, and Jamin Interferometers,[1] or by dif-

LATERAL SHEARING
INTERFEROMETER
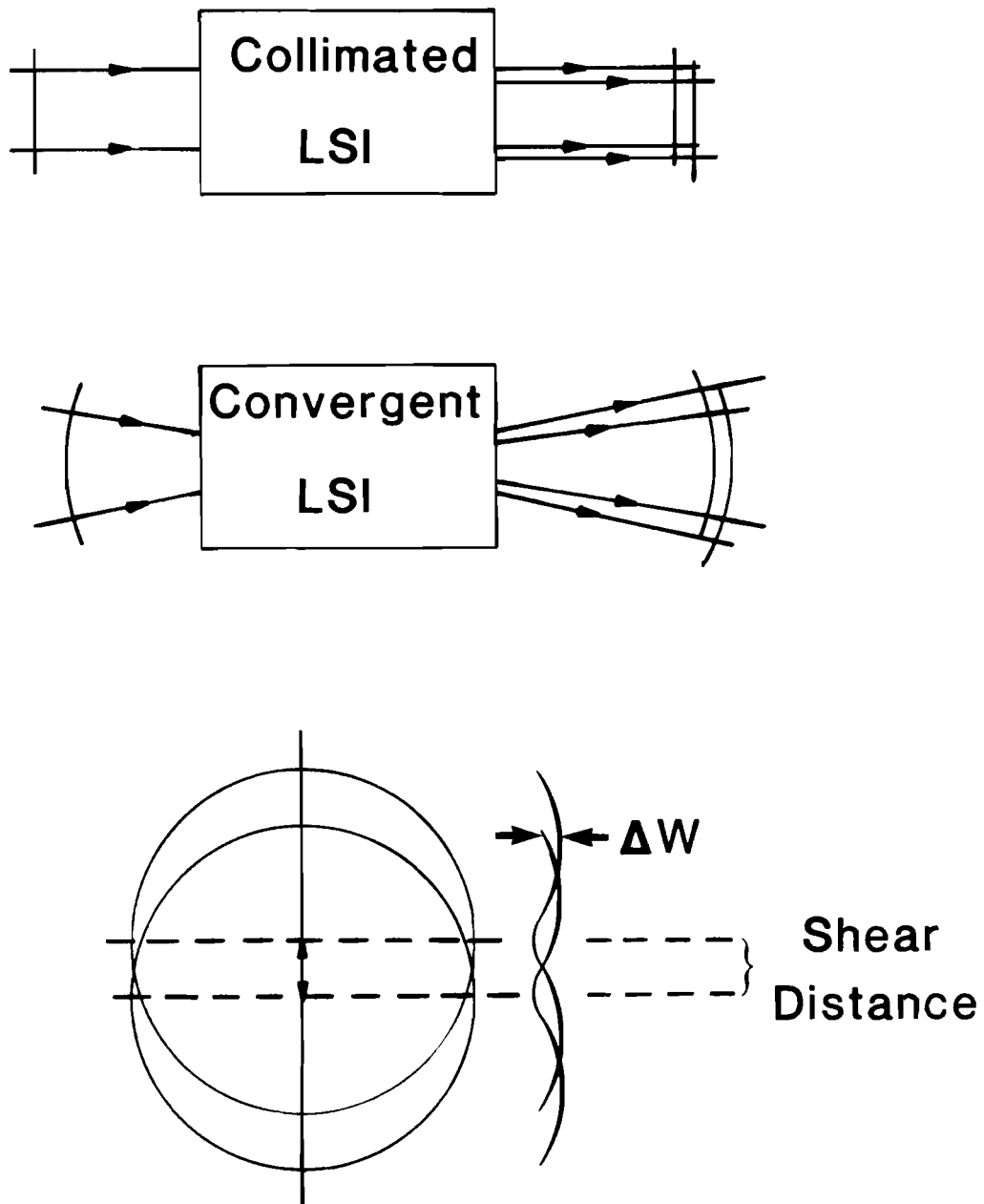
FIGURE 2-1

fraction, as utilized by the double frequency grating lateral shear interferometer.[2]

Referring to Fig. 2.1, the phasefront distribution can be expressed as $W(x,y)$, where x,y are the coordinates of point $P(x,y)$. A shear, $S = \Delta x$, between the two wavefronts introduces a path difference ΔW at point $P(x,y)$ such that $\Delta W(x,y) = [W(x+S/2,y)-W(x-S/2,y)]$. Neglecting constant phase shifts between the two wavefronts, a bright fringe is obtained whenever ΔW is an integer multiple of λ, where ΔW is the average of the wavefront slope ($\partial W/\partial x$) times the shear distance

$$\left.\frac{\partial W(x,y)}{\partial x}\right|_{\substack{\text{averaged} \\ \text{over } S}} (S) \quad = \quad n\lambda \tag{2-1}$$

The fringes of the lateral shear interferogram represent loci of constant wavefront slope, averaged over the shear distance.[3] The recovery of $W(x,y)$ is improved by a knowledge of the wavefront slope in two orthogonal directions, unless rotational symmetry is assumed. A second interferogram, where the shear direction is along the y axis, must be obtained in this case.

Given a nominally collimated wavefront, the Murty plane parallel plate interferometer (see Fig. 2.2) is a relatively simple method of acquiring wavefront slope information. The two interfering wavefronts are composed of front and rear surface reflections which are sheared according to the following equation,

MURTY INTERFEROMETER
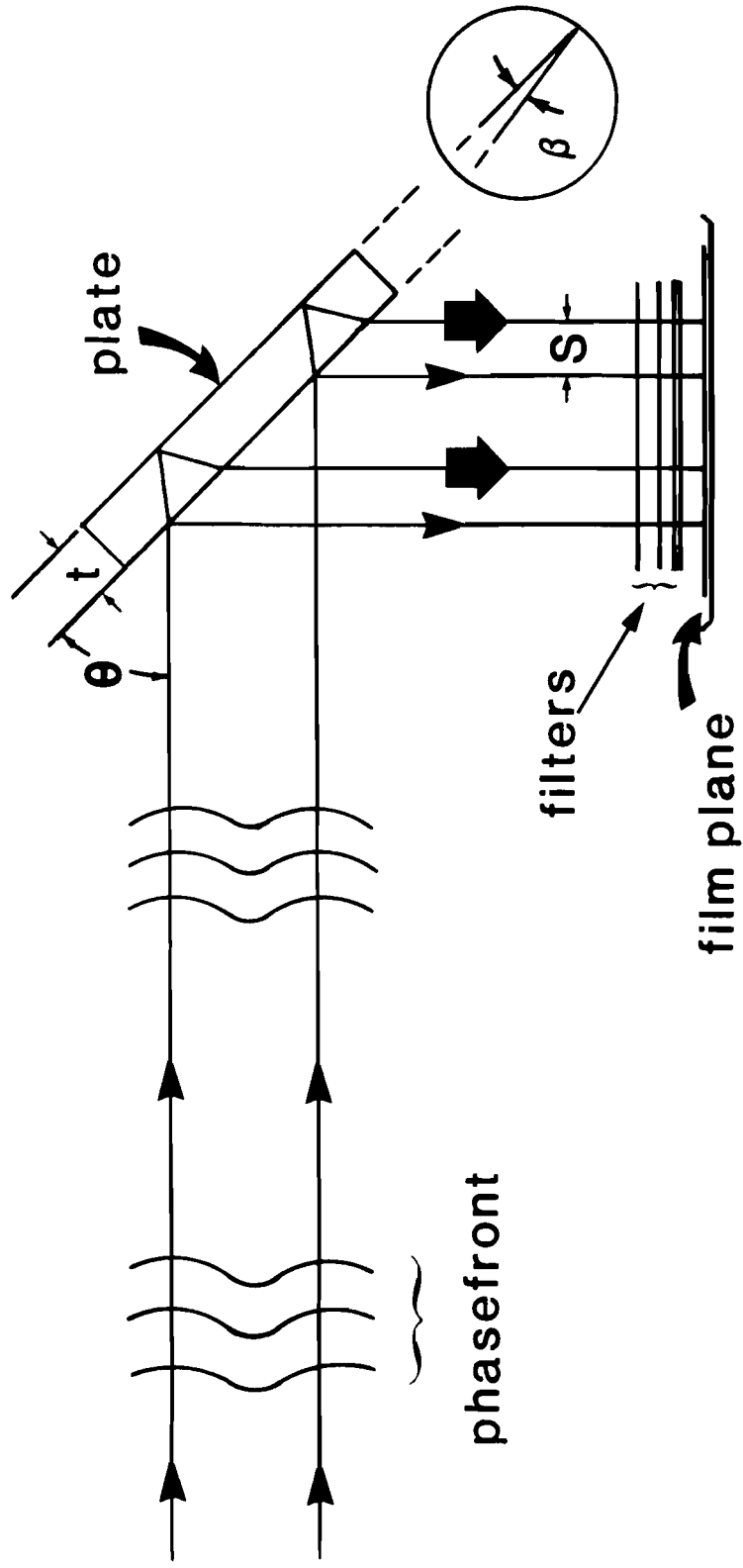
FIGURE 2-2

$$S = \frac{(t)\sin(2\theta)}{(n^2 - \sin^2\theta)^{\frac{1}{2}}} \qquad (2-2)$$

were t is the plate thickness, n is the refractive index and θ is the angle of incidence. The corresponding optical path difference between the two wavefronts is given by,

$$OPD = 2t(n^2 - \sin^2\theta)^{\frac{1}{2}} \qquad (2-3)$$

For an uncoated plate, the magnitudes of the two reflections are equal, and determined by the Fresnel reflection coefficients, thus insuring high fringe visibility for a sufficiently coherent source. The sensitivity is dependent upon the shear distance and any tilt introduced between the two reflecting surfaces. Generally tilt is introduced in the direction orthogonal to that of the lateral shear. In the case of shear in the x direction, the optical path difference associated with the tilt may be represented as a linear function of the y coordinate,

$$\Delta W = Ay = n\lambda \qquad (2-4)$$

where A is the tilt angle, λ is the wavelength of light and n is the refractive index. In the absence of any aberrations, this equation represents a system of straight fringes parallel to the x axis.

In the case of a wavefront with large, multiple aberrations, any tilt would further complicate analysis. A wavefront which is roughly charac-

terized, and known to have small aberrations of a particular type, requires tilt fringes for interferometric reduction since it is easier to evaluate the modulation of nominally straight fringes than to evaluate an almost complete absence of fringes.

Several methods of obtaining two orthogonal wavefront slopes are available. A single plate can be used in two different orientations if the wavefront in two consecutive experiments is reproducible. The use of two plates, orthogonally oriented, is a more expensive solution when simultaneity is a requirement. The double frequency grating is another solution; two shears are obtained by one holographic, double frequency, crossed, diffraction grating. The amount of shear is determined by the difference between the two spatial frequencies which make up the crossed grating. An important advantage to this technique, as opposed to the Murty interferometer, is that no optical path difference (time differential) between the sheared wavefronts exists. Therefore, any temporal incoherence effects in a pulsed beam will not blur the fringe pattern. Fringe blurring would be attributable to time dependent phase changes during the pulse, since a photographic recording device time-integrates the interference pattern.

Shearing interferometry has an inherent disadvantage over conventional wavefront interferometry because of the amount of analysis required to obtain the original wavefront. The most common analytical procedure assumes that the unknown wavefront $W(x,y)$ is a smooth function that can be represented by a two dimensional polynominal. The polynomial coefficients are calculated using a least squares fitting of the wavefront slope values obtained from the measurement of the fringe positions. Rimmer and Wyant state that the accuracy of the final results can

be as good as the accuracy of the measured data.[4] They point out that the major sources of error in their results are the measurement of the shear value and the polynomial fit to the data. They claim an error as small as .04 wavelength RMS has been obtained in the measurement of a wavefront with about one wavelength of aberration. However, an actual attempt at analyzing the data obtained from a HPPL points out the practical difficulties and enormity of the task.[5]

Figures 2.2 and 2.3 schematically illustrate the type of set up that each method requires for use on a HPPL. The Murty design utilizes a combination of wedged reflectors and attenuating filters to insure proper exposure of the photographic record. Figures 2.3 shows the actual setup used to obtain grating-shearing interferograms on an infra-red HPPL. By placing the grating near the focus of the lens system, lateral shearing interferograms are produced on either side of the zero order and in two orthogonal directions. An obstruction which blocked the zero order light was placed ahead of the final lens, to preserve the fringe visibility in the $\pm$ 1 diffracted orders. High visibility interference fringes were obtained on one beam from a twenty-four beam laser system (OMEGA) on a regular basis, but high power densities on the holographic grating resulted in occasional damage.[6] Although the results offered increased understanding of the beam performance in the focal spot as a function of the aberrations in the beam, an accurate analysis of the fringes was never completed.

The point diffraction interferometer (PDI)[7,8] is another potential tool for use on the HPPL. The PDI is basically a two-beam, common-path interferometer in which the reference beam is generated by the diffraction from a small aperture in a partially transmitting material. The

DOUBLE FREQUENCY GRATING
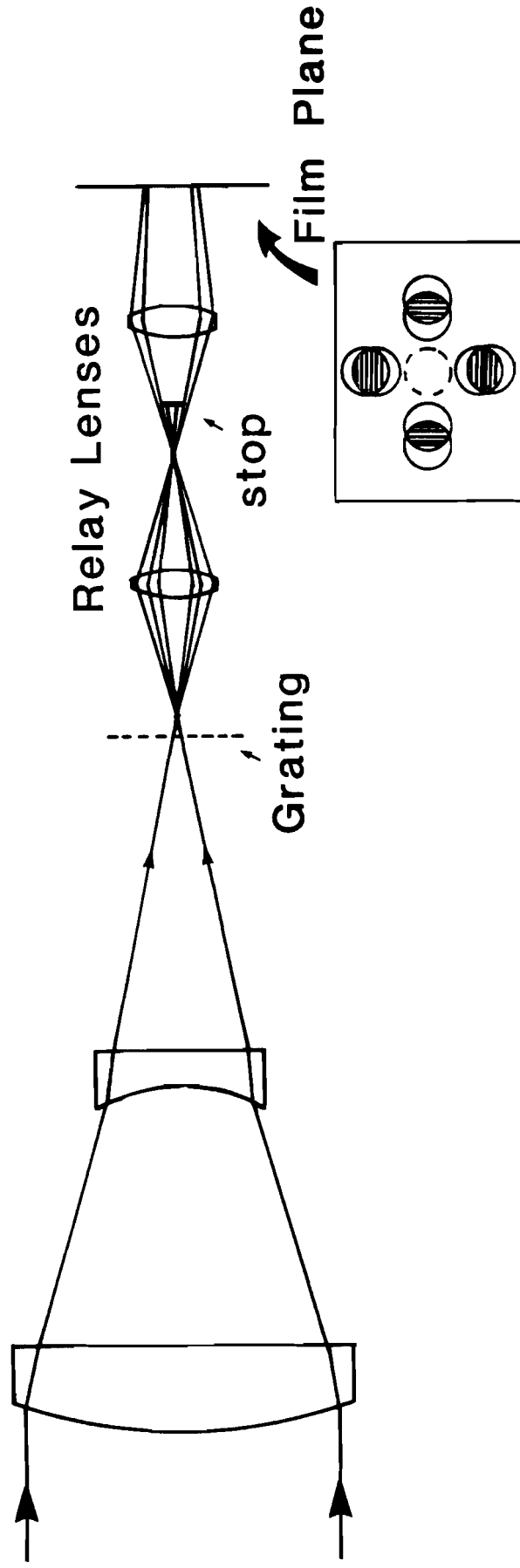
FIGURE 2-3

material, either a thin film deposited on a substrate, or a bulk absorption plate, is placed at the Fourier transform plane of a focussed wavefront as shown in Fig. 2.4. The pinhole is positioned so that some portion of the aberrated point spread function of the wavefront is diffracted into a perfect spherical wave reference beam. The attenuation coefficient of the material is chosen so that high visibility fringes result from the interference of the two wavefronts. The fringe quantity and shape can be chosen by adding or substracting tilt and defocus by laterally and logitudinally displacing the PDI, respectively. The disadvantage of the PDI is that these adjustments also affect the fringe visibility since the reference beam depends upon the intensity distribution of the aberrated point spread function. Unlike lateral shearing interferometry, the fringes from a PDI interferogram trace out contours of regions of equal optical path difference. A map of the wavefront phase is obtained directly.

An infra-red Smartt Interferometer has been successfully designed and used to measure the phase of a CO_2 HPPL.[9] High power densities exclude any type of interferometer which focusses the light onto a coated surface, since a vaporization of the thin film coating, used to attenuate the wavefront, usually occurs. This new design utilized a substrate consisting of a 13 micron thick, epitaxially grown, silicon section into which a high conductivity n-type dopant is driven in by means of a diffusion process. To avoid high power densities on the surface, high F/# systems were used in conjunction with a 40 micron diffraction aperture, along with an initial attenuation of the full beam. The trade offs were found to be between the choice of aperture size and wavefront attenuation versus the contrast and accuracy of the fringes. A peak to valley error of $\lambda/20$ was obtained (λ =10.6 μm).

POINT DIFFRACTION INTERFEROMETER
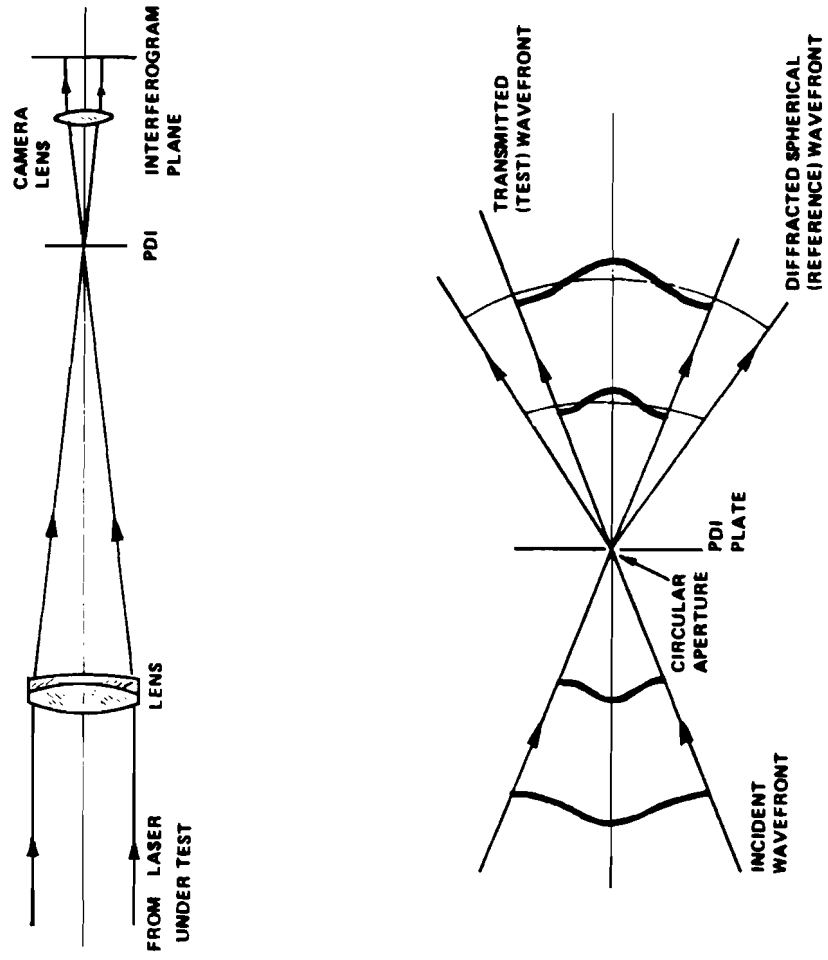
FIGURE 2-4

A variation of the Mach-Zehnder Interferometer has been used to measure the beam parameters of a continous-wave HeNe gas laser.[10] In Fig. 2.5, a TEM_{00} mode laser beam is used as a signal beam. A reference beam is obtained by enlarging the signal beam sufficiently to produce a plane wave with uniform amplitude. Direct measurements of the resulting interferogram and intensity distribution were made to obtain beam parameters.

Holographic techniques allow the possibility of recording and subsequently reconstructing the amplitude and phase of a wavefront. Conventional holographic interferometry involves the storage of two or more temporally separated wavefronts, and an interferometric comparison between them is made during reconstruction. Alternately, the wavefront reconstructed by diffraction at the hologram can be made to interfere with another wavefront transmitted through the hologram. In this case, real time, two-beam type fringes are obtained. Generally this is applied to vibrational analysis or mechanical stress measurement, where the two interfering wavefronts are both object wavefronts and time dependent phase changes are studied. When a plane wave is used as the interfering wavefront transmitted through the plate, then the phase of the object wavefront itself can be visualized in terms of two-beam interference fringes. A hologram of a pulsed laser can be recorded with a locally generated reference beam from the pulse itself.[11,12] The object wavefront can be subsequently reconstructed with an appropriate continous wave laser. Like the PDI, this interferometric technique directly produces wavefront information.

MACH–ZEHNDER INTERFEROMETER

Reference beam

Recording Plane

CW HeNe
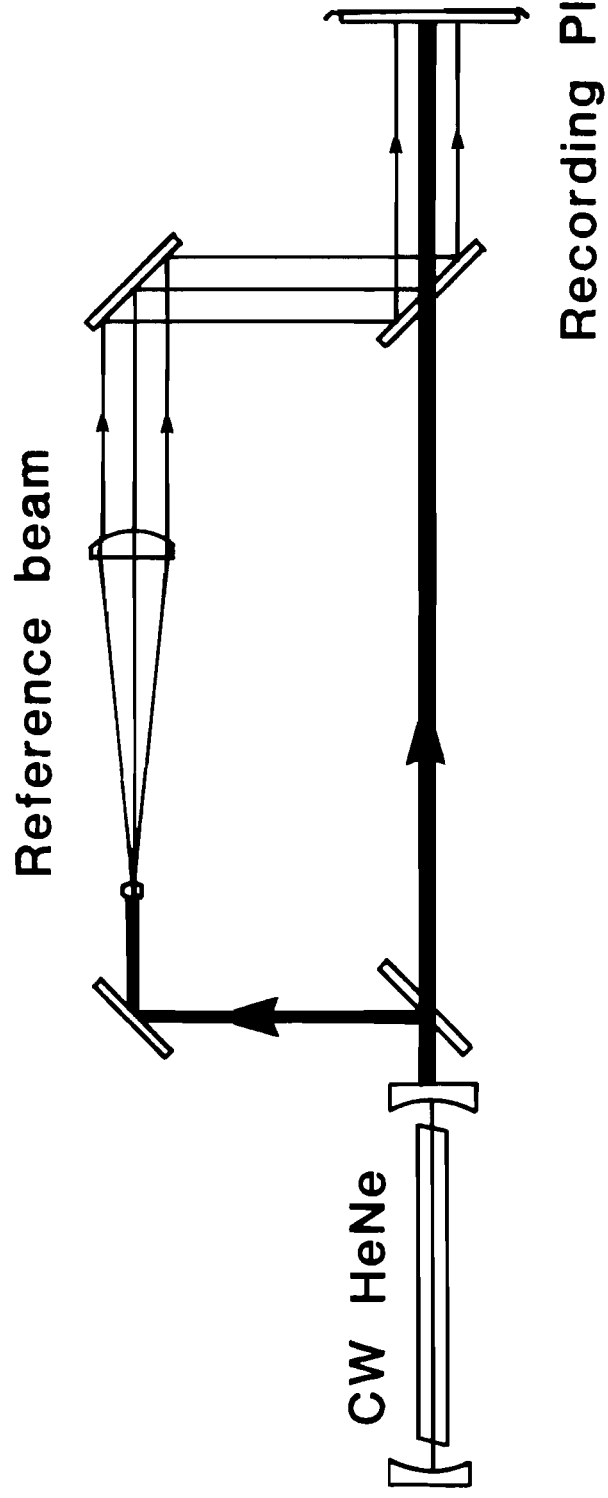
FIGURE 2-5

2.3 Intensity Measurement

Many techniques are available in recording the near-field intensity distribution of a HPPL. The major design parameters are the wavelength sensitivity, resolution, and dynamic range of the recording medium. Kodak Linagraph direct print paper, Polaroid high speed black and white film, and Dupont Dylux Instant Image Proof Paper[13] are commonly used to diagnose errors in beam alignment, but their low resolution and low dynamic range preclude accurate sensitometric analysis. Solid impressions of the intensity profile, formed in thermally deformable plastics, are used as diagnostic tools for high average power lasers. When the demagnification of a large diameter beam is possible, image tubes and detector arrays are available recording devices.

The photographic method is possibly the best near-field intensity recording technique. The wavelength sensitivity ranges from being adequate in the near infrared to overly responsive at ultraviolet wavelengths. The dynamic range can vary from less than two orders of magnitude to more than three orders of magnitude, depending on the type of emulsion and the selected slope (gamma) of the density verses logarithm of the exposure (D-logE) curve. Lack of resolution rarely presents a problem for large diameter HPPL beams. Accurate intensity values are obtained by generating D-log(E) curves for each combination of wavelength, pulsewidth, and development procedure.

Photographic methods are also available for the recording of far-field and equivalent-target-plane (ETP) intensity distributions. The equivalent plane camera produces a two-dimensional array of successive quasi-far-field images, each with a set of decreasing exposure levels.[14] Figure 2.6 illustrates the set-up necessary to obtain the

2-DIMENSIONAL ARRAY CAMERA
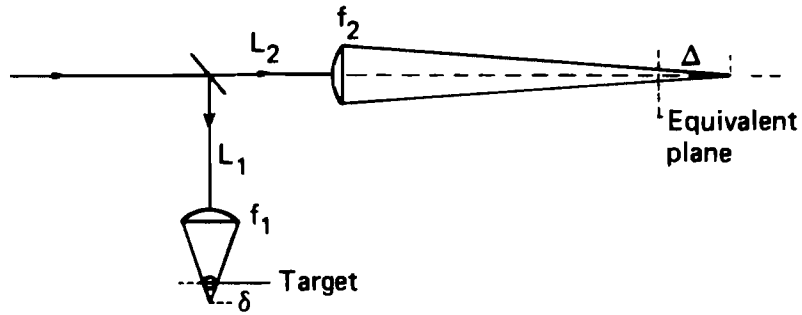
$$\Delta = \frac{f_2{}^2 \delta}{f_1{}^2 - (L_2 - L_1) \delta + (f_2 - f_1) \delta}$$
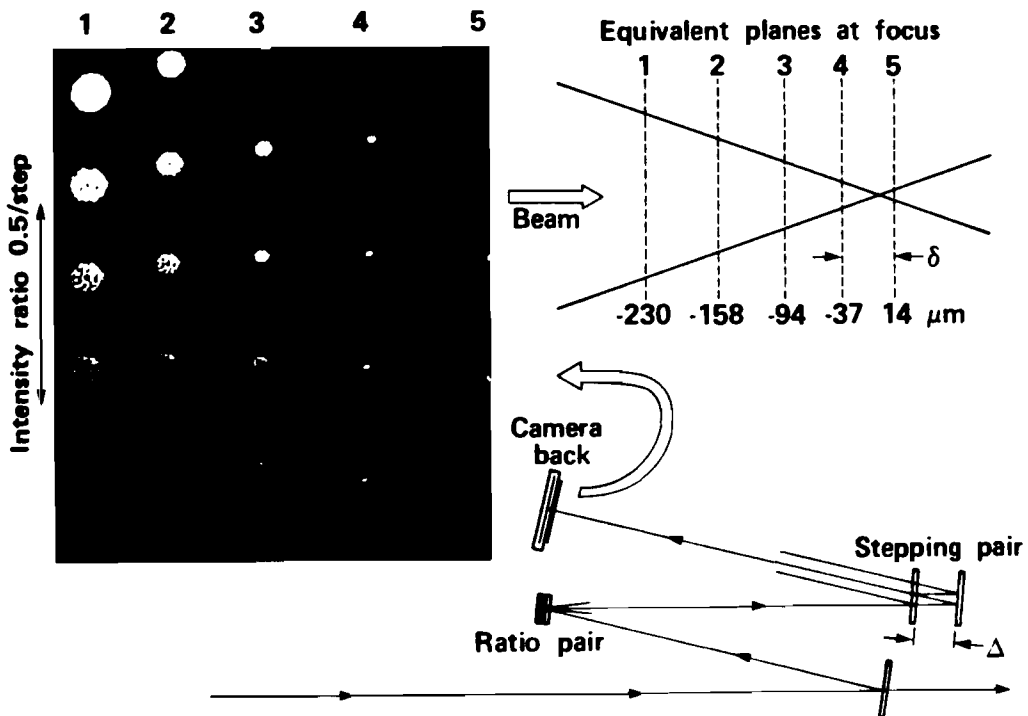
FIGURE 2-6

array. An energy reduction in the beam, along with the use of a long focal length lens, delivers the correct energy density to the film plane. Attenuating and narrow pass blocking filters are placed just before the film plane. All optics prior to the camera must be diffraction limited in quality, while the filters need only be locally homogeneous and uniformly transmitting.

It is generally accepted that ETP photographic methods are accurate when the plane is sufficiently removed from the focal plane. However, these methods can give misleading results and errors in energy density determinations when used near the focal plane of the lens.[15] If the intensity distribution has a spike in the center with broad wings of intensity below the film threshold, then this method yields a smaller than true image size. This is actually a problem of limited dynamic range and can apply to electronic detection as well. The array camera can offer a way to determine the extent of this problem for a given wavefront. By allowing the first few row elements of each focal column to be overexposed, large changes in image size due to this effect could be observed, and would indicate that the recording plane is too near focus for an accurate energy density calculation.

Pinhole methods were developed as a means of more accurately determining focal plane intensity distributions.[16] A single aperture is translated through a matrix of positions within the focal plane. A detector behind the aperture measures the energy of each laser pulse, one pulse per matrix element. The requirement of simultaneous measurements led to the development of pinhole methods that utilize the multiple side orders of a diffraction grating.[17]

Image tubes and detector arrays are available for single shot measurement of far-field intensity distributions. The vidicon tube has been used to image a CO_2 HPPL off diffusing surfaces.[18] The low resolution of 15 lines/mm and a dynamic range of less than two orders of magnitude make the vidicon tube inadequate for accurate measurements. Other image tubes with better performance are available but have not been tested on a HPPL.[19]

Pyroelectric arrays offer many advantages to wavefront measurement. (Pyroelectricity is the phenomenon by which crystals convert changes in temperature to electricity.[20]) Their flat spectral response and wide dynamic range make them an excellent choice of detector. The disadvantages include both a limited resolution and relatively high expense.

The CID (Charge Injection Device) imaging array offers superior resolution as well as a dynamic range of greater than five orders of magnitude.[21] The two-dimensional array consists of coupled metal-oxide silicon (MOS) capacitors which collect and store the photogenerated charge. Coincident X-Y selection is used to inject the stored charge into the bulk silicon. The output signal is related to the time integrated charging current to the MOS capacitor plates. The major disadvantage is system expense and, like the pyroelectric array, an accidental excess of energy, beyond the damage threshold of the material, results in costly repairs.

2.4 Conclusions

A technique which inherently can produce the far-field and near-field intensity distributions, as well as the near-field phase distribution of a HPPL most deserves investigation. The basic design of a system that has this capability is shown in Fig. 2.7.

The heart of this system is a holographic interferometer. The incident wavefront is split into an object beam and a newly created reference beam. Several techniques can be employed to create a suitable reference beam, which are discussed in Chapter Three. The two beams recombine at the holographic plate to form an interference pattern that is characteristic of both the object and the reference beams. A CW laser, operating at the same wavelength, can be used with the same set-up to reconstruct the object wavefront. This design takes advantage of the fact that holographic interferometry is capable of recording all of the information necessary for the complete recovery of the original complex amplitude distribution.

Various wavefront measurement techniques, considered impractical for use on the HPPL, are possible with a CW reconstruction of the same HPPL wavefront. A near-field intensity pattern could be appropriately demagnified and observed with a detector array without the risk of costly damages. The propagation of a CW plane wave along the path of the initial object beam would produce two beam inteferometric fringes, characteristic of the original phasefront. Furthermore, a typical PDI, designed for use with a CW laser, could be used in place of the separate-plane-wave reference scheme to allow the phasefront measurement to include the performance of the final focussing lens. While the reconstructed wavefront is still focussed through the lens, the PDI could be removed to observe a continuum of ETP images, and the far-field intensity

HOLOGRAPHIC INTERFEROMETER

Reconstruction

Hologram

ϵ

reference beam

CW laser
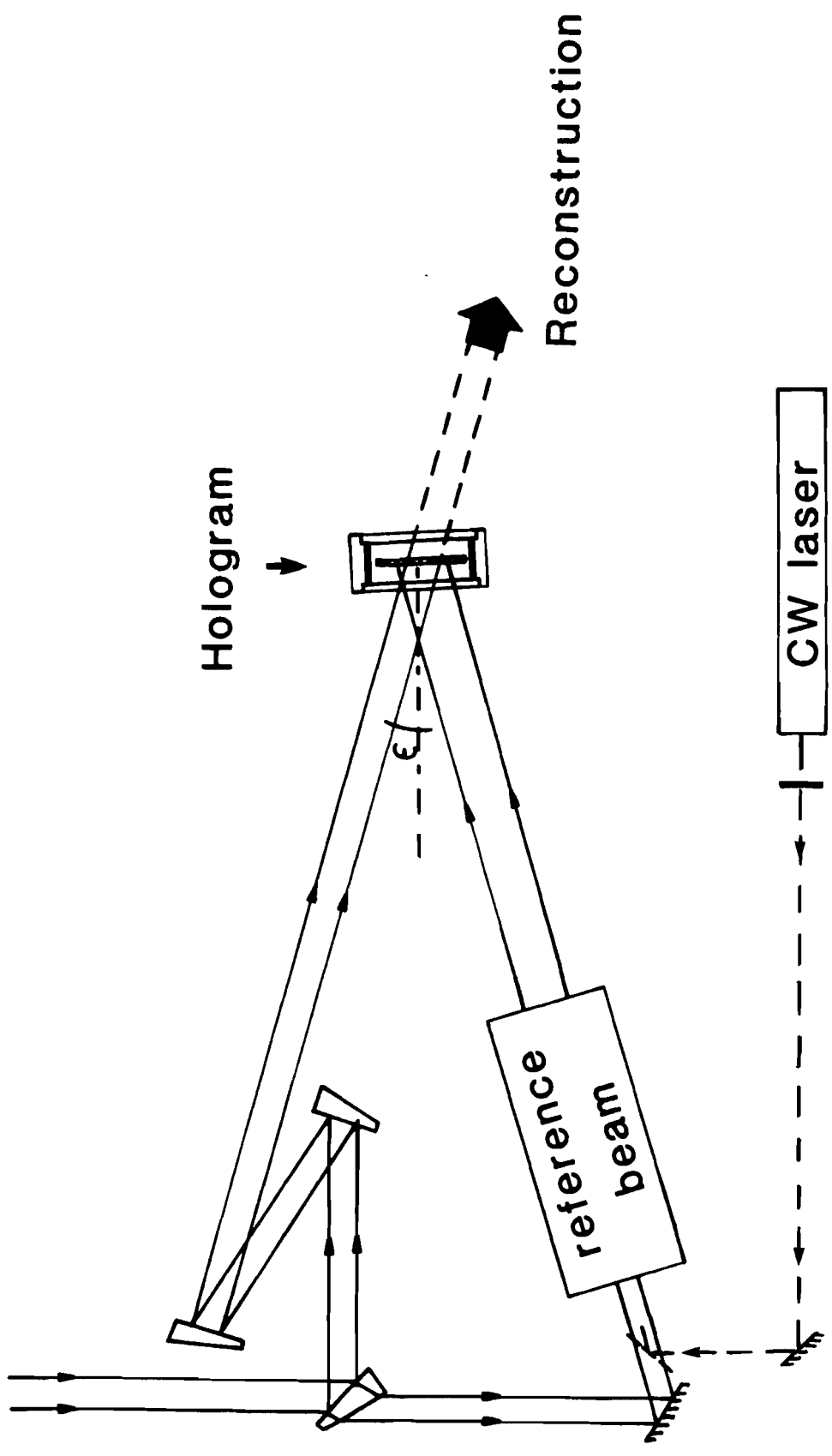
FIGURE 2-7

pattern could be mapped out over a curved surface corresponding to a spherical target. Additionally, this technique could reduce the difficulty associated with measuring the intensity distribution right at the focal plane.

Alternatively, phase measurements could be obtained without the use of an interferometer. A technique which utilizes acousto-optic modulation, heterodyne detection, and two-dimensional raster scanning has been developed to characterize laser beam quality.[22] This technique offers the ability to simultaneously measure the two dimensional phase and intensity distributions of the CW reconstruction of the pulsed beam.

In summary, the holographic interferometer inherently offers total wavefront storage. Various wavefront measurement techniques are better suited to a CW reconstruction of the HPPL. This design merits investigation since it offers both interferometric and intensity measurement capabilities not presently available for HPPL beam analysis.

REFERENCES

1. D. Malacara, _Optical Shop Testing_, John Whiley and Sons Inc.,
    1978, p.105

2. J.C. Wyant, "Double Frequency Lateral Shear Interferometer",
    Applied Optics, Sept. 1973, p. 2057

3. J.C. Wyant, _Optical Testing and Testing Instrumentation_, The
    Institute of Optics Contemporary Optics Notes

4. M.P. Rimmer and J.C. Wyant, "Evaluation of Large Aberrations
    Using a Lateral-Shear Interferometer Having Variable Shear",
    Applied Optics, Jan. 1975, p. 142

5. R. Hopkins, _Laboratory for Laser Energetics_, Unpublished Internal
    Report, June 11, 1982

6. S. Kumpan, _Laboratory for Laser Energetics_, Preliminary Internal
    Report, June 5, 1981

7. W.P. Linnick,"A Simple Interferometer for the Investigation of
    Optical Systems", _C.R. Acad. Sci. URSS._, Vol. 5, p.210, 1933

8. R.N. Smartt and J. Strong, _Journal of Scientific Applications_,
    62, p. 737, 1972

9. V.K. Viswanathan, R.B. Hammond, I. Liberman, B.D. Seery, A. Gibbs
    and P.D. Bolen, _Los Alamos Conference in Optics_, April 1981

10. T. Miyamoto and K. Yasuura,"Measurements of Beam Parameters of a
    Laser Beam and its Diffraction Field, Using a Hologram",
    Applied Optics, Jan. 1971, p. 161

11. C. Roychoudhuri and B.J. Thompson,"Studying Beam Parameters of a
    Pulse Using Holography in Conjunction with Interferometry",
    Abstract Only, _JOSA_, 1972, p. 1357

12. H.J. Caufield, _Handbook of Optical Holography_, Academic Press,
    1979, p. 219

13. M.W. Taylor, J.Goldhar and J.R. Murray, "An Instant Image
    Photographic Material Suitable for Ultraviolet Laser Beam
    Intensity", _Lawrence Livermore Laboratory_, June 14,1981

REFERENCES(continued)

14. H.G. Ahlstrom, Physics of Laser Fusion, Vol.II, <u>Lawrence Livermore Laboratory</u>, Jan. 1982

15. P.J. Shayler, "Laser Beam Distribution in the Focal Region", <u>Applied Optics</u>, Sept., 1978, p. 2673

16. B.J. Brannon, et. al., "Laser Focal Spot Measurements", <u>Journal of Applied Physics</u>, Aug. 1975, p. 3576

17. R.W. O'Neil, et. al., "Beam Diagnostics for High Energy Pulsed CO_2 Lasers", <u>Applied Optics</u>, Feb, 1974, p. 314

18. S. Mersch, J.S. Harris and D.L. Mullen, "Imaging CO_2 High Energy Laser Pulses with a Pyroelectric Vidicon Camera", <u>Optical Engineering</u>, May/June 1981

19. R.C.A., <u>Electro-Optics Handbook</u>, 1974, p. 173

20. C.B. Roundy, "Pyroelectric Arrays Make Beam Imaging Easy", <u>Laser & Applications</u>, Jan. 1983

21. <u>General Electric</u>, "Solid State Video/Digital Camera", 1981

22. C.P. Wang, "A New Technique for Measuring Two-Dimensional Laser-Beam Phase and Intensity Profiles", <u>The Aerospace Corporation</u>, Nov. 1983

III. THEORETICAL CONSIDERATIONS

3.1 Introduction

Holography is a method of recording and reconstructing the complex amplitude of a wavefront. The interference pattern between an object wavefront and a coherent reference beam is recorded. The use of a silver halide emulsion as an energy recording medium requires chemical processing in order to manifest the wavefront modulation. Wavefront reconstruction takes place, in a third step, when the hologram is illuminated with a second reference wave. Under certain conditions, the reconstructed wavefront is identical in form to the original wavefront, and may be operated upon as if it were the original. Other radiation characteristics, such as spectral bandwidth, pulsewidth, and polarization are not preserved. This chapter deals with the theoretical concepts which outline the requirements for an accurate wavefront recording of a High Peak Power Laser (HPPL), and an accurate, continuous wave reconstruction of the same wavefront.

3.2   Wavefront Recording

Communication theory offers insight into the relationship between heterodyne techniques and general holographic methods. Expressions describing the interference and modulation between the object wave and the reference wave (local oscillator) offer a clear understanding of the effects due to temporal variations, and show the means by which the amplitude and relative phase information are preserved. The following notation follows closely to Cathey.[1] Let the object wave and local oscillator (LO) wave be represented, respectively, by

$$\text{(Object)} \qquad O(x,y)\cos[-\omega_1 t + \alpha x + \gamma z + \psi(x,y)] \qquad\qquad \text{(3-1)}$$

$$\text{(LO)} \qquad R(x,y)\cos[-\omega_2 t + \delta x + \mu z + \phi(x,y)] \qquad\qquad \text{(3-2)}$$

where $O(x,y)$, $\psi(x,y)$ and $R(x,y)$, $\phi(x,y)$ represent the amplitude and phase distribution pairs of the object and LO waves, respectively. Plane polarization along the y axis is tacitly assumed. The relationships between the incident angles, χ and θ, and the pairs of propagation constants, α, γ, and δ, μ, of the object wave and LO, respectively, are illustrated in Fig. 3-1. The lines represent surfaces of constant phase, called phasefronts. The temporal frequencies, ω_1 and ω_2 of the object and LO waves, respectively, have units of radians/second. Square law detection of the interference signal between these two waves would produce a signal described by:

RECORDING GEOMETRY

$$\alpha = k\sin(\chi)$$

$$\gamma = k\cos(\chi)$$

$$\delta = k\sin(\theta)$$

$$\mu = k\cos(\theta)$$
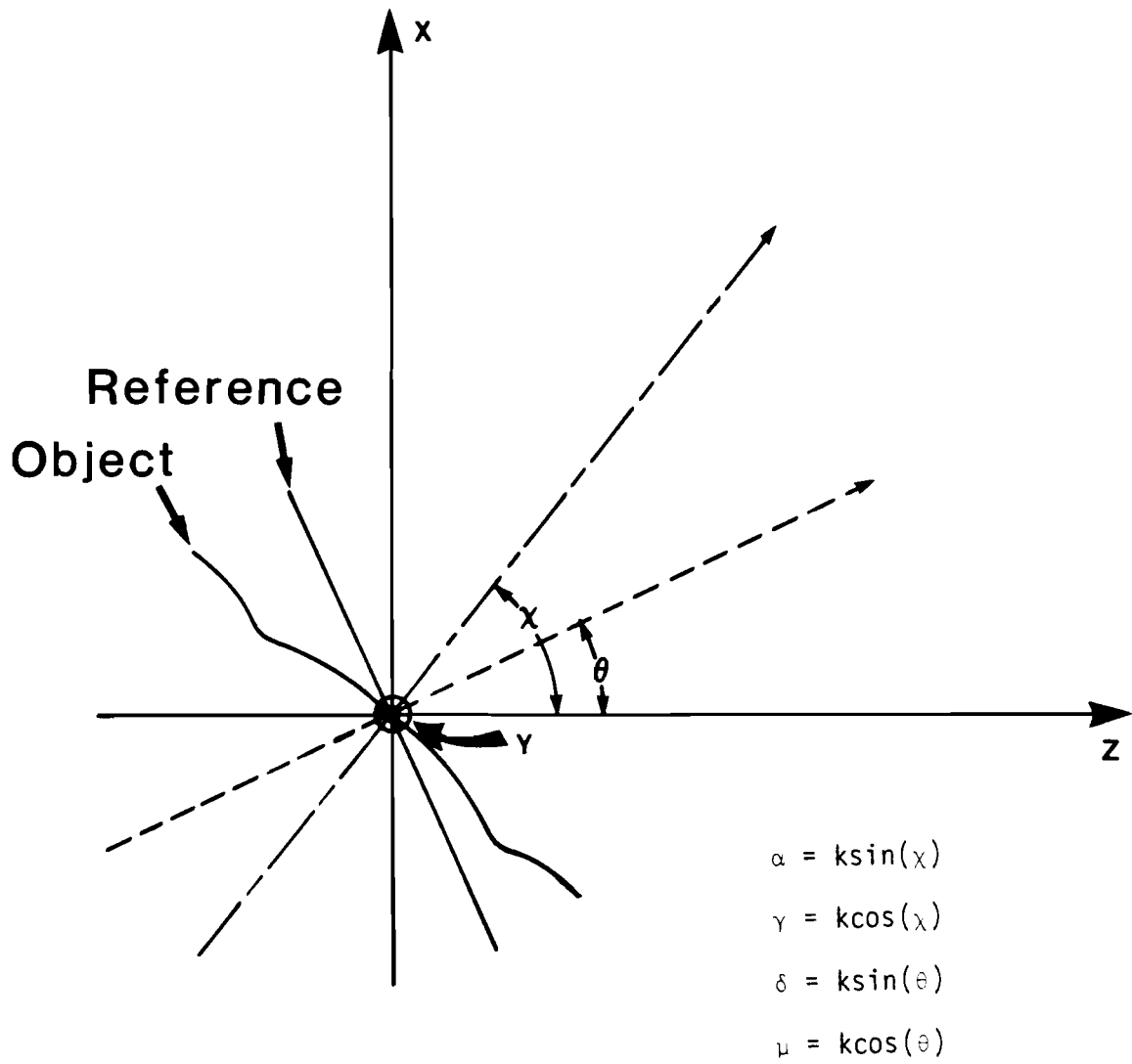
FIGURE 3-1

$$S(x,y,t) \propto 0^2(x,y)/2 + 0^2(x,y)\cos[-2\omega_1 t + 2\alpha x + 2\gamma z + \psi(x,y)]$$
$$+ R^2(x,y)/2 + R^2(x,y)\cos[-2\omega_2 t + 2\delta x + 2\mu z + \phi(x,y)]$$
$$+ 0(x,y)R(x,y)\cos[-(\omega_1+\omega_2)t + (\alpha+\delta)x + (\gamma+\mu)z + \psi(x,y) + \phi(x,y)]$$
$$+ 0(x,y)R(x,y)\cos[-(\omega_1-\omega_2)t + (\alpha-\delta)x + (\gamma-\mu)z + \psi(x,y) - \phi(x,y)]$$

$$(3-3)$$

The double frequency and sum frequency components vary too rapidly, for a detector with limited resolution and time response to record, leaving only the zero frequency and difference frequency terms,

$$S(x,y,t) \propto 0^2(x,y)/2 + R^2(x,y)/2 + 0(x,y)R(x,y) \cdot$$
$$\cos[-(\omega_1-\omega_2)t + (\alpha-\delta)x + (\gamma-\mu)z + \psi(x,y) + \phi(x,y)] \quad (3-4)$$

The original amplitudes and phases are linearly preserved in the cross terms. Heterodyning techniques utilize the intermediate frequency $\omega_{IF} = \omega_1 - \omega_2$ to reconstruct the object wave. Off-axis holographic methods utilize a spatial carrier frequency, and are referred to as Leith-Upatnieks holograms. Letting $\omega_1 = \omega_2$ and restricting the recording geometry to symmetrical illumination, $\theta = -\chi$, the expression becomes,

$$S(x,y) \propto 0^2(x,y)/2 + R^2(x,y)/2 + 0(x,y)R(x,y)\cos[2\alpha x + \psi(x,y) - \phi(x,y)]$$

$$(3-5)$$

Equation 3-5 shows that the amplitude distribution is recorded as an amplitude modulation of the spatial carrier frequency. The phase distribution is recorded as a phase modulation of the same carrier. A holographic recording of two nominally plane waves can be considered a modulated diffraction grating. The amplitude of the grating is influenced by the object amplitude, and the positions of the grating lines by the phase. Figure 3-2 illustrates each case, with 3-2a showing the sinusoidal variation of fringes due to the interference between two perfectly plane waves. If the object wave has only amplitude variations, such that $O(x,y) \neq$ constant and $\psi(x,y) =$ constant, then only the intensity of the fringes varies (Fig. 3-2b). A phase modulation of a wave, such as $O(x,y) =$ constant and $\psi(x,y) \neq 0$ causes a shift of the fringes and a change in their spacing (Fig. 3-2c).

Many materials are available to record and preserve the modulated wavefronts; dichromated gelatins, ferroelectric crystals, thermoplastics, photoresists, photochromic materials, and others are described in the literature. The most common medium, the silver halide emulsion, is discussed in most holographic references, and is well characterized by both the manufacturers and the scientific community. In the first phase of the holographic process, the wavefront information is recorded and preserved in the form of a latent image. The materialization of the wavefront modulation occurs during subsequent processing of the emulsion.

Development of the silver halide emulsion converts the latent image distribution to a metallic silver distribution, such that the macroscopic number density is proportional to the incident electric field squared. Referring to equation 3-5, we can describe the density distribution with the following equation,

MODULATED DIFFRACTION GRATING

TWO PLANE WAVE INTERFERENCE

3-2a

AMPLITUDE MODULATION

3-2b

PHASE MODULATION

3-2c
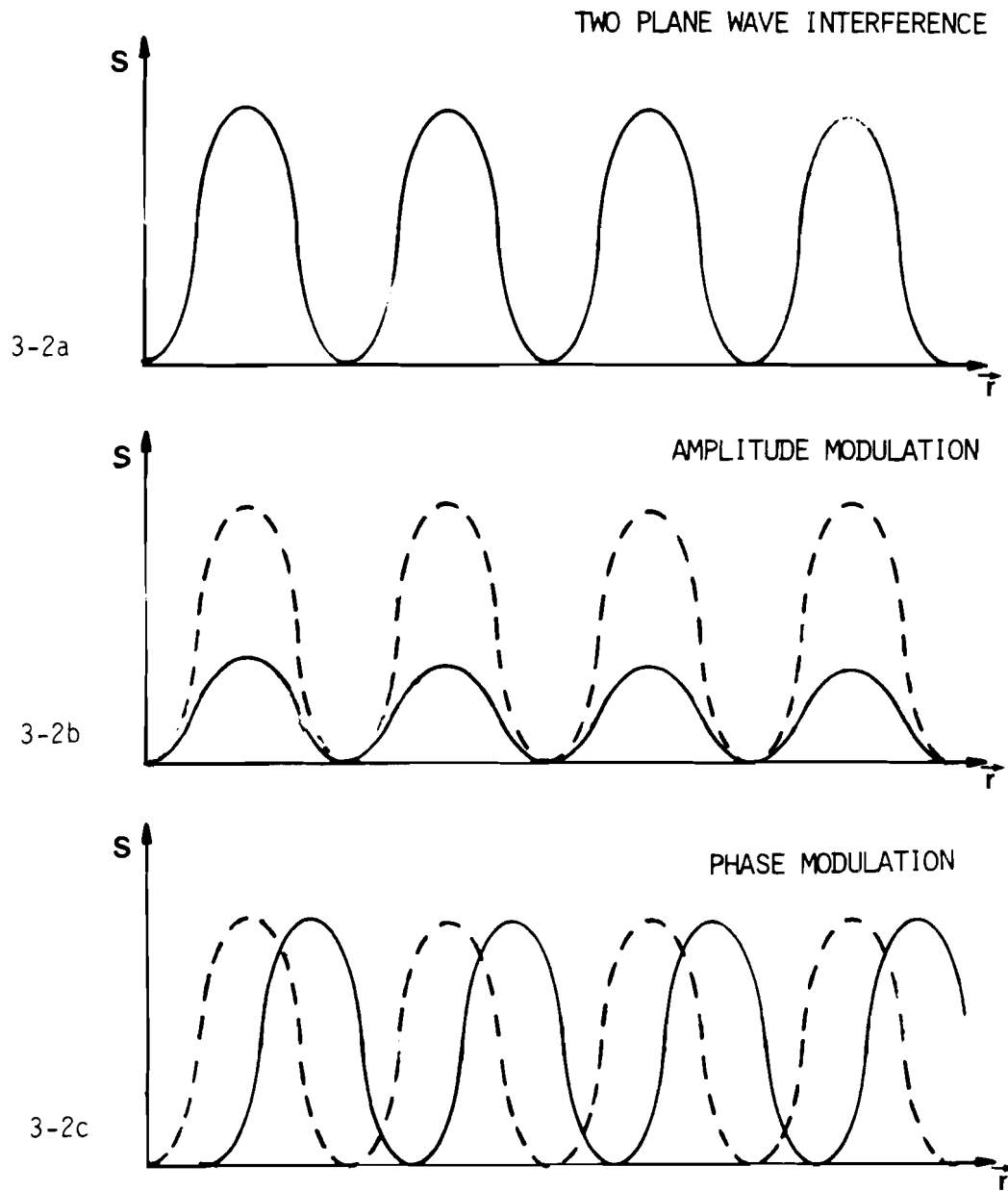
FIGURE 3-2

$$N(x,y) = N_0 + N_1 \cos[2\alpha x + \psi(x,y) - \phi(x,y)] \qquad (3\text{-}6)$$

Ideally, both the object and reference wavefronts are nearly plane waves, such that the difference between their phase distributions is a constant, i.e., $\psi(x,y) - \phi(x,y) = C$. For two plane waves we have,

$$N(x,y) = N_0 + N_1 \cos[2(k\sin\chi)x + C] \qquad (3\text{-}7)$$

where 2χ is the full angle between the plane waves. Planes of metallic silver appear after development as shown in Fig. 3-3. The equiphase planes satisfy the vector equation,

$$(\vec{k}_1 - \vec{k}_2) \cdot \Delta\vec{r} = 0 \qquad (3\text{-}8)$$

The planes are separated by a distance d, where d is given by the Bragg condition:

$$d = \frac{\lambda_0}{2\sin(\chi)} = \frac{\lambda_0/n}{2\sin(\chi')} \qquad (3\text{-}9)$$

As an example, let $\lambda = 351$ nanometers and $2\chi = 15°$. The spatial frequency, $\nu = 1/d$, of the planes along the x-axis is 744 cycles per millimeter.

METALLIC SILVER DISTRIBUTION
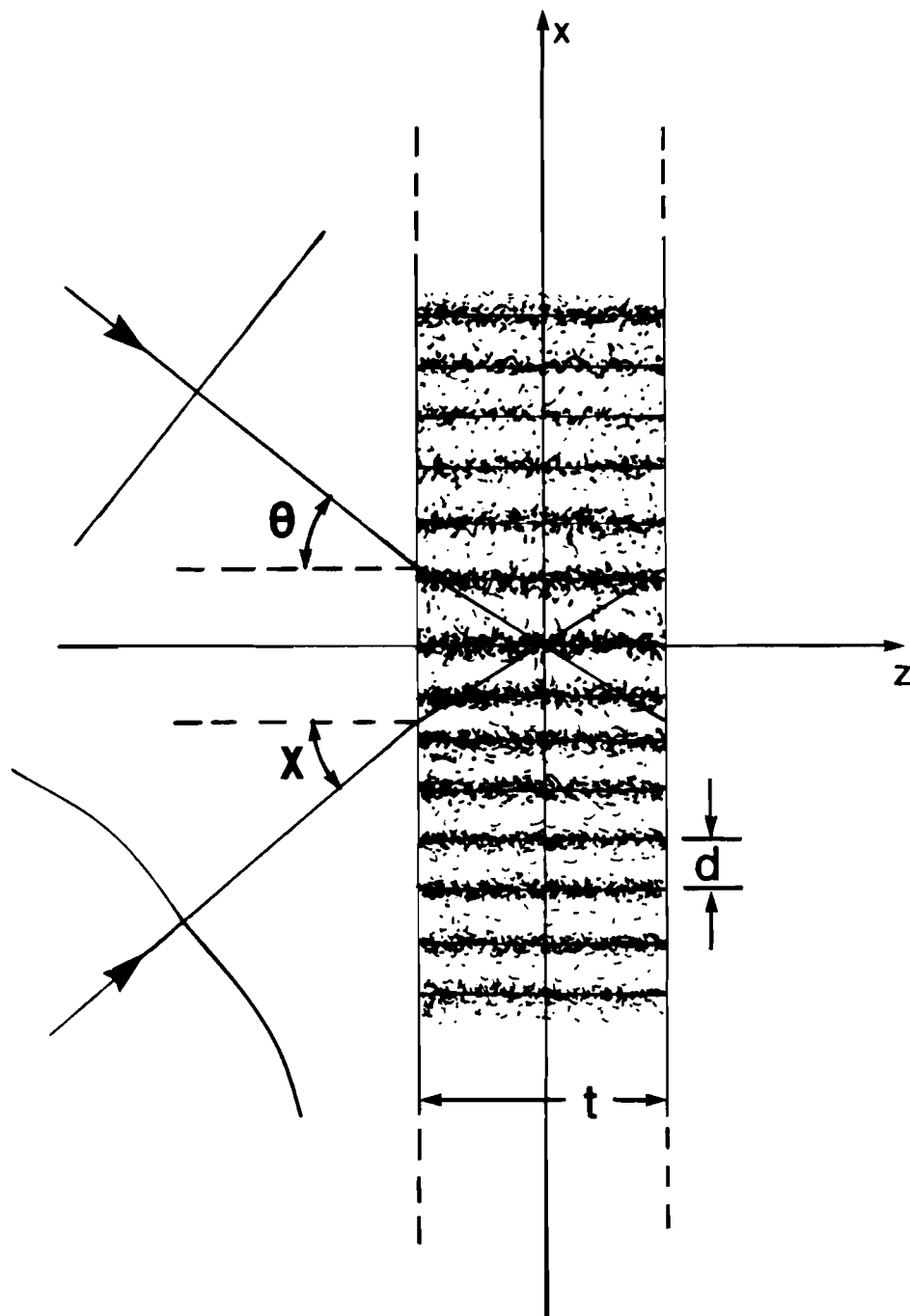
FIGURE 3-3

As the thickness of the photographic emulsion decreases, the planes of metallic silver approach rulings like that of a diffraction grating. A Q factor is defined to determine whether a certain combination of wavelength, emulsion thickness (t), and grating/plane separation will exhibit plane diffraction or volume diffraction characteristics.

$$Q = \frac{2\pi\lambda_0 t}{nd^2} \qquad (3\text{-}10)$$

Generally, a Q > 10 indicates a thick hologram, but volume effects are observed for $1 < Q < 10$.[3] Consider a continuation of the above example (λ = 351 nm, 2χ = 15°), where the emulsion thickness is seven microns, corresponding to an Agfa-Gevaert 10E56 holographic plate. Substituting the expression for the plane spacing, d, into equation 3-10 yields a calculated Q factor of,

$$Q = \frac{8\pi t \sin^2(\chi)}{n\lambda_0} \simeq 6 \qquad (3\text{-}11)$$

Although plane diffraction theory sufficiently describes the reconstruction process, volume effects are anticipated during holographic experiments which utilize the A-G 10E56 plate.

The materialization of the wavefront modulation occurs during development of the silver halide emulsion, and continues throughout subsequent processing. The amplitude transmittance of a photographic negative that is illuminated by a plane wave of amplitude $C_0(x)$, is given by

$$T_A(x) = C_0(x)e^{-a(x)t} e^{ikn(x)t(x)} \tag{3-12}$$

where $a(x)$ = absorption constant
          $t(x)$ = emulsion thickness
          $n(x)$ = refractive index

If the exposure and development cause a spatial variation of the absorption constant, then the transmitted amplitude is modulated in accordance with the exposure and an amplitude hologram is said to exist. Furthermore, if the exposure and development cause a spatial variation in the emulsion thickness, or the refractive index, then a phase hologram also exists.

The metallic silver rulings give rise to an amplitude hologram, but a complex transmittance, due to a phase modulation, from a surface relief and from index variations in the emulsion, is usually observed.[1] We will concentrate on the amplitude hologram and consider phase modulation as a source of coherent noise.

Frieser's two step model (Fig. 3-4) illustrates the transfer from exposure to density.[4] Step one shows the lowered modulation of the signal, characteristic of a modulation transfer function (MTF) less than one, for a given spatial frequency. For the case of two plane wave interference, only a narrow range of spatial frequencies need to be recorded, and the MTF is approximately constant over this range. Step two shows the transfer from effective exposure (E) to density (D). Since the amplitude transmission is related to the density in the following way,

AMPLITUDE TRANSFER
CHARACTERISTIC CURVES

T_A–log(E)
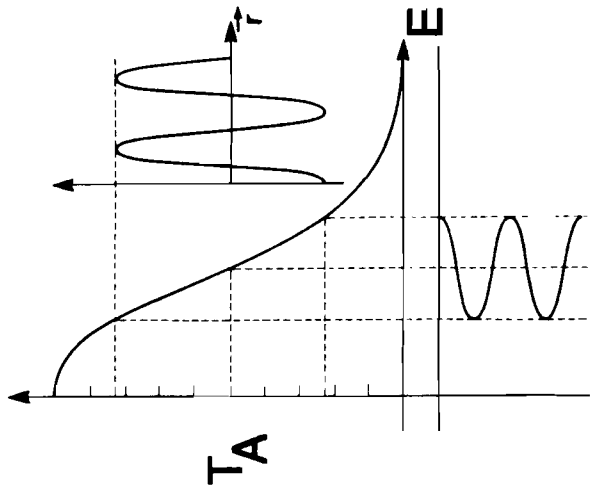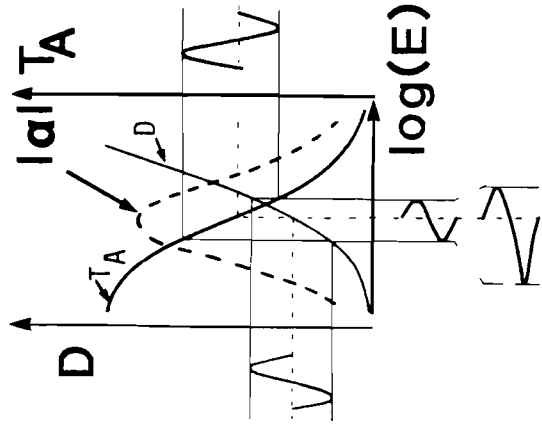
Frieser's
Model

FIGURE 3-4

$$T_A = (T)^{\frac{1}{2}} = 10^{-D/2} \qquad (3\text{-}13)$$

where T is the intensity transmittance, this step also shows the transfer to amplitude transmittance. A T_A - log(E) curve is useful since a Δlog(E) range can be shifted along the log(E) abscissa to determine diffraction efficiency as a function of the mean exposure. A T_A - E curve is more appropriate in showing the range of exposures, or the modulation, for which the exposure and amplitude transmittance are linearly related. The modulation is defined in the following way,

$$M(x,y) = \frac{2[R^2(x,y)0^2(x,y)]^{\frac{1}{2}}}{R^2(x,y) + 0^2(x,y)} = \frac{2[K(x,y)]^{\frac{1}{2}}}{1 + K(x,y)} \qquad (3\text{-}14)$$

where $K(x,y) = 0^2(x,y)/R^2(x,y)$, and $0 \leq M(x,y) \leq 1$.

3.3 Wavefront Reconstruction

In general, the amplitude transmittance is related to the incident exposure as follows:

$$T_A = T_0 + T_1 E + T_2 E^2 + T_3 E^3 + \ldots\ldots\ldots \qquad (3\text{-}15)$$

where T_0 is the zero exposure transmittance. The second term represents the linear relationship that would ideally exist. Each higher order term represents a nonlinearity which produces extraneous images and distortions in the first order image. Linear recording and processing are assumed such that all orders greater than one are suppressed.

Complex notation compactly describes all of the reconstructing wavefronts. Rewriting equation 3-5 in complex notation we obtain,

$$S(x,y) \propto O^2(x,y) + O(x,y)R(x,y) \, e^{i[2\alpha x + \psi(x,y) - \phi(x,y)]}$$
$$+ R^2(x,y) + O(x,y)R(x.y) \, e^{-i[2\alpha x + \psi(x,y) - \phi(x,y)]} \quad (3\text{-}16)$$

Substituting the above expression for the exposure, E, into the linear term of equation 3-15 yields an expression for the amplitude transmittance function, T_A', of the photographic negative.

$$T_A' = T_0 + T_1 \left[O^2(x,y) + R^2(x,y) + O(x,y)R(x,y) \cdot \right.$$
$$\left. \left\{ e^{i[2\alpha x + \psi(x,y) - \phi(x,y)]} + e^{-i[2\alpha x + \psi(x,y) - \phi(x,y)]} \right\} \right] (3\text{-}17)$$

Wavefront reconstruction is achieved by propagating a second reference wave through the holographic plate. Let the new reference wave be represented by $W(x,y)$,

$$W(x,y) = R'(x,y) \, e^{-i\omega t} \, e^{i[\epsilon x + \Omega(x,y)]} \qquad (3\text{-}18)$$

where ϵ is the propagation constant, $\epsilon = k\sin\beta$, and β is the incident angle of the reference beam. The transmitted amplitude, $E(x,y)$, is given by,

$$E(x,y,t) \propto R'(x,y)[O^2(x,y) + R^2(x,y)] \, e^{i[-\omega t + \epsilon x + \Omega(x,y)]}$$

$$+ R'(x,y)O(x,y)R(x,y) \, e^{-i[\omega t - \epsilon x + 2\alpha x + \psi(x,y) - \phi(x,y) - \Omega(x,y)]}$$

$$+ R'(x,y)O(x,y)R(x,y) \, e^{i[-\omega t + \epsilon x + 2\alpha x + \psi(x,y) - \phi(x,y) + \Omega(x,y)]}$$

$$(3\text{-}19)$$

The propagation constants of the three reconstructed components show that they are spatially separated from one another. The first term represents the zero order wave, which passes through the emulsion in the same direction as the reconstructing wave, $W(x,y)$. The second term represents the secondary wave related to the conjugate of the original wave. The third term, E_{object}, is the primary reconstructed wave, which is related to the original object wave:

$$E_{obj.} \propto R'(x,y)O(x,y)R(x,y) \, e^{i[-\omega t + (2\alpha + \epsilon)x + \psi(x,y) - \phi(x,y) + \Omega(x,y)]}$$
$$(3\text{-}20)$$

If the reconstructing wave propagates along the same path as the original reference wave, i.e., $\beta = -\chi$, then $\epsilon = -\alpha$, (see Fig. 3-1) and the object amplitude is given by,

$$E_{obj.} = R'(x,y)O(x,y)R(x,y)\, e^{i[-\omega t + \alpha x + \psi(x,y) - \phi(x,y) + \Omega(x,y)]}$$

$$(3\text{-}21)$$

The propgation constant, $\alpha = k\sin\chi$, shows that the reconstructed object wave travels along the same path as the original object wave. Dropping the phase term, and suppressing the time dependence, we obtain the following expression for the reconstructed field.

$$E_{obj.} = R'(x,y)R(x,y)\, e^{i[\Omega(x,y) - \phi(x,y)]}\, O(x,y)\, e^{i\psi(x,y)}$$

$$(3\text{-}22)$$

Ideally, the reference wave distributions $R'(x,y)$ and $R(x,y)$ are constant, while their corresponding phase distributions are equal to within a constant phase factor. The resulting amplitude is then given by

$$E_{obj.} = K_0\, O(x,y)\, e^{i\psi(x,y)}$$

$$(3\text{-}23)$$

which is the original object wave, differing only by a multiplicative constant.

Although plane reference waves are advantageous, since they can be reproducibly aligned, we see from equation 3-22 that diffraction limited plane reference waves are not necessary. Nominally plane waves, con-

taining slowly varying phase errors, are sufficient as long as the condition that $\Omega(x,y) - \phi(x,y) = $ constant is satisfied. Differences, between the two phase distributions, translate directly to the phase distribution of the reconstructed object wave. Equation 3-22 shows that any amplitude nonuniformities, in the recording reference wave, translate directly to nonuniformities in the reconstructed object amplitude. Large nonuniformities would change the bias exposure, and linear recording would be challenged. Similarly, the reconstructing reference wave translates its nonuniformities to the reconstructed object amplitude.

Linear recording is a result of keeping the exposure, E, within the linear region of the T_A - E curve, such that

$$E_0(1-m) < E < E_0(1+m) \tag{3-24}$$

where the allowable modulation (m) is bounded somewhere between zero and one, depending on the shape of the T_A - E curve. E_0 is the bias exposure, and is equal to $R^2(x,y) + O^2(x,Y)$. This condition on E is obtained through correct biasing, and a $K = O^2(x,y)/R^2(x,y)$ value somewhat less than one.

It is not clear, from a T_A - E curve, that regions of lower intensity within the object wave, will reconstruct as regions of proportionally lower intensity. The zero order reconstructed wave is transmitted as though it passes through a photographic negative, but to understand how

AMPLITUDE TRANSFER FUNCTION
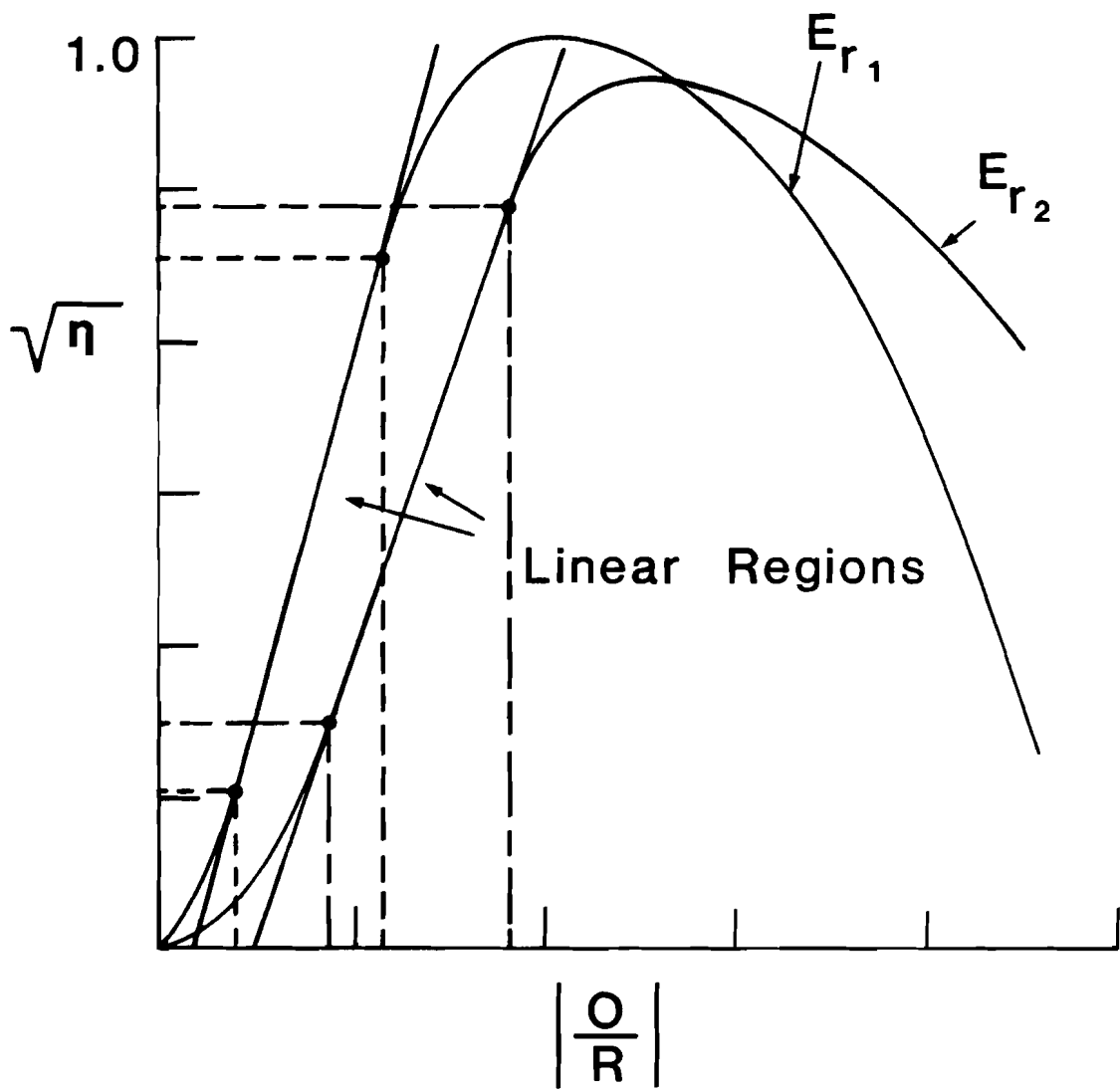
FIGURE 3-5

the relative amplitude ratio throughout a reconstructed wavefront, can be preserved, we need to examine the diffraction efficiency (η). The diffraction efficiency of thin amplitude holograms, as well as volume amplitude and volume phase holograms, are discussed in the literature.[3,5] The function describing the reconstructed amplitude, as a function of $\sqrt{K}$ and the reference wave amplitude, is called the Amplitude Transfer Function (ATF).[1] Figure 3.5 shows a typical series of $\sqrt{\eta}$ -$\sqrt{K}$ curves, where the reference wave intensity, E_r, is the varied parameter. The ATF illustration of η is most appropriate here because we are primarily interested in the results of recording a uniform reference beam, with a varying object beam. The range of beam ratios $\sqrt{K}$, for which the amplitude is linearly recorded, is indicated by the straight-line portion of the $\sqrt{\eta}$ -$\sqrt{K}$ curve at constant reference beam intensity, E_r. A family of curves of this type are invaluable as a method to determine the best compromise between linearity and diffraction efficiency. For our purposes, the compromise will be influenced by the range of object beam amplitude fluctuations that need to be recorded and the amount of laser energy available for continous wave reconstruction.

3.4   Sources of Noise

The main sources of noise involve light that is diffracted or scattered into, or out of, the reconstructed object wave. All noise mechanisms are signal dependent and combine coherently with the reconstructed wave. Nonlinear recording is potentially the largest source of noise. In addition to a nonlinearly reconstructed object wave, a nonlinear

T_A - E relationship can cause higher order images and false images sur-rounding the object wave.[1]

The granular nature of the AgBr in the photographic emulsion, and the metallic silver after development, causes random scattering of the object and reference beams during exposure, and the reference beam during recon-struction. The scattered light forms a veiling glare around the recon-structed object wave. Scattering can also arise from the inhomogeneities and surface deformations of the support and binding materials. These optical imperfections can be introduced during the fabrication and/or the processing stages.

Some phase modulation is inherent in amplitude holograms. The pre-dominant effect is a surface relief in the gelatin, caused by tanning (increased cross-linking between molecules) or hardening due to the re-action products of certain developers.[3] This can be elminated by means of a liquid gate. A liquid gate consists of a leak proof chamber that is sandwiched between two interferometrically flat windows. The outer two surfaces are coated with anti-reflection thin films. The chamber is filled with an index matching fluid, and contains a mechanism to fasten the glass plate. This device can elminate halation effects, multiple reflections, some types of scattering, and phase variations in the emul-sion and glass plate.

3.5 Coherence

Spatial and temporal coherence, two characteristics of laser radiation, are necessary for the holographic recording of a wavefront. Spatial coherence is defined by considering two different points, $P_1(x_1,y_1)$ and $P_2(x_2,y_2)$ which, at time $t = t_0$, lie on the same wavefront. $E_1(x_1,y_1,t)$ and $E_2(x_2,y_2,t)$ are the corresponding electric fields at these points. By definition, the differences between the phases of the two fields at time $t = t_0$ is zero. A coherent relationship between points P_1 and P_2 means that the difference between the phases of the two fields remains zero for any time $t > t_0$.[6]

A hologram can be recorded with a reference beam which has poor spatial coherence, but accurate reconstruction becomes a difficult alignment task. Reference beams having good spatial coherence (plane, spherical) are desired for they can be easily duplicated during the reconstruction process. A holographic technique which utilizes a reference beam that is generated from a small region of the object wave requires a high degree of spatial coherence, since many object points interfere with the same reference point. Ideally, a laser system, based on a laser oscillator that operates on a single transverse mode, should have sufficient spatial coherence.[5]

Temporal coherence is defined by considering a general point $P(x,y)$ at two different times t and $t + t_0$. If, for a given elapsed time t_0, the phase difference between the electric fields $E(x,y,t)$ and $E(x,y,t_0)$ remains the same for any time t, then temporal coherence is

said to exist for that time interval t_0.[6] The time during which the wave is coherent, multiplied times the propagation velocity of the wave, is called the coherence length. Defining the coherence length, L_c, as the pathlength difference which reduces the reconstructed intensity by 50%, then for an ideal single frequency gaussian pulse, it is given by[7]

$$L_c = \frac{\pm 2^{\frac{1}{2}} \ln(2) c_0}{\pi \Delta f} \tag{3-25}$$

where $\Delta f = 2 \ln(2)/\pi \tau_0$ is the line width (FWHM), and τ_0 is the pulsewidth (FWHM). Ideally, a gaussian shaped laser pulse, of one nanosecond pulsewidth, has a coherence length of approximately $L_c = 21$ centimeters. Generally, effects due to temporal incoherence can be minimized by setting the time differential to zero, but a frequency swept laser oscillator or a frequency shift in a laser amplifier can cause the optimum path difference to be other than zero.

When the phase fluctuations of the waves are random, the concepts of spatial and temporal incoherence can be combined by means of the first order Mutual Coherence Function (MCF), defined as[6]

$$\Gamma^{(1)}(\vec{r}_1, \vec{r}_2, \tau) = \lim_{T \to \infty} \int_{-T}^{T} V(\vec{r}_1, t+\tau) V^*(\vec{r}_2, t) dt \quad , \tag{3-26}$$

here $V^{(1)}(r,t)$ is called the complex analytic signal. The MCF can be normalized to become the complex degree of coherence

$$\gamma^{(1)}(\vec{r}_1,\vec{r}_2,\tau) = \frac{\Gamma^{(1)}(\vec{r}_1,\vec{r}_2,\tau)}{[\Gamma^{(1)}(\vec{r}_1,\vec{r}_1,0)\Gamma^{(1)}(\vec{r}_2,\vec{r}_2,0)]^{\frac{1}{2}}}$$ (3-27)

where $\quad 0 < \left|\gamma^{(1)}(\vec{r}_1,\vec{r}_2,\tau)\right| < 1$

We can incorporate the complex degree of coherence into the wavefront modulation. Since we are interested in a reference wave which is generated from a small region of the object wave, a change of spatial coordinates is necessary. For a sufficiently small region, an average coordinate (x_R, y_R) is assigned to the reference wave and equation 3-14 becomes

$$m = m(x,y,t) = \frac{2[R^2(x,y)0^2(x,y)]^{\frac{1}{2}}\left|\gamma^{(1)}[(x_R,y_R),(x,y),\tau]\right|}{R^2(x,y) + 0^2(x,y)}$$ (3-28)

Deviations from perfect spatial or temporal coherence result in a complex degree of coherence less than one, which translates to a decrease in modulation and a corresponding decrease in diffraction efficiency. These deviations can be tolerated if the complex degree of coherence, between the small region selected to be the reference beam and each object beam region, is approximately constant, otherwise, unwanted amplitude variations will be recorded.

The modulation is a time averaged quantity such that,

$$m(x,y,t) \quad \propto \quad \left| <V(\vec{r}_1,t+\tau),V^*(\vec{r}_2,t)> \right|$$

(3-29)

Therefore, one or more short term coherence relationships, as well as one long term coherent relationship can exist. The information storage capacity of a hologram allows for the recording of more than one phasefront, if several short term coherence intervals exist in the midst of time dependent phase on the laser beam.

3.6   Local Reference Beam

Several alternatives are available to generate a reference beam from the original wavefront. The primary requirements on each scheme have already been mentioned in this chapter. Firstly, it must be able to take a portion of the original wave, and produce from it, a uniform amplitude distribution. Secondly, it must create a phase distribution that is interferometrically reproducible between the recording and reconstructing stages. Thirdly, the system must be able to handle the high power densities characteristic of the HPPL.

A holographic system that incorporates a diffuser in the reference beam is shown in Fig. 3-6. A diffuser placed at the front focal plane of a lens produces a uniform amplitude distribution in regions near the back focal plane of the same lens. A direct consequence of this amplitude
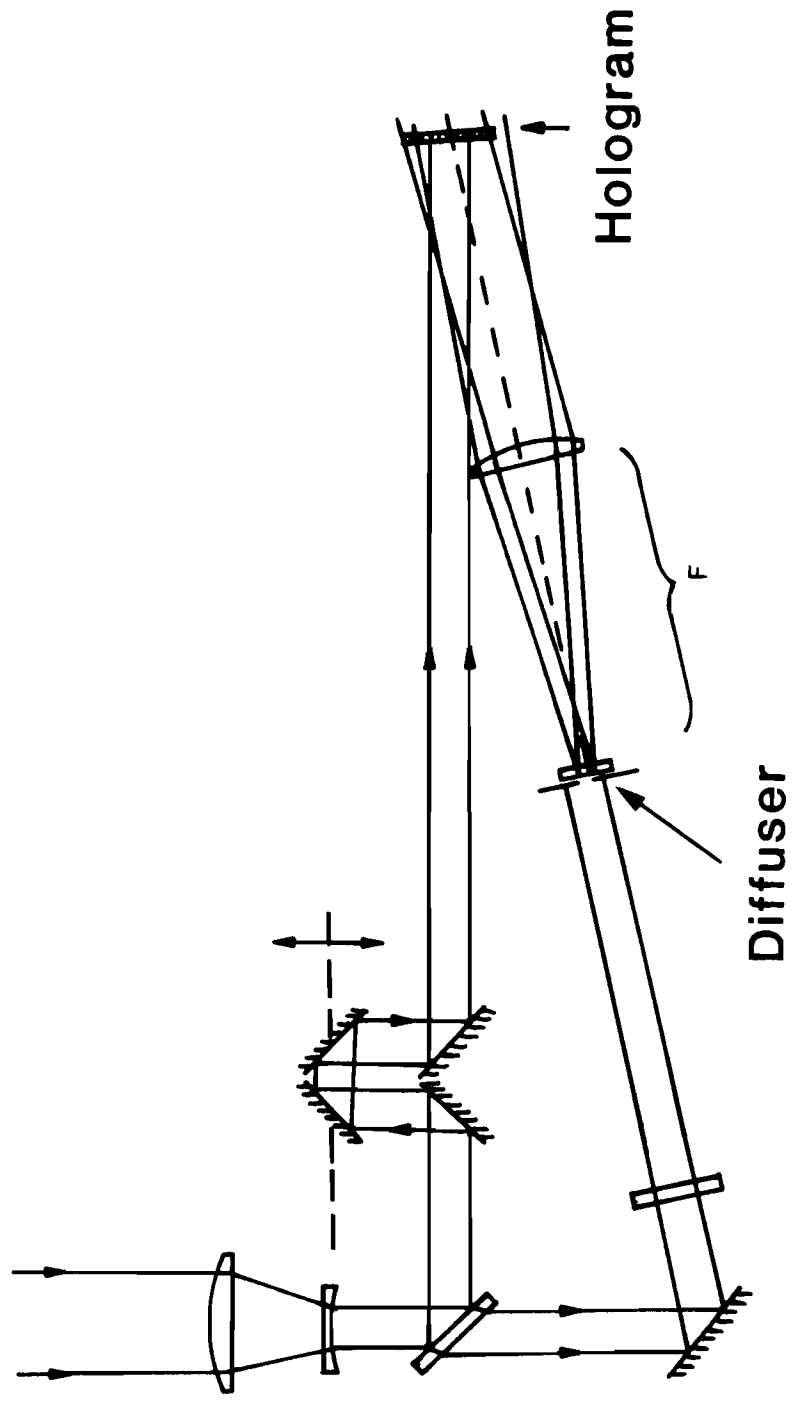
DIFFUSE REFERENCE

Hologram

F

Diffuser

FIGURE 3-6

uniformity, is a spatially modulated phase distribution. This characteristic puts a tight tolerance on the angular and linear shifts of either the diffuser, the hologram, or both during the reconstruction process. Furthermore, a considerable amount of laser energy is lost at the diffuser, during the continuous wave reconstruction, resulting in very low diffracted energies.

Another technique involves the reverse Galilean telescope. A negative lens is place at the center of a large obstruction, and used to expand a small portion of the original wave. The recollimation of this beam would produce a plane wave reference, which is a relatively simple phase distribution to reproduce. For a wavefront with several wavelengths of aberration, a small portion (5% in diameter) of the wavefront would possess a small fraction of a wavelength in phase variation. This method does not contain a way to manipulate the incident amplitude distribution, therefore, the majority of the spatial frequency spectrum, contained in the original wave, is carried through to the recording plane.

A system which is capable of making the spatial frequency spectrum physically accessible, for accurate filtering, is shown in Fig. 3-7. A positive entrance lens, with an internal focus, is utilized in place of the negative lens. The heart of this system, expanded in Fig. 3-8, is generally referred to as a coherent optical processor. Sections of it are discussed in the literature, (Cathey,[1] Goodman[8], and Collier[5]), but a concise mathematical description is found in Stark.[9] An aperture is placed at the input plane (x_1, y_1) to select a small portion of the original wavefront. The complex amplitude transmittance in the front focal plane of the first lens is $r_1(x_1,y_1)$, while the corresponding amplitude distribution in the back focal plane is represented by the
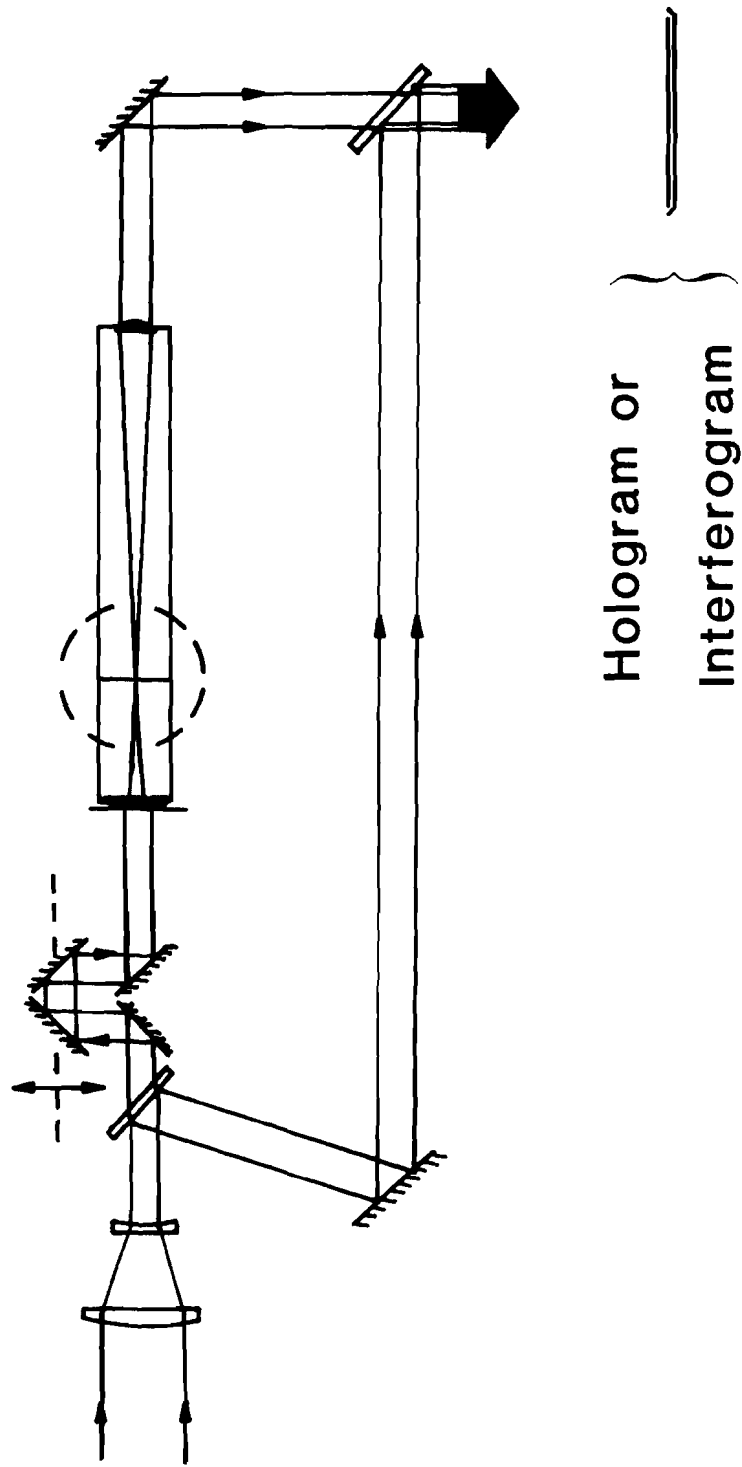
SPATIALLY FILTERED REFERENCE

Hologram or
Interferogram

FIGURE 3-7

SPATIAL FILTER SYSTEM

$$M = -f_2/f_1$$

Pinhole

f_1

f_1

f_2

f_2
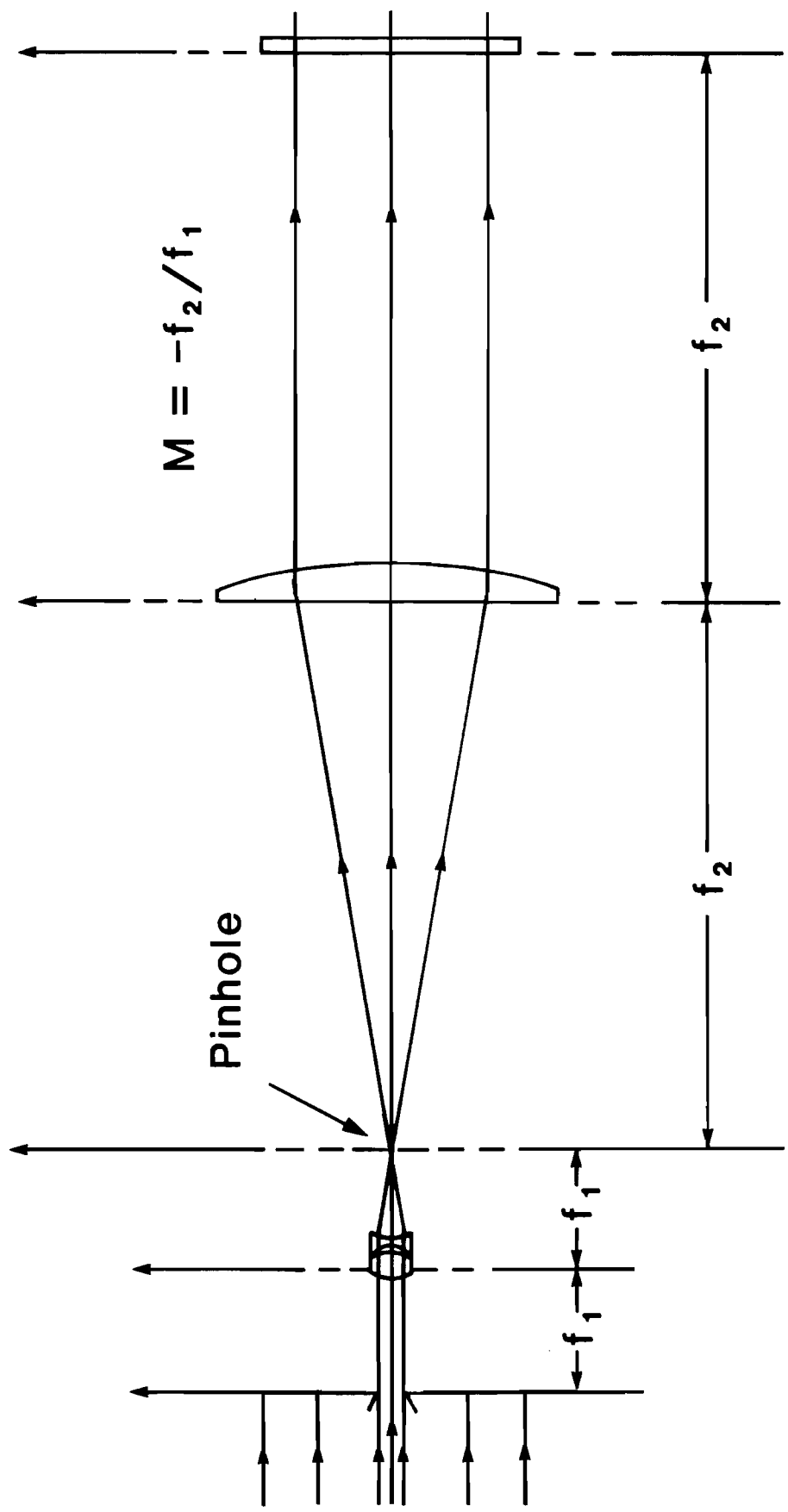
FIGURE 3-8

Fourier transform, $R_1(u,v)$ of the input. Neglecting constant phase and proportionality factors,

$$R_1(u,v) = \int\int_{-\infty}^{\infty} r_1(x_1,y_1)\, e^{-i2\pi(ux_1 + vy_1)} dx_1 dy_1$$

(3-30)

where λ is the wavelength and (u,v) are the spatial frequencies such that $u = x_f/\lambda f_1$ and $v = y_f/\lambda f_1$.

When a spatial filter is placed in the back focal plane of the first lens, the amplitude distribution, just after the Fourier plane, is given by

$$U_f(x_f,y_f) = R_1(x_f,y_f) \cdot T(x_f,y_f)$$

(3-31)

where $T(x_f,y_f)$ is the filter amplitude transmittance. The same Fourier transform relationship exists for the front and back focal planes of the second lens. Therefore, the output spectrum equals the product of the input spectrum times and frequency transfer function $H(u,v) = T(\lambda f_1 u, \lambda f_1 v)$,

$$R_2(u,v) = R_1(u,v) \cdot H(u,v)$$

(3-32)

The filter operates directly on the spatial frequency spectrum of the incident wave. By Fourier transforming both sides of 3-27, we find that

the output amplitude can be represented by the convolution of the input amplitude, scaled by a magnification, $M = -f_2/f_1$, with the impulse response function $h(x_2,y_2) = \mathcal{F}[H(u,v)]$.

$$r_2(x_2,y_2) = 1/M \int\limits_{-\infty}^{\infty}\!\!\!\int r(Mx_1,My_1)h(x_2-Mx_1,y_2-My_1)dx_1dy_1 \qquad (3\text{-}33)$$

A pinhole is a low-pass, blocking, spatial filter with an amplitude transmittance,

$$T(x_f,y_f) = \text{circ}(r_f/r_o) = \begin{cases} 1 & 0 < r_f < r_o \\[2ex] 0 & \text{elsewhere} \end{cases} \qquad (3\text{-}34)$$

where r_o is the pinhole radius which determines the cut-off frequency, $\nu_c = r_o/\lambda f_1$.[10] As the frequency transfer function approaches a narrow circ function, i.e. small pinhole, the impulse response function becomes a broad, first order Bessel function of the first kind. Conceptually, it is the convolution of this Bessel function with the input function that causes a smoothing of the amplitude distribution. Physically, it is still the blocking of the high frequency Fourier components that results in increased amplitude uniformity.

Although it appears that the pinhole diameter should be chosen strictly based on the lowest spatial frequency that needs to be filtered out, the amplitude modulation, caused by the size of the pinhole, must be considered. Figure 3-9 shows the amplitude distributions that result
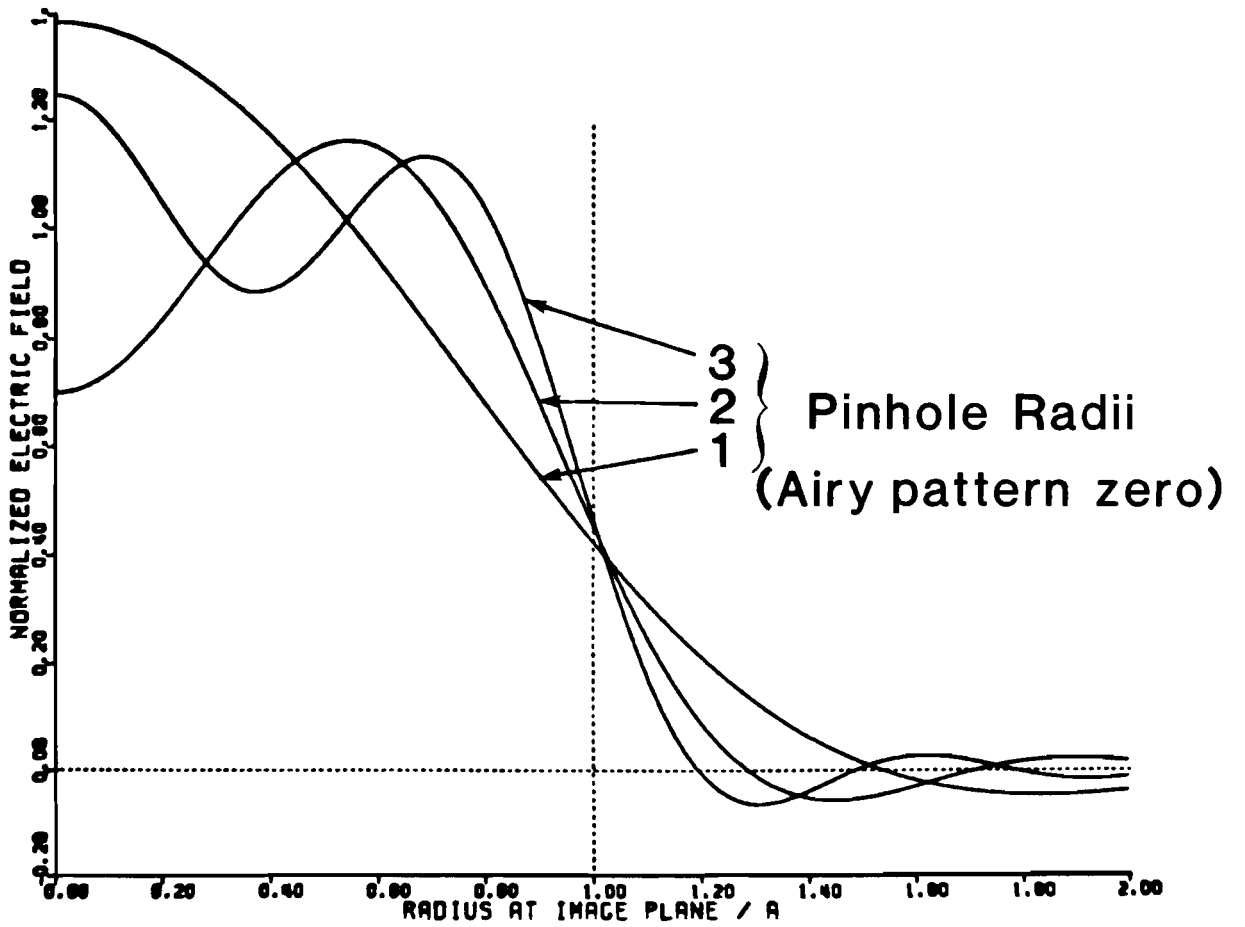
IMAGES OF FILTERED PLANE WAVE

FIGURE 3-9

from the spatial filtering of an incident plane wave.[11] The pinhole radii were chosen to be the first, second, and third zeros of the Airy pattern,

$$\text{Airy Intensity} = \left| \frac{2\pi a^2 \, J_1(2\pi a\rho)}{2\pi a\rho} \right|^2 \tag{3-35}$$

where the zeros are given by $(2a\rho)_{1,2,3} = 1.220, 2.233, 3.238$ respectively. Since $\rho = r_0/f_1$, and $2a = d$, where d is the entrance pupil diameter, the radial positions of the minima are given by,

$$r_{min.} = (2a\rho)(\lambda f_1)/d \tag{3-36}$$

The image of the input aperture, when the pinhole surrounds only the first zero, contains a monotonically decreasing amplitude. A smaller pinhole would broaden the image and begin to decrease the total energy. As the pinhole radius varies between the first and second zeros, the amplitude distribution changes from a center peaked profile to an edge peaked profile. For the case of $r_0 \gg r_3$, a modulated amplitude distribution at the recording plane is a magnified version of the input aperture transmission function. Therefore, for an input plane wave, the amplitude modulation, caused by the presence of a circular aperture at the Fourier transform plane of a lens, is a minimum if either of the following conditions is satified:

$$r_{pinhole} \simeq \lambda F_{\#} \quad \text{(3-37a)}, \qquad r_{pinhole} \gg 3\lambda F_{\#} \quad \text{(3-37b)}$$

The results of spatially filtering a gaussian intensity distribution, such as a CW argon laser, would be different, and would depend on where the input aperture cut into the edge of the gaussian profile.[11,12]

The level of spatial filtering needed to obtain an optimally uniform amplitude is influenced by the spatial frequency content of the wavefront and the above conditions for minimum induced amplitude modulation. To illustrate this, if the region of the original wavefront selected to be the reference beam is characterized by several high frequency components superimposed onto a flat-top amplitude distribution, then a pinhole radius which satisifies condition 3-37b would produce the optimum amplitude distribution. On the other hand, if the original wavefront has a large range of spatial frequencies, then condition 3-37a should be satisfied, and the system magnification, $M = -f_2/f_1$, should be adjusted to utilize only the central region of the collimated output. In either situation, spatial frequencies that are smaller than the cut-off frequency, ν_c, should not be present in the portion of the original amplitude distribution that is selected to become the reference beam.

In a coherent optical system, any displacement of a spatial filter from its optimum position degrades the performance of the system and causes a modulation of the amplitude distribution.[13] Vander Lugt studied the effects of laterally and longitudinally displacing a spatial filter in an optical data processing system. He determined that the signal-to-noise ratio, normalized to one at zero displacement, degraded to

SNR = 0.5 for a lateral displacement of 5 µm, for $F_{\#}$ = 10. A similar displacement in the longitudinal direction produced much less of an effect.

The spatial filtering of a HPPL is possible only if the power density associated with the focussed spot is less than that required for the breakdown of air. If a vacuum spatial filter is used, then a higher power density can be propagated through the pinhole, until a point where a pinhole closure phenomenon occurs. Approximate energy density values, for a one nanosecond, 351 nm pulse, needed to observe air breakdown or pinhole closure, are not readily available.

An experimental study[14] of gas breakdown induced by the ultra-violet, second harmonic radiation of a ruby laser (347 nm), at a pulse-width of eight nanoseconds, gives evidence that the breakdown of air, at atmospheric pressure, is approximately $4x10^{10}$ W/cm^2. This work also showed that the breakdown of Argon tracked parallel with that of air, where the atmospheric breakdown of Argon was determined to be about $2x10^{10}$ W/cm^2. In another experimental study,[15] the laser induced breakdown of Argon was determined for the relevant wavelength, λ = 351 nm, at atmospheric pressure, and at the pulsewidth of 500 ps. Extrapolation of model calculations which fit the data, predict a power density threshold of approximately $2x10^{12}$ W/cm^2, for Argon gas. These two experimental studies, although performed on slightly different wave-lengths, and different pulsewidths, do not agree. Pulsewidth differences do not explain the factor of 100 difference between the two studies. The improved quality of frequency converted beams over the last ten years might explain these differences. If we accept the result that Argon and air track in parallel, as a function of pressure, from the first study,

and we accept the power density threshold for Argon stated in the second study, then an estimated upper limit for the power density threshold for air is 4×10^{12} W/cm^2.

The power density at the focal plane of the lens is calculated with the following expression:

$$\eta = \frac{E_0}{\tau A} = \frac{E_0}{\tau \pi (1.22 \lambda F_\#)^2} \qquad (3\text{-}38)$$

where τ is the pulsewidth (FWHM), E_0 is the energy required to expose a given holographic plate to the correct bias level, and $A = \pi(1.22 \lambda F_\#)^2$ is the area of the Airy disc. The required energy, E_0, is estimated from the product of the plate sensitivity, in joules per square centimeter times the area of the reference beam. Operating at $F_\# = 7$, with an eight centimeter reference beam diameter, an 850 ps pulsewidth, and an Agfa-Gevaert 10E56 holographic plate as the recording medium, the required energy is approximately one millijoule, and the power density would be approximately 4 terawatts per square centimeter. The feasibility of spatial filtering the reference beam under these conditions will be determined experimentally.

A study of the pinhole-closure phenomena was completed on the radiation from a Nd:glass laser ($\lambda = 1.054$ µm).[16] It was determined that the power density threshold, for significant plasma formation is approximately 10^{12} W/cm^2, for a low pressure environment. The rate of closure was estimated to be $2\text{-}5 \times 10^7$ cm/sec. This rate suggests that if a plasma is formed due to excessive power densities, then a pinhole smaller than 200 µm will close for more than 50% of the duration of the

-60-

pulse, for a pulsewidth of one nanosecond. An indication of pinhole closure would be the blocking of certain Fourier components for power densities near threshold, and a complete blocking of the light for increased power densities.

The reconstructed energy density, γ, can be estimated with the following equation:

$$\gamma = \frac{\alpha \, E \, R \, S \, T}{A}$$

(3-39)

where α is the diffraction efficiency of the hologram, E is the output energy of the CW laser, R is the uniform fraction of the gaussian CW laser beam, S is the fraction of incident energy that passes through a pinhole of the size of the Airy disc, T is the holographic plate transmittance, and A is the area of the reconstructed wavefront. The following values for these parameters are reasonable for preliminary calculations:

E = 20 mW @ 351.1 nm

α = 0.01

R = 0.40

S = 0.84

T = 0.50

$A = \pi \, (6.3/2)^2 \, cm^2$

The resulting energy density of $\gamma \simeq 1 \; \mu j/cm^2$ suggests that long exposure times will be necessary for the photographic recording of shearing interferograms of the reconstructed phasefront.

3.7   Conclusion

Holographic theory supports the thesis that the wavefront of a high-peak-power laser can be linearly recorded and processed, and that a continuous wave laser can reconstruct this wavefront for real-time analysis. Coherence effects, nonlinear mechanisms, and spatial filtering impracticalities challenge the success of this technique, but alternate methods and reasonable compromises are available to make experimentation attractive.

REFERENCES

1. W.T. Cathey, <u>Optical Information Processing and Holography</u>, John Whiley and Sons, 1974, pp. 48,131,114

2. L.M. Soroko, <u>Holography and Coherent Optics</u>, Plenum Press, 1980, p. 402

3. H.M. Smith, <u>Holographic Recording Materials</u>, Springer-Verlag, 1977, pp. 3,5,55

4. H. Frieser, <u>Photographic Information Handling</u>, Focal Press-London/New York, 1975

5. Collier, Burckhardt, Lin, <u>Optical Holography</u>, Bell Telephone Laboratories, 1971, pp. 223,228,316,124

6. O. Svelto, <u>Principles of Lasers</u>, Plenum Press, 1982, pp. 9,270

7. L.D. Siebert, "Holographic Coherence Length of a Pulse Laser", <u>Applied Optics</u>, Vol. 10, #5, 1971, p. 632

8. J.W. Goodman, <u>Introduction to Fourier Optics</u>, McGraw-Hill,1968, p. 166

9. S.P. Almedia, G. Indebetouw, "Pattern Recognition via Complex Spatial Filtering", <u>Applications of the Optical Fourier Transform</u>", H. Stark, Acedemic Press, 1982, p. 47

10. J.D. Gaskill, <u>Linear Systems, Fourier Transforms, and Optics</u>, John Whiley and Sons, 1978, p. 228

11. J. Kelly, "The Operation of the Hard Aperture and Air Spatial Filter Combination", <u>Laboratory for Laser Energetics</u>, Unpublished Internal Report

12. L.D. Dickson, "Characteristics of a Propagating Gaussian Beam", <u>Applied Optics</u>, Vol. 9, #8, Aug. 1970, p. 1854

13. A. Vander Lugt, "The Effects of Small Displacements of a Spatial Filter", <u>Applied Optics</u>, Vol.6, #7, 1967, p. 1221

14. Alcock, Kato, Richardson, "New Features of Laser Induced Breakdown in the Ultraviolet", <u>Optical Communications</u>, Vol.6, #4, Dec. 1972, p. 342

15. Wehl, Rosen, Wilson, Seka, "Laser Induced Breakdown of Argon at 0.35 um", <u>Physical Review A</u>, Vol.26, #2, 1982, p. 1164

16. <u>Lawrence Livermore Laboratory</u>, "Studies of Closure Phenomena in Pinholes Irradiated by Nd Laser Pulses", p. 5

IV. EXPERIMENTAL RESEARCH

4.1   Introduction

The majority of experimental work consisted of demonstrating conven-
tional wavefront measurement techniques, and investigating alternate
methods of creating a suitable reference beam for holographic applica-
tions.   Together with preliminary holographic experiments, this work
revealed problems unique to the high-peak-power laser, and guided an
evolution of system designs. Wavefront recording and reconstruction were
performed on the same final design. The system performance was evaluated
by means of comparison with results from conventional methods.

4.2   GDL Laser System

The Glass Development Laser (GDL) is a one-beam prototype of a
twenty-four-beam laser system (OMEGA) located at the Laboratory for Laser
Energetics (LLE) of the University of Rochester. The system is based on
a frequency tripled neodymium:phosphate glass laser, illustrated in Fig.
4-1. An active-passive mode-locked oscillator, generating pulses between
750 picoseconds and one nanosecond full width at half maximum (FWHM), and
operating at a wavelength of 1.054 μm, drives a six-stage amplifier
chain.[1] An intracavity aperture is located close to the oscillator rod
to optimize output uniformity and restrict oscillations to one transverse

Glass Development Laser

FIGURE 4-1

mode (TEM_{00}). The pulse trains emitted from the oscillator contain between 18 and 25 pulses (FWHM), spaced at 20 ns intervals. Individual pulsewidths of about 850 $\pm$ 50 ps were measured, prior to our experiments, with a Hadland Imacon streak camera and an EG&G optical multichannel analyzer. Satellite free pulses are switched out from the pulse train by means of a sequence of polarizers and krytron driven Pockel's cells. The krytron high voltage switch is triggered by a time-delayed signal from a vacuum photodiode that senses the pulse train energy.

The switched-out pulse, with a nominal energy of 200 µJ, is truncated by a circular input aperture, and is subsequently amplified by the first three amplifiers. The flashlamp pumped cylindrical rods (16, 30, 40 mm diameter) amplify the beam by approximately 100, 40, and 20 times, respectively. The two 64 mm diameter amplifiers have typical gains of between 10 and 16. The final amplification stage (90 mm diameter) produces a gain of between 5 and 8.[2] Vacuum spatial filters are situated between each amplifier to filter out the high frequency components and to permit complete image relaying of the input aperture throughout the laser system. Spatial filter losses, optical component insertion losses, and mirror losses diminish the $5x10^6$ gain as indicated by a set of typical energies for various locations in the system, shown in Fig. 4-1.

A Pockel's cell/polarizer isolation system is placed between the first and second and between the third and fourth amplification stages to protect the front end of the system from potentially damaging back reflections, and to increase the contrast ratio between the transmitted and rejected parts of the pulse. Furthermore, a Faraday rotator/polarizer system, located between the two 64 mm amplifiers, isolates the smaller-aperture driver-line from high irradiance back reflections.

The GDL frequency conversion system utilizes two KDP type II crystals as shown in Fig. 4-2.[3] Each crystal is mounted between two ultraviolet-grade fused silica windows; an index matching fluid called Koolase[4] fills the gaps between surfaces. The first crystal converts the incident infrared radiation to the second harmonic (λ = 527 nm), yielding an approximate green to infrared energy ratio of two to one. After doubling, the first (1ω) and second (2ω) harmonics are combined in the second crystal to generate third harmonic (3ω) radiation. Although the GDL facility is capable of producing higher energies and greater efficiencies, a typical maximum laser output of 130 joules at λ= 1.054 μm is converted at 50 to 55% efficiency to produce about 70 joules of the third harmonic. The ultraviolet energy is measured with a one inch, surface absorbing, Scientech calorimeter. Lower conversion efficiencies are obtained by lowering the infrared input energy to the frequency conversion system. The 1ω, 2ω, and 3ω components are separated by means of a series of wavelength selective mirror coatings.

In summary, the following parameters characterize the frequency converted laser beam under investigation:

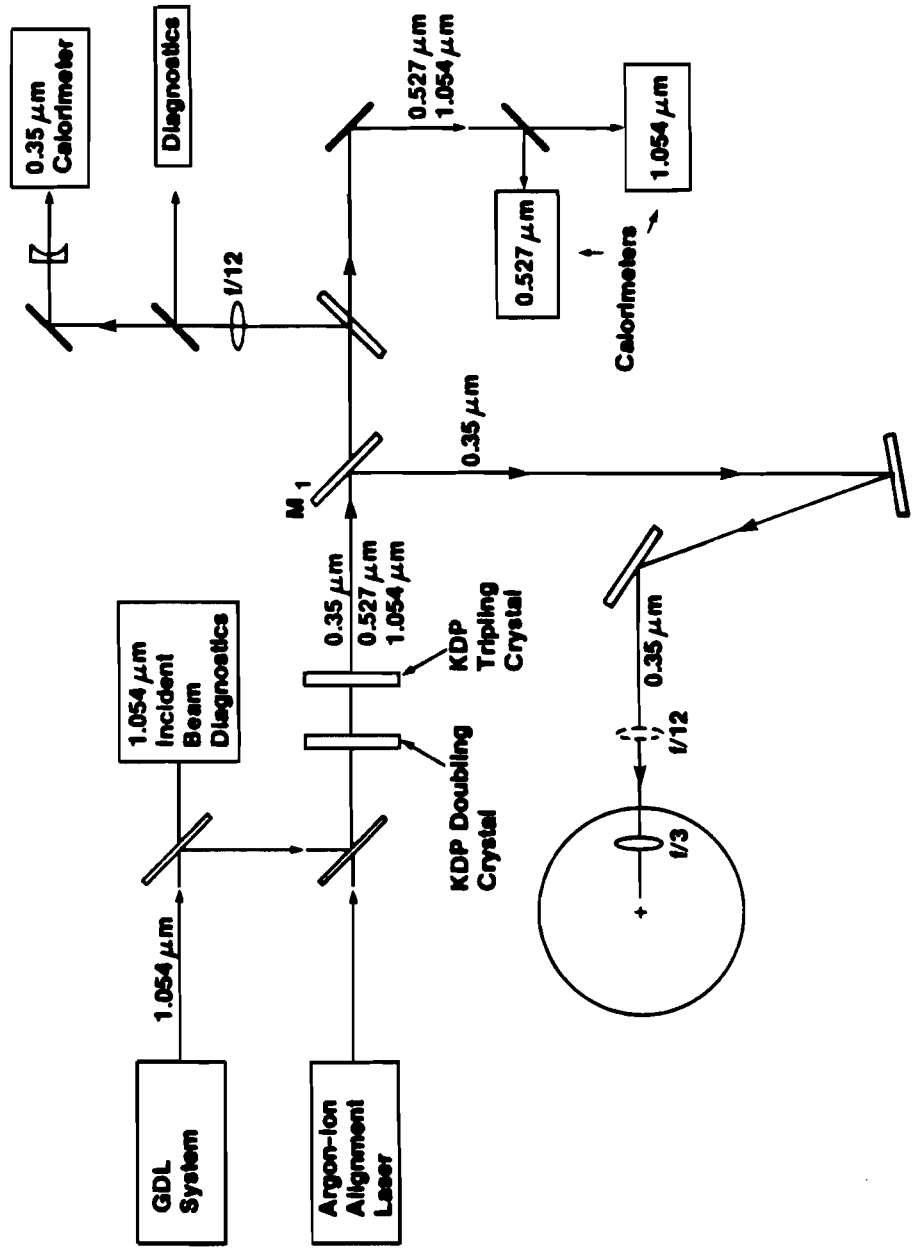|	
Wavelength	351 nanometers
Energy	0-70 joules
Pulsewidth	850 picoseconds (FWHM)
Diameter	12.5 centimeters
Polarization	"S" wrt horiz. path

Frequency Conversion

FIGURE 4-2

4.3   Preliminary Experiments

Preliminary experiments were conducted to generate boundary conditions for the design of a wavefront measuring system. Figure 4.3 shows the basic layout used for several experiments performed on a noninterfering basis with the primary laser user. The lower arm of the interferometer was blocked to provide a uniform beam to an intensity step tablet during film calibrations. Photographic film and holographic plate sensitivities, as well as reciprocity effects, were determined. When investigating coherence effects, the double diffuser in the upper arm was replaced with a negative lens for beam expansion and collimation. The path lengths of the two arms were varied to produce time delays of 50 and 500 picoseconds.

Aerographic film (Kodak 4421) was found to have a sensitivity of approximately 5 ergs/cm^2, for a density of between 1.5 and 2.0 above gross fog. This corresponds to a reciprocity factor of about three. An Aerographic film calibration is contained in Appendix A. Agfa-Gevaert plate 10E56 exhibited a density of between 0.5 and 0.6 when exposed with an irradiance of about 200 ergs/cm^2, indicating a reciprocity factor of between four and five. Kodak plate 649-0 was sufficiently exposed at an irradiance of about 100 to 150 microjoules/cm^2, and exhibited reciprocity effects greater than that of the Agfa-Gevaert plate. These reciprocity factors are only estimates, since the spectral sensitivities provided by the manufacturers do not include λ = 351 nm.

Similar reconstructions were obtained for the two different time delays, with a decreased diffraction efficiency for the larger path-length difference. Since the two arms of an interferometer can easily be
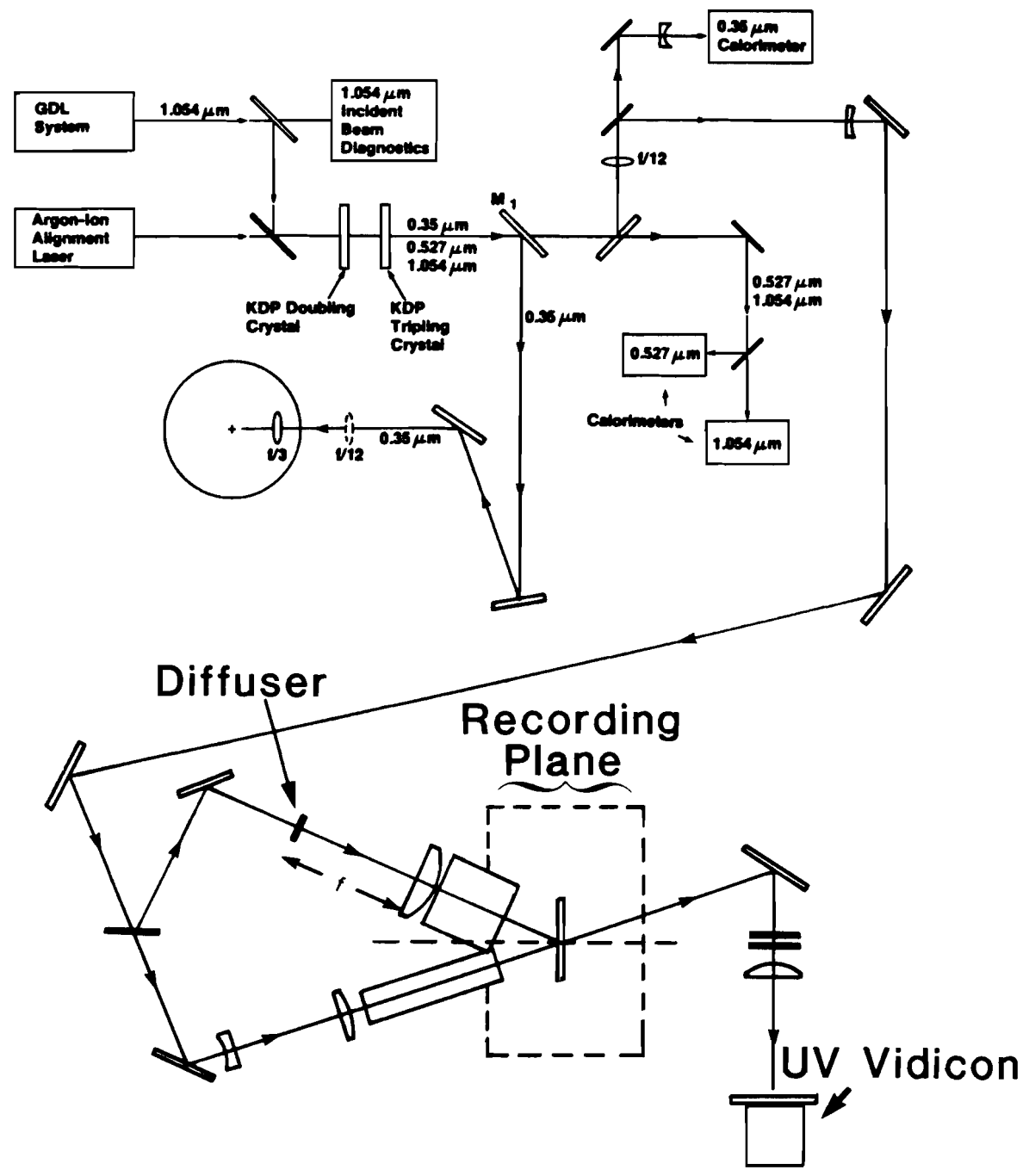
"Piggy-Back" Set-Up

GDL System — 1.054 μm

1.054 μm Incident Beam Diagnostics

Argon-Ion Alignment Laser

KDP Doubling Crystal

KDP Tripling Crystal

0.35 μm
0.527 μm
1.054 μm

M₁

0.35 μm

0.35 μm

f/12

f/3

0.36 μm Calorimeter

f/12

0.527 μm
1.054 μm

0.527 μm

Calorimeters

1.054 μm

Diffuser

Recording Plane

f

UV Vidicon

FIGURE 4-3

aligned to within a few centimeters of optical path difference (OPD), we conclude that the laser coherence was sufficiently long for phasefront measurements.

These experiments demonstrated that an uncoated beamsplitter, with the back side anti-reflection coated, is not suitable for use in an interferometer. Highly modulated fringes were recorded, even when the coating approached a reflectivity of 0.20%; either a wedged or an index matched beamsplitter is required. Ambient room light, due to unconverted 2ω radiation presented a problem, since blocking filters could not be employed, and extensive shielding of the recording apparatus was necessary.

4.4   Conventional Techniques

Wavefront measurement techniques, previously used on an infra-red HPPL, were redesigned for use on the frequency converted laser beam. Figure 4.4 illustrates the basic experimental set-up. (The NRC magnetic table in the lower right is 3' x 7' in size.) The ultra-violet beam was intercepted by an uncoated, 3° wedged, Dynasil 6000 beamsplitter, near normal incidence. The transmitted and secondary reflected beams were blocked with Linagraph thermal paper, which was contained in a plastic packet to prevent blow-off debris from reaching the optical components. The two mirrors between the crystals and the wedge were coated for high reflectivity at λ = 351 nm, and for low reflectivity at the first and

CONVENTIONAL EXPERIMENTAL SET-UP

$1\omega \longrightarrow 3\omega$

Tank

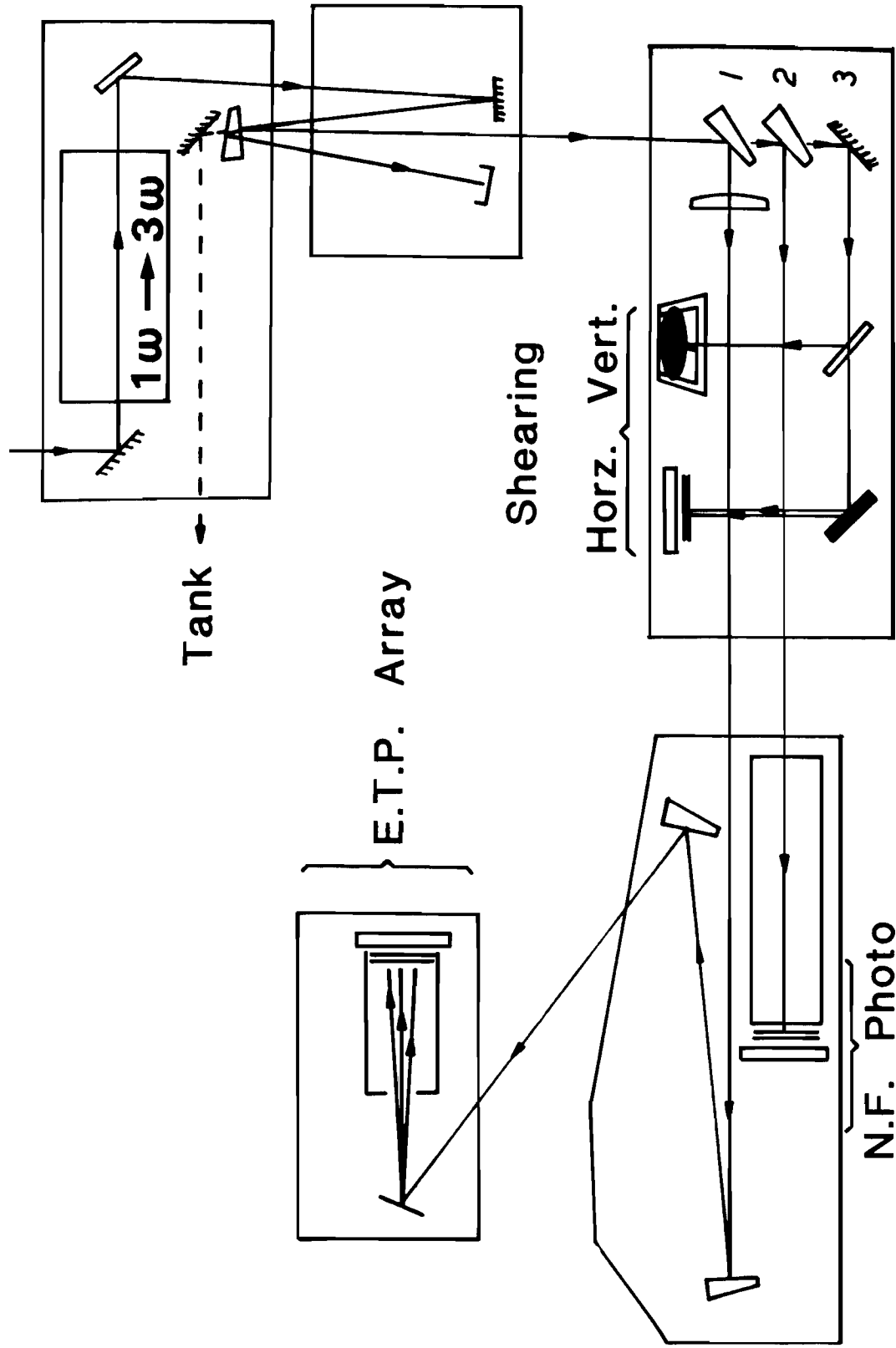E.T.P. Array

Shearing

Horz. Vert.

1
2
3

N.F. Photo

FIGURE 4-4

second harmonics. Therefore, the four percent fraction of incident energy which reached the lower tables had greater than 100 to 1 contrast, i.e. $E(3\omega)/E(2\omega)$, $E(3\omega)/E(1\omega) > 100/1$.

Beamsplitters of sufficient quality were not available for simultaneous use of the three diagnostics. One path was operated for each laser pulse. The first path, containing a Galilean telescope (not shown, M = 1/2), transported the beam through a focussing lens (f.1. = 10 m, fused silica substrate, dual AR @ 351 nm), and into an equivalent-target-plane (ETP) camera. The beam encountered three front surface reflections; one 3° wedged beamsplitter and two uncoated beamsplitters. The second surface reflections were removed by attaching a cell, containing an index matching liquid called Koolase (n = 1.44) to the back of the beamsplitter, resulting in a Fresnel reflection coefficient of 0.019%. The third beamsplitter injected the focussing beam into a 1° etalon (reflectivity = 70% - both surfaces), thus producing both a transmitted and a reflected one-dimensional array in exposure. The reflected arrray contained N elements; R = 0.7, .09(0.7), .09(0.7)0.5, $.09(0.7)(0.5)^2$ ....,$.09(0.7)(0.5)^{N-2}$, where N = 2, 3, 4, ... differ in intensity by one-half. The intensity of the first element was much higher than the others to check for high intensity photographic errors. The ETP camera contained a Schott filter (1.0 N.D. - NG4), index matched to a Schott (UG-11) ultra-violet pass filter. The ETP arrays were photographed with Kodak Aerographic Duplicating (4421) film. The equivalent-target-plane was chosen to represent tangential focussing for a 0.60 meter lens and a 400 µm target diameter.

The second path directed the beam, through a long beam tube, into a near-field camera. The same photographic techniques used for the ETP

array were employed, except that the Schott NG4 was replaced by 1.0 and 0.6 neutral density (ND) (Kodak Wratten #96) filters.

The third path was used for lateral shearing interferometry. A 50% beamsplitter separated the beam into two components, each directed towards a fused silica shear plate, oriented at 45°. The shear plates, each with a 3.7 microradian wedge, were mounted in Aerotech (AOM110) gimballed mounts. The "S" polarized beam remained "S" polarized with respect to the horizontally oriented shear plate, but became "P" polarized with respect to the vertically oriented shear plate. The Fresnel reflection coefficients, for "S" and "P" polarized light at 45°, determined the filter attenuation needed in the camera. Aerographic (4421) film was used to photograph the interference pattern.

All mirrors, beamsplitters, and plates were interferometrically tested on a large aperture Fizeau, at a wavelength of 632.8 nanometers. Surface figures of $\lambda/10$ to $\lambda/20$, which translate to approxiamtely $\lambda/6$ to $\lambda/11$ at a wavelength of 351 nanometers, were measured over the clear aperture of the optical components. A final inspection, involving extensive cleaning procedures, was performed for each component.

The photographic results of the conventional beam characterization are shown in Fig. 4.5. High frequency (2-3 cycles/mm) interference fringes, due to the uncoated blocking filter, are present in the near-field photograph. Fine circular fringes, due to the Wratten #96 filters, are also present, but low visibility, high frequency fringes do not present a problem during film digitization for an image of this size.

**Equivalent Target Plane Array
(true size)**

0   (cm)   12.5
Near Field

Vertical Shear

Horizontal Shear

fig. 4-5

The equivalent-target-plane array shows five images, where each of the images, two through five, differs in intensity by one-half. The first (over-exposed) image does not differ in size or shape from the second image. Therefore, limited dynamic range (100/1) has not caused image distortion (deletion), and photographic methods are valid at a tangential focus position. The lateral shearing interferograms confirm that one or more wavelengths of optical path difference are distributed over the diameter of the beam. The rotation and expansion of the fringes, from three horizontal tilt fringes to fifteen vertically oriented fringes, seen in the horizontal shear pattern, indicates a large amount of defocus. The vertical shear pattern corroborates this. The difference in the number of fringes, between orthogonal views, indicates a different amount of defocus in the tangential and sagittal planes, which is referred to as astigmatism. The presence of coma is suggested by the tapering at one end, and the outward flaring of the fringes at the other end. Spherical aberration is indicated by the bulging of the fringes at the center of the interferogram.

The modulation depth of the fringes indicates that a long term temporal coherence existed. A quantitative analysis of the interferogram was not performed, since a visual inspection clearly indicated a severe aberration problem in the beam. A subsequent interferometric study of the frequency conversion crystals and crystal cells determined that they were the source of most of the phase error.

The conventional wavefront measurement techniques have provided a good characterization of the GDL frequency converted laser beam. Defects in the crystals were located, and distortions in the crystal cell were found. The equivalent-target-plane, representing tangential focus, was

accurately recorded. Furthermore, the effects due to a non-constant frequency conversion efficiency over the aperture were observed.

However, additional information is desired. The phasefront of the beam is not recorded in a readily useful form. The equivalent-target-plane camera has not been proved to be sucessful at the exact focus of the lens. The development of a holographic technique offers both a two-dimensional map of the phasefront, and a continuum of ETP images that approach the focal plane.

4.5   Reference Beam Formation

Two methods of deriving a local reference beam were investigated. The first method is characterized by the use of a transmitting diffuser in the reference arm of the holographic system as shown in Fig. 3-6. The second method incorporated a spatial filter in the reference arm of the interferometer as illustrated in Fig. 3-7.

A coherent optical processor was built to investigate the diffuser technique. Referring to Fig. 4-6, the incident beam was split into a phase modulated reference beam and an object beam, which were subsequently recombined at the holographic plate. A fused silica plate, ground with a 75 μm grinding abrasive was positioned at the front focal plane of the collimating lens. A region of uniform intensity was produced near the back focal plane of the lens. A glass plate with small, slowly varying phase irregularities, was inserted into half of the object beam. An Agfa-Gevaert 10E75 plate recorded the interference pattern. After plate processing, a repositioning of the plate was accomplished by viewing the
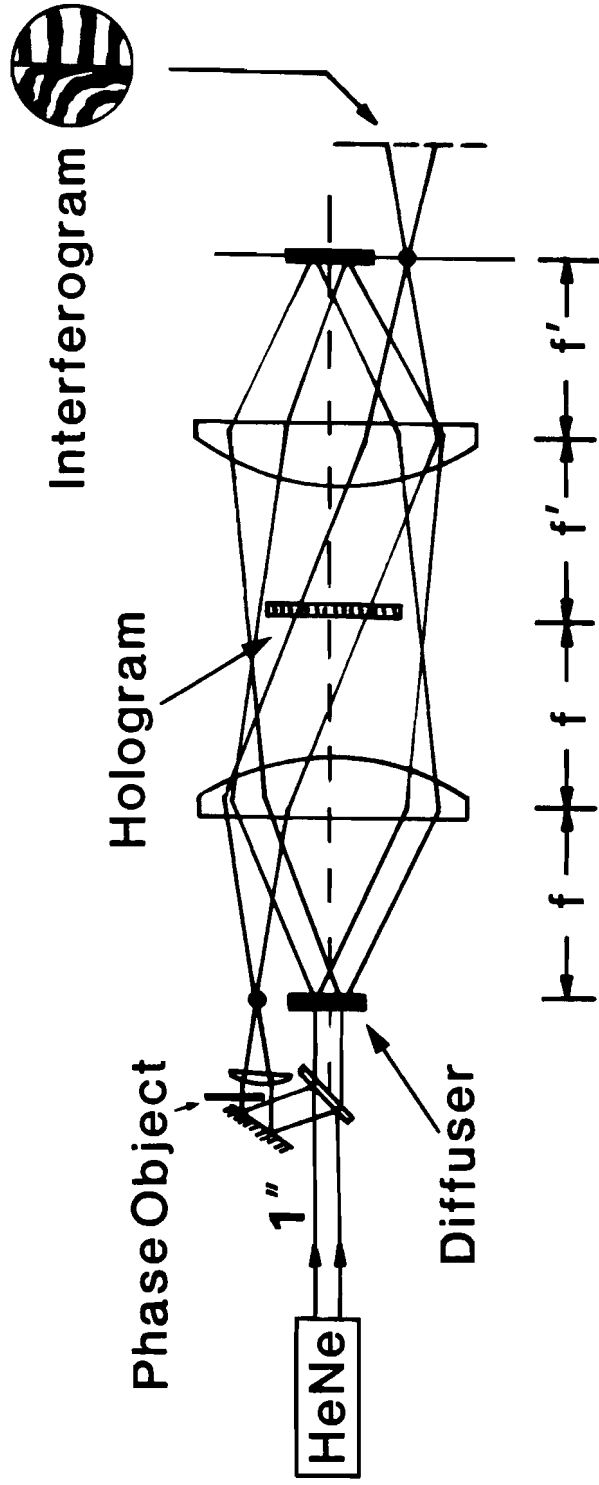
COHERENT PROCESSOR

FIGURE 4-6

bright reconstructed point at the back focal plane of the second lens. When both arms of the system were propagating light, the removal of the phase object from the object beam path produced an interference pattern characteristic of the phase object. Fringes of equal thickenss, i.e. tilt fringes, were observed upon returning the phase object to the object beam path.

Amplitude masks were introduced into the reference beam, just before the double diffuser. Amplitude fluctuations, similar to those found in the GDL laser beam, did not visibly affect the reconstructed image. Phase plates were introduced at the same location. The interference pattern contours, observed near the image plane, were not affected by phase changes made before the diffuser, but phase variations larger than a few wavelengths (λ= 632.8 nm) decreased the signal-to-noise ratio below viewing capabilities. Therefore, it was concluded that the double diffuser sufficiently disguised the reconstructing reference beam, in an experiment where both the recording and the reconstruction were achieved with the same continuous-wave laser. These results suggested that a region of the pulsed beam, over which phase fluctuations of about two wavelengths of light occur, could be disguised as a plane wave, and conversely, a CW plane wave could be used to reconstruct an object wavefront that was recorded with a pulsed reference beam.

Accurate repositioning of the holographic plate was extremely important. Alignment tolerances were similar to a holographic coupler. The holographic plate could be rotated approximately one milliradian, while the diffuser could be rotated no more than about 100 microradians. Longitudinal tolerances were loose for both the diffuser and the holographic plate, i.e. 100's of microns. The hologram could be laterally

displaced no more than about 25 μm., while the diffuser could be displaced on the order of several millimeters, due to the translation invariance characteristic of the coherent optical processor.

The phase-modulated reference beam study exhibited two serious drawbacks which precluded an attempt to applying the technique to the pulsed laser beam. Large light losses at the diffuser caused the low power level, CW laser to produce extremely weak reconstructions. Secondly, critical alignment techniques had not yet been demonstrated and would require development.

Spatial filtering techniques are more compatible with a weak reconstructing laser beam. Preliminary experiments showed that less light is lost at a spatial filter pinhole than at a diffusing surface, for the same level of amplitude uniformity in each case. It was found that a hologram's diffraction efficiency was greater for a two-plane-wave recording. Additionally, spatial filtering techniques involved relatively easy alignment during the reconstruction stage of the holographic process.

Two problems were anticipated during the theoretical study of spatial filtering. Conservative calculations predicted possible pinhole closure due to high intensities present at the focus of a well corrected lens. Secondly, laser induced breakdown of air was presumed probable, for systems without a vacuum spatial filter. It was intended that a preliminary study of a nonfocussing technique (refer to section 3.6) be conducted prior to the spatial filtering investigation. However, an accidental replacement of a negative beam-expander by a positive objective into a Galilean up-collimating system produced a study of spatial filtering methods earlier than had been planned.

Before studying the effects of the spatial filtering of a portion of the original laser beam, it was necessary to determine that enough energy could be propagated through the focus of a diffraction limited, F/5 to F/10 lens, to sufficiently expose a holographic plate. Figure 3-8 schematically illustrates the set-up used to photograph the light that propagated past the focal plane. A demagnified laser beam with a diameter of 62.5 millimeters, was transported to the input side of a Tropel (model 280-F/4) collimator. This lens was antireflection coated for a range of wavelengths centered near $\lambda = 351$ nm, and was fabricated from ultraviolet grade fused silica. The entrance pupil of the lens selected an eight millimeter portion of the central region of the beam. The focussed beam was recollimated using an F/3 aspheric lens, with a focal length of approximately 600 millimeters, resulting in a magnification of $M = -f_c/f_o = -50$. A near field camera, equipped with a shutter and blocking filter, recorded the final image on Aerographic (4421) film.

The power density, η, at the focal plane of the objective is calculated according to equation 3-37:

$$\eta = \frac{E}{\tau A} = \frac{E_o K}{\tau \pi (1.22 \lambda f/d)^2} \qquad (4-1)$$

where E_o is the ultraviolet light energy in joules, τ is the pulse-width (FWHM) in seconds, and A is the area of the theoretical Airy disc $(A = \pi (1.22 \lambda f/d)^2)$. The fraction of the beam energy that is contained within the area of the Airy disc, K, contains a product of estimated attenuations: the reflectances and transmittances of the optical compon-

ents, the area ratio between the input aperture and the incident beam, the fraction of energy at the Airy disc, and the fraction of the average beam energy at the point of reference beam selection. The overall attenuation is estimated to be: $K = (.04)(.9)^3(d/6.3)^2 (.84)^2 = d^2/2000$. The largest error in this calculation arises from the estimation of the fraction of average beam energy at the point of reference beam selection; K is believed to be the attenuation to within a factor of three. A computation of 4-1, where the pulsewidth is taken to be 850 ps, $\lambda = 351$ nm, and $K=d^2/2000$, yields an expression for the power density at the focus of a lens in terms of the laser beam's energy, the diameter of the entrance pupil, and the focal length of the objective, as shown below:

$$\eta = \frac{E_0(D)^4(10^{14})}{(f)^2} \quad \text{watts/cm}^2$$

(4-2)

Table 4-1 lists the shot numbers and the calculated power densities at the focal plane, and indicates the observation of air breakdown for various holographic experiments. Figure 4-7 illustrates the results with an air breakdown threshold of approximately $1x10^{13}$ W/cm^2. The data is self consistant, and agrees with extrapolated data from the cited references to within the error associated with the attenuation estimation.

When air breakdown occurred, concentric regions of varying density were recorded with a very dense region in the center, and all high frequency information was absent. Figure 4-8 (shot number 7521) represents a power density of about $6x10^{12}$ W/cm^2, and shows that in the absence

TABLE 4-1: FOCAL PLANE ENERGY DENSITIES

Shot Number	E_0 (joules)	Focal (cm) Length	Diameter (mm)	Energy (Watts/cm^2) Density	Breakdown
7882	19.6	2.75	3.8	$5.4 \cdot 10^{12}$	N
7859	8.95	2.75	3.8	$2.5 \cdot 10^{12}$	N
7858	10.5	2.75	3.8	$2.9 \cdot 10^{12}$	N
7720	9.57	2.75	3.8	$2.6 \cdot 10^{12}$	N
7644	11.7	2.75	5.5	$1.4 \cdot 10^{13}$	Y
7616	12.2	2.75	4.0	$4.1 \cdot 10^{12}$	N
7614	15.9	1.20	8.0	$4.5 \cdot 10^{14}$	Y
7578	18.7	1.20	3.0	$1.1 \cdot 10^{13}$	N
7546	14.0	1.20	3.0	$7.9 \cdot 10^{12}$	N
7528	10.9	1.20	3.0	$6.1 \cdot 10^{12}$	N
7521	10.0	1.20	3.0	$5.6 \cdot 10^{12}$	N
7519	16.6	1.20	5.0	$7.2 \cdot 10^{13}$	Y
7515	29.0	1.20	8.0	$8.2 \cdot 10^{14}$	Y
7501	8.45	1.20	8.0	$2.4 \cdot 10^{14}$	Y

AIR BREAKDOWN
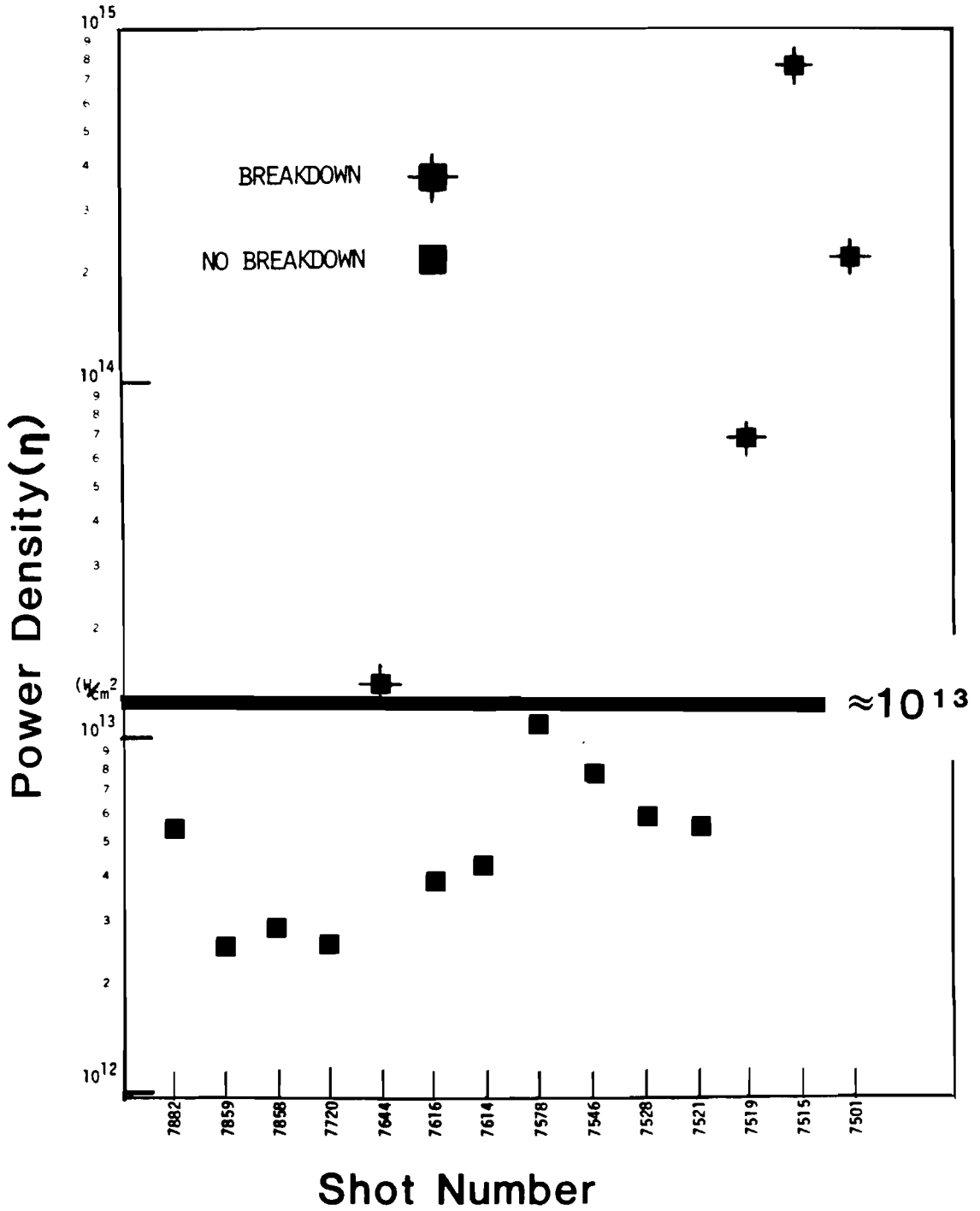
FIGURE 4-7

of air breakdown, the high frequency detail is restored. This phenomenon was observed independent of the presence of a spatial filter pinhole at the focal plane; therefore, pinhole closure effects were ruled out. Additionally, the densities on the photographic film indicated that the majority of the light passing through the input aperture reached the film plane. The pinholes were examined under a Zeiss Universal metalurgical microscope. No trace of damage was observed. Therefore, we conclude that the threshold for pinhole closure effects is greater than the threshold for the breakdown of air.

During the course of the spatial filtering experiments, the Tropel objective exhibited coating imperfections, and was replaced by an Edscorp objective, with a focal length of 2.75 centimeters. An aperture of 3.8 mm diameter was positioned at the front focal plane. A magnification of approximately 22 produced an 83 mm diameter, collimated beam at the image plane.

A Spectra-Physics model 165 Argon Ion Laser, equipped with ultraviolet coated mirrors, was available as an alignment and a reconstruction laser. After replacement of the BeO plasma tube, it reliably operated at a 10 milliwatt ouput level at a wavelength of $\lambda = 351.1$ nm. A GDL laser pulse was necessary for initial alignment. The pulsed beam propagated through a reference crosshair and into Kodak Linagraph paper, which recorded the diffraction pattern from the crosshair. The crosshair and it's near field image were two reference points used to align the argon laser coincident with the pulsed beam, to within approximately 50 to 75 microradians. The objective and collimating lenses were aligned onto

this reference line. The accuracy of this technique was sufficient for the alignment of the 100 μm pinhole, but a more accurate technique was needed for the placement of a 15 μm pinhole.

A sheet of transparent, 12.7 μm thick Mylar was accurately placed at the focal plane, by viewing the spatial frequency content of the transmitted beam. A 35 μm wide, hourglass shaped tunnel was drilled with the pulsed beam using an average power density of about 5×10^{12} W/cm^2. (The tunnel was analyzed with the Zeiss Universal microscope.) The argon laser was then aligned through the drilled hole, with a calculated accuracy of 30 to 40 microradians. The Mylar was replaced by the spatial filter pinhole, and was aligned to within $\pm$ 1 μm laterally and to within $\pm$ 4μm longitudinally, by viewing the diffraction pattern in the collimated beam at the image plane. The hole drilling technique was also more convenient for one person to align.

Figure 4-8 shows the expanded image of the portion of the laser beam that was selected by the input aperture. It indicates that a full range of spatial frequency components were contained in the unfiltered reference beam. Not having the system flexibility to select another, more uniform portion of the beam, the spatial filtering of this reference beam was studied. Figure 4-9 shows the results of filtering with a 100 μm pinhole. The higher spatial frequencies were filtered out, but modulation characteristic of truncating the Airy distribution at a radial point greater than the second zero appeared. The scale of the modulation is similar to that observed during a CW spatial filtering study. Figure 4-11 shows the results of filtering a central portion of the argon laser with a 100 μm pinhole.

For figures 4-8 to 4-12 and 4-16 to 4-19, each of the four quadrants is a different way of illustrating the same intensity distribution, as shown below.

Original Print	Azimuthally Averaged Profile
3-Dimensional Intensity Plot	Iso-Intensity Contour Plot

The original negative, or a positive print, has a limited quantitative usefulness before it is processed with an appropriate calibration curve. On the other hand, it does exhibit high frequency detail, which is lost in the averaging algorithms of the other three representations. The azimuthally averaged profile is a measure of the radial energy distribution. The false three-dimensional intensity plot is a graphic illustration of the two-dimensional information that is missing from the azimuthally averaged energy distribution. The iso-intensity contour plot is a quantitative measure of the same two-dimensional intensity distribution. A description of the image processing system, used to process and analyze photographic negatives, is contained in Appendix A.

Figure 4-10 shows the photographic and image processing results of spatially filtering the pulsed reference beam with a 15 μm pinhole. A comparison with Figs. 4-8 and 4-9 shows that nearly all of the original spatial frequencies were removed. A slowly varying amplitude fluctuation, corresponding to a spatial frequency of about 20 cycles over the full diameter of the original beam, remained. About 60 percent of this

PULSED REFERENCE NEAR FIELD –
NO PINHOLE
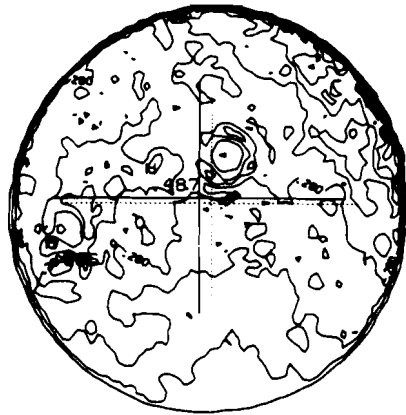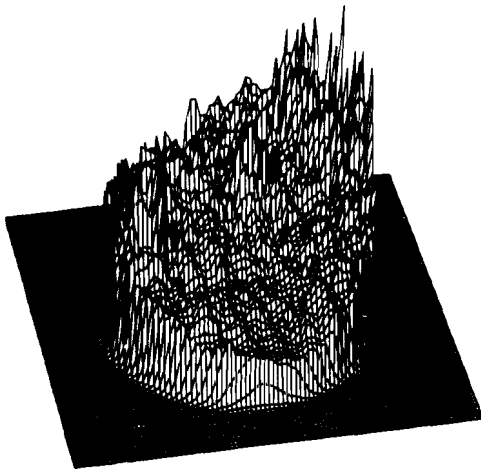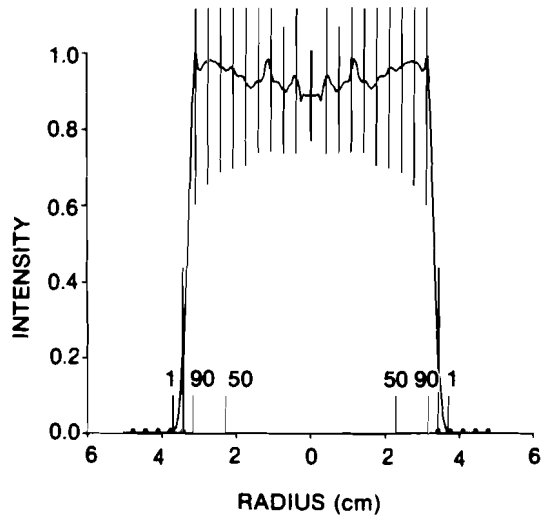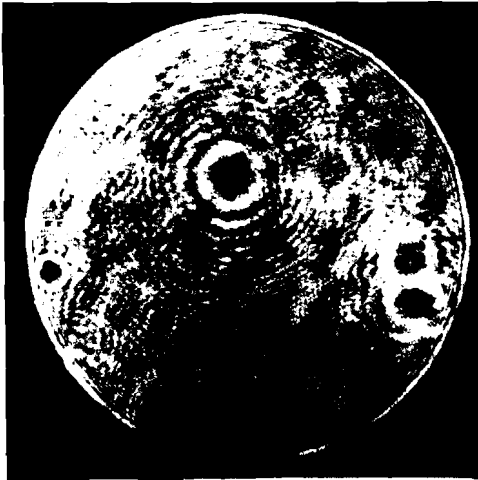
fig. 4-8

PULSED REFERENCE NEAR FIELD –
100-μm PINHOLE

UR
LLE
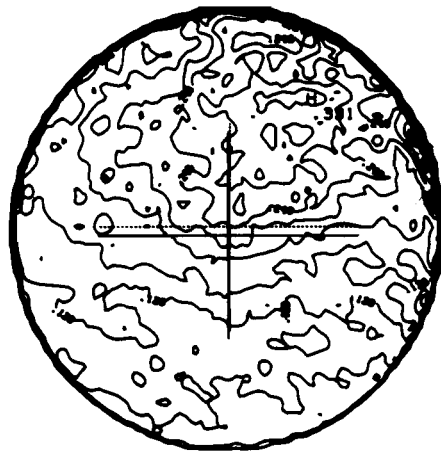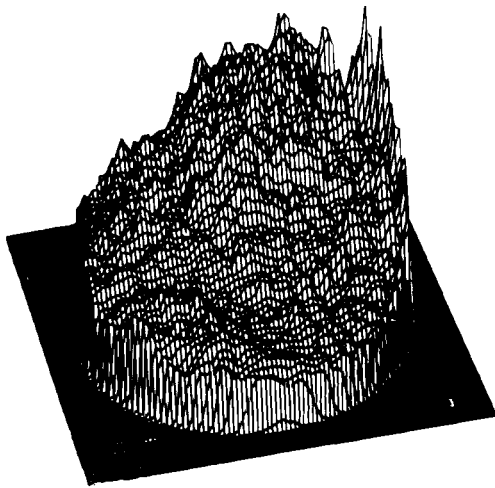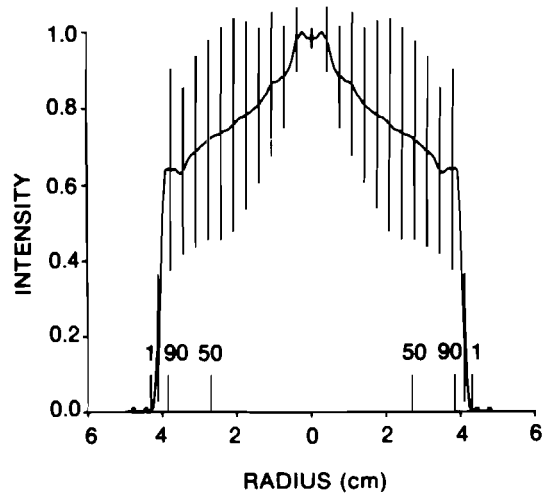
fig. 4-9

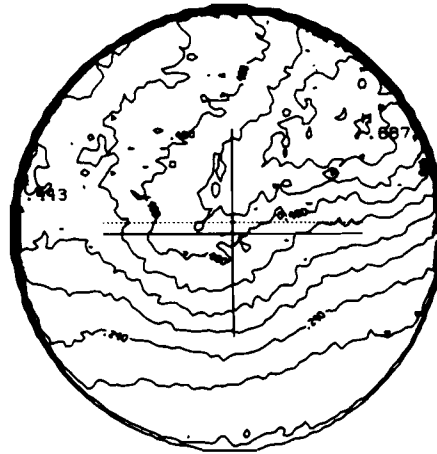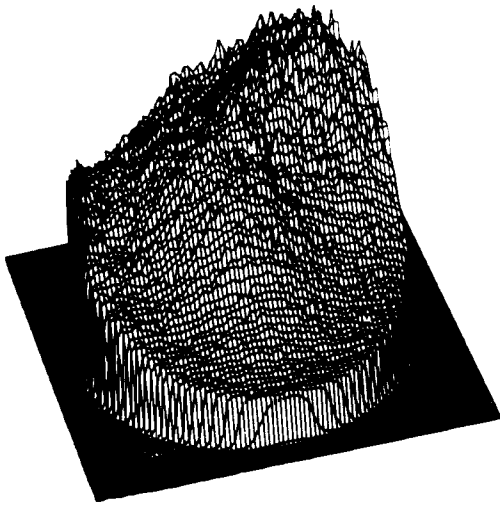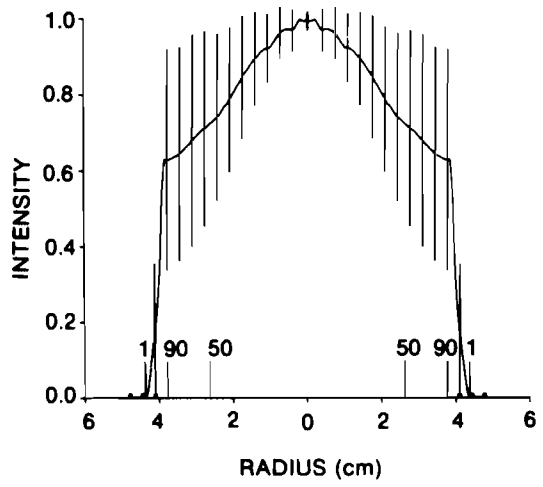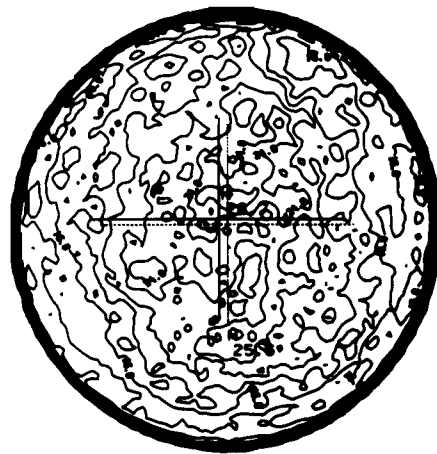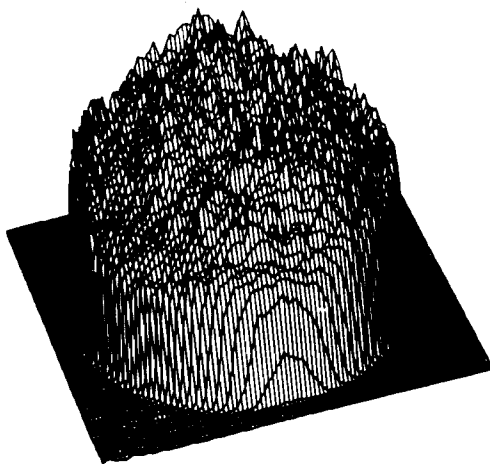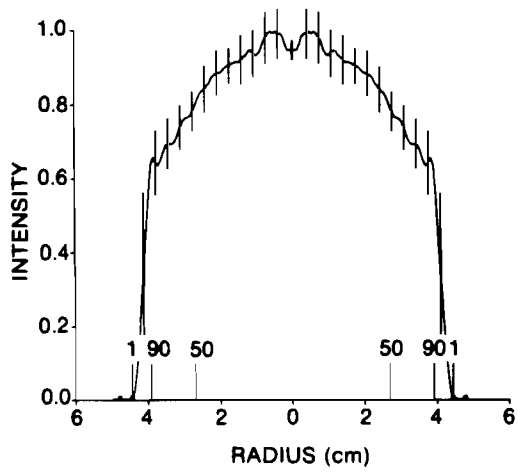# PULSED REFERENCE NEAR FIELD –
15-μm PINHOLE

fig. 4-10

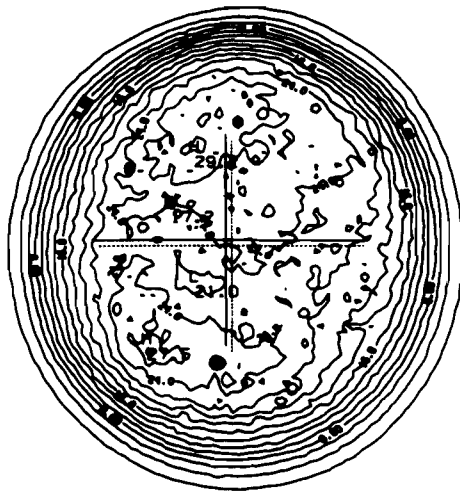fig. 4-11
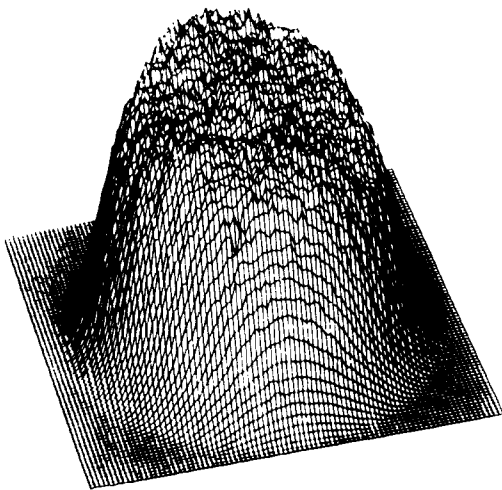
CONTINUOUS WAVE REFERENCE NEAR
FIELD – 15-μm PINHOLE
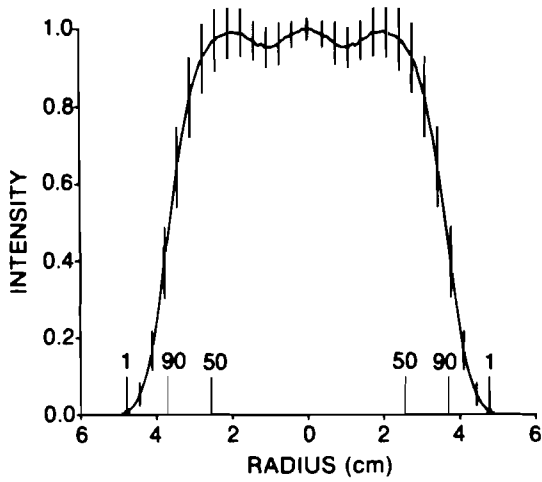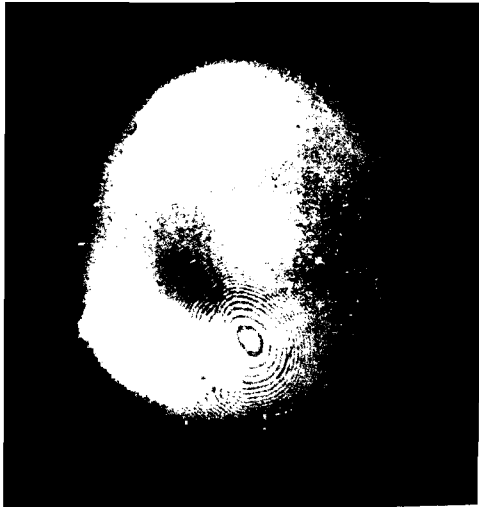
fig. 4-12

beam's area was needed to act as the reference wave. The most uniform, usable area contained a slowly varying amplitude of ± 25% in intensity. Figure 4-12 shows the results of spatially filtering the central region of the argon laser with a 15 μm pinhole. Intensity variations of about ± 10 percent are contained in an azimuthally averaged envelope of ± 5 percent modulation. This represents the upper limit of amplitude uniformity that is possible when spatial filtering the pulsed reference beam with a 15 micron pinhole, and operating at approximately F/7. Pinhole diameters between 5 and 10 μm satisfy condition 3-37a, but pinholes within this range were not available. The 15 μm pinhole truncated the far field distribution somewhere between the second and third zeros of the Airy pattern. Figure 4-10 represents the reference beam that was used during the holographic recording of the object wavefront.

4.6   Holographic Experimental Set-Up

Many of the design features and techniques, mentioned in the discussions of preliminary experimental work, were incorporated into the design of the holographic system. Figure 4-13 illustrates the basic experimental set-up. The laser beam was transported to the lower table by means of an uncoated, wedged beamsplitter. The beam was demagnified by means of a Galilean telescope, which was composed of a positive 10 meter lens and a negative 5 meter lens. The low power output from the argon laser made it necessary to establish an intermediate reference beam. The argon alignment laser that normally propagated through the crystals for

HOLOGRAPHIC EXPERIMENTAL SET-UP

Argon Ion

Filter

$1\omega \rightarrow 3\omega$

Tank

Wavefront Storage

Hologram

Reconstruction

N.F.
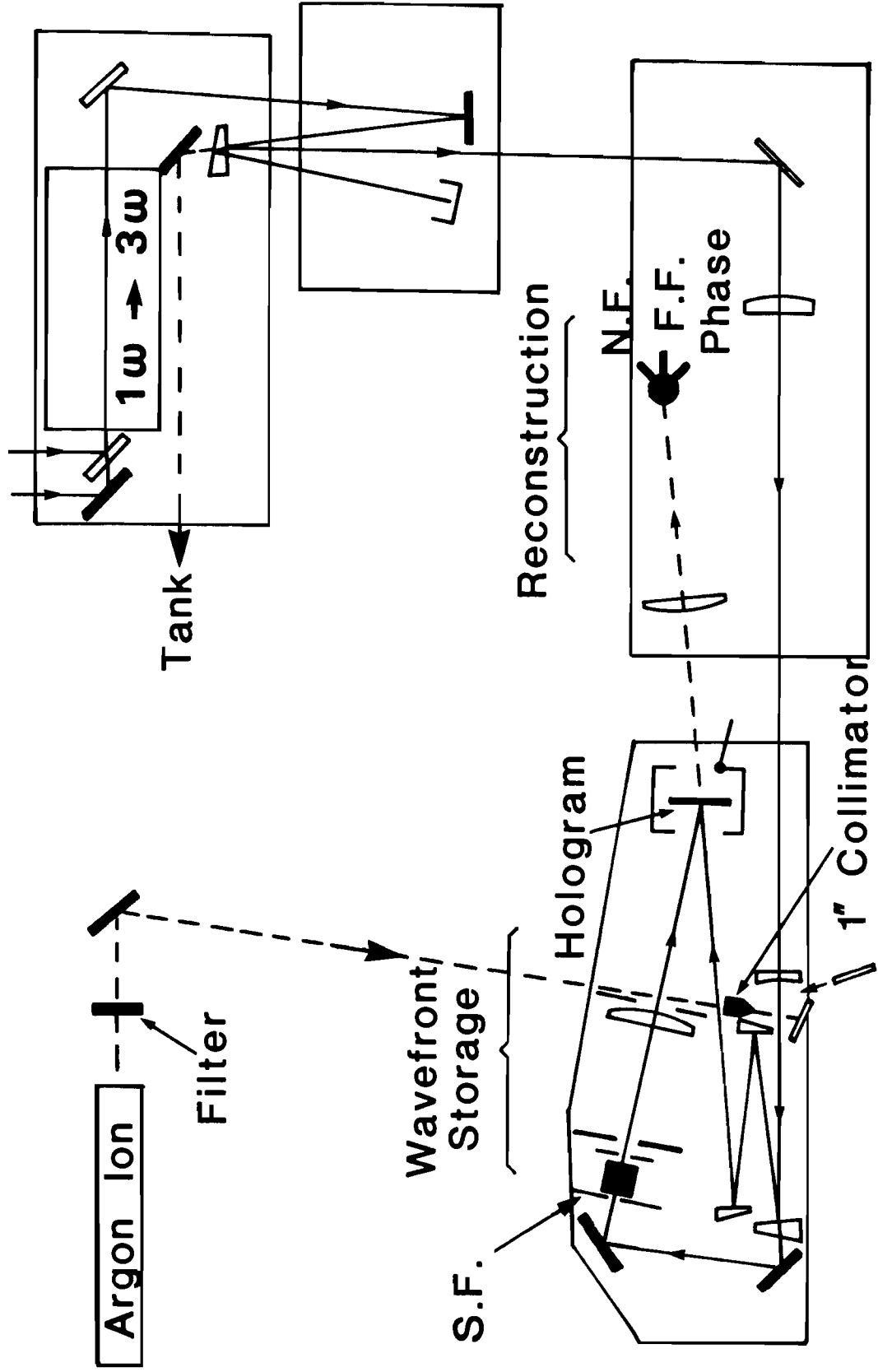
F.F. Phase

S.F.

1" Collimator

FIGURE 4-13

system alignment was used to set two crosshairs onto the path of the pulsed beam. A second argon laser beam was split from the first, collimated and colinearly aligned with the path defined by the two crosshairs. This newly created alignment beam made it possible to align each lens in the telescope, by viewing it's back reflections. The ultraviolet beams were viewed by means of fluorescence from unexposed and undeveloped Polaroid #57 positives. The position of the telescope was chosen based on the paraxial raytracing of ghost images, avoiding excessive loading on any of the upstream optical surfaces.

After demagnification, an uncoated, wedged beamsplitter split the beam into a reflected object beam and a transmitted reference beam. The object beam encountered two more front surface reflections from index-matched wedges before arriving at the holographic recording plane. Two highly reflecting mirrors transported the reference beam to the entrance pupil of the spatial filtering system. A central region of the beam continued through the input aperture, passed through focus to be filtered, and was recollimated to produce a nominally plane wave. A third argon laser beam, after passing through a one inch diameter Tropel collimator, was injected into the beam path, before the wedged beamsplitter, by means of a motorized kinematic mirror. (The alignment of this CW beam was described in Section 4.4 on reference beam formation.) The spatial filter (Newport Research model 900) was equipped with a micrometer adjustment for each of three orthogonal axes. The axial adjustment set the distance between the pinhole and the objective, while two lateral adjustments centered the pinhole on axis. The axial separation between the spatial filter and the collimator was adjusted by means of an additional axial stage. A horizontal shear plate was placed after the

collimator to obtain a measurement of the phase of the reference beam. Correct alignment was confirmed when horizontal tilt fringes were observed over the whole field. Highly modulated fringes were obtained with an argon laser operating current of between 5 and 10 percent above threshold. Neighboring spectral lines ($\lambda \neq 351.1$ nm) were blocked with a narrow bandpass interference filter.

The holographic plate holder (Newport Research model 540) was mounted securely onto an angular stage. With a glass plate in the holder, the reference and object beams were reflected back onto each other to insure that the plate normal bisected the full angle between the two paths. A full angle choice of 15° was dictated by space constraints. Many beam blocks and baffles were needed to block reflections, ghost images, and unconverted 2ω light. The recording apparatus was totally enclosed, with a computer controlled shutter open for 20 seconds during the pulse.

4.7   Wavefront Recording and Reconstruction

The use of a Galilean down-collimating telescope allowed a compromise between studying the GDL pulsed wavefront and using standard format, 5" by 4", Agfa-Gevaert 10E56 holographic plates. Conventional techniques, discussed in Section 4.3, were applied to the object beam, in order to obtain a point of reference for comparison with the reconstructed wavefront. A series of pulsed shearing interferograms were recorded to iteratively adjust the spacing between the elements of the Galilean telescope, to determine the phase effects due to the optical components in

the object beam path, and to obtain a point of reference for phase-front comparison. Additionally, near-field and far-field distributions of the object beam were photographed at power levels similar to those needed for the correct biasing of the holographic plate.

The preliminary design balanced the reference and object beams at an intensity ratio of ten to one. Losses at the spatial filter and the wedged beamsplitter, together with a nonuniform intensity distribution at the point of reference beam selection, decreased this ratio to about three to one, for the average object beam intensity. A ratio of about one to one occurred in regions where the object beam was most intense and the reference beam was at it's lowest intensity value. The bias level was controlled by selecting the infrared energy at a known third harmonic conversion efficiency for that energy. The exposed plates were processed according to the procedures outlines in Appendix B. Unintentionly over-exposed plates were bleached to obtain a greater diffraction efficiency.

Measurement of the wavefront reconstruction was accomplished in a three part procedure that utilized conventional methods. The one inch diameter Tropel collimator was removed from the argon laser beam path to allow more light to reach the spatial filter. The separation between the objective and collimator was adjusted to produce a plane wave, while the pinhole was accurately adjusted to produce a uniform intensity distribution. The reconstructed beam was directed to the lower right table in Fig. 4-13. The near field intensity distribution was recorded on Aerographic (4421) film. A horizontal lateral shearing interference pattern was recorded on Polaroid #57 positive print film. A one dimensional equivalent- target-plane array, created from the same focussing lens and

etalon used to obtain the pulsed ETP, was photographed with Aerographic (4421) film.

The final experiment at $\lambda = 351$ nm, conducted on the reconstructed object wavefront, produced a two-dimensional measurement of the phase-front. A bleached hologram was placed at the original recording plane. A point-diffraction interferometer (Smartt PDI) was positioned at the focus of an F/3 targeting lens. An ultraviolet vidicon camera was placed immediately behind the PDI to aid in the alignment of the interfero-meter. Visualization of the fringes was obtained by accurately adjusting the spatial controls of the PDI while viewing the television image. Un-like lateral shearing interferometry, sufficient modulation depth of the fringes could be obtained at maximum current through the argon laser tube, since no time differential existed between the object and reference wavefronts. Both a near maximum CW laser output and an increased dif-fraction efficiency due to the bleaching of the hologram were needed for the successful vidicon detection of the interference pattern.

An adjunct experiment was performed to determine the requirements for holographic interferometry. A holographic interferometer, similar to that shown in Fig. 4-13, was constructed on a neumatically stablized NRC magnetic table. The reconstructing and reference beams were derived from a Helium-Neon laser. The reconstructed wavefront was combined with the directly transmitting wavefront from the other arm of the system to form two-beam inteference fringes. Interferograms were recorded on Polaroid #57 positive print film.

4.8   Experimental Results

All original data, obtained with conventional or holographic techniques, is in the form of either photographic negatives or Polaroid positives. Intensity distributions, recorded as density variations, must be intensity corrected before relevant analysis can be performed. Interferograms can be analyzed directly, but it is advantageous to make high contrast positive prints of those that were recorded as negatives.

Figure 4-14 shows both the pulsed and the reconstructed object beam lateral shearing interferograms. A direct comparison can be made since the amount of shear is, within a few percent, the same. The time dependent phase effects, clearly evident in the pulsed interferogram, are reduced in the reconstructed interferogram. The number of fringes, as well as their orientation, is the same in each pattern. Small, rapidly varying changes in the shape of each fringe, of the same magnitude observed between measurements of different laser pulses, are present. Additionally, small, slowly varying differences in the shape of the fringes are observed. Referring to equation 2-1, the sensitivity of the shear plate to defocus is calculated in the following way.

$$\underline{DEFOCUS} \quad - \quad W(x,y) \quad = \quad D(x_0^2 + y_0^2) \tag{4-3}$$

where D is the optical path difference (OPD) at the edge of the field, and (x_0, y_0) are the normalized coordinates. The shift of fringes corresponding to a particular value of D, is expressed by,
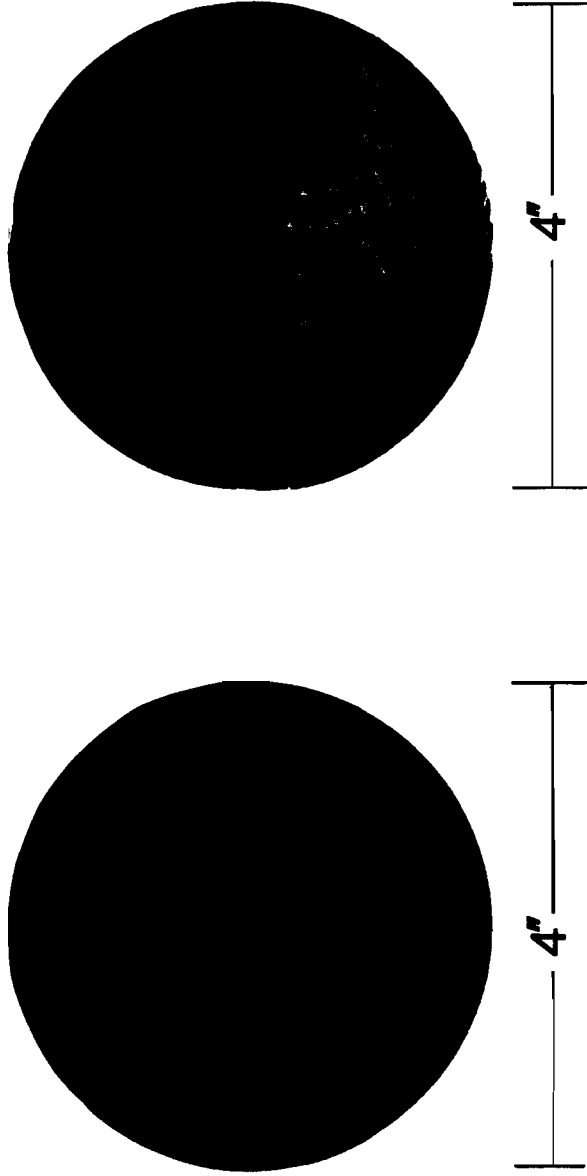
SHEARING INTERFEROGRAMS

reconstructed

pulsed

fig. 4-14

FIZEAU INTERFEROGRAMS

K-649O   A-G 10E56

fig. 4-15

$$\Delta W = n\lambda = \frac{2 \cdot OPD_{max.} (x_m - S)S}{x_m^2} \tag{4-4}$$

where $D = OPD_{max.}$, S is the shear, and x_m is the beam radius. From Fig. 4-14, S = 18 mm, and x_m = 31.3 mm, so that the change in the number of fringes at the edge of the field is given by,

$$\text{\# Fringes} = OPD_{max.} (0.5) \tag{4-5}$$

The sensitivity of the shear plate is fixed, but the accuracy of the interferogram is dependent on the quality of the fringes. Since in this case the position of a fringe can be measured to within one-fourth of the average fringe separation, $OPD_{max.}$ = 0.25/Q5 = 0.5, and half-wave accuracy is obtained. The OPD variations over the area of an Agfa-Gevaert 10E56 holographic plate were measured with a Fizeau interferometer. Figure 4-15 shows an interferogram that represents the cumulative phase from passing twice through the plate at λ = 632.8 nm. OPD variations of between one-half and one wave at λ = 351 nm occur over a 2.5" diameter area. Therefore, the slowly varying changes in the position of the fringes, corresponding to optical path differences of about one-half to one wavelength of light, are readily attributable to the holographic plate's OPD variations.

Near field intensity distributions, of the pulsed and reconstructed wavefronts, are shown in Figs. 4-16 and 4-17 respectively. Unfortunately, the photographs were recorded at different time periods, and a
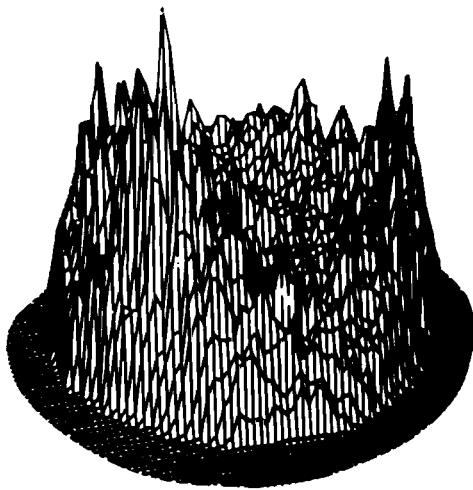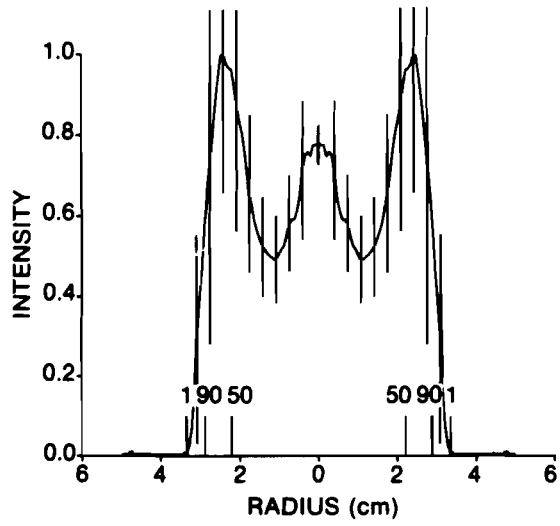
OBJECT BEAM
NEAR FIELD

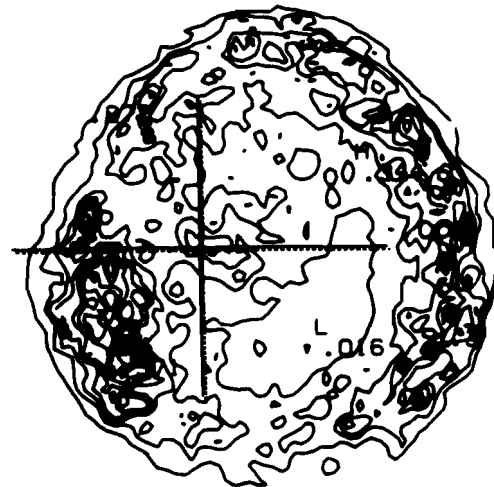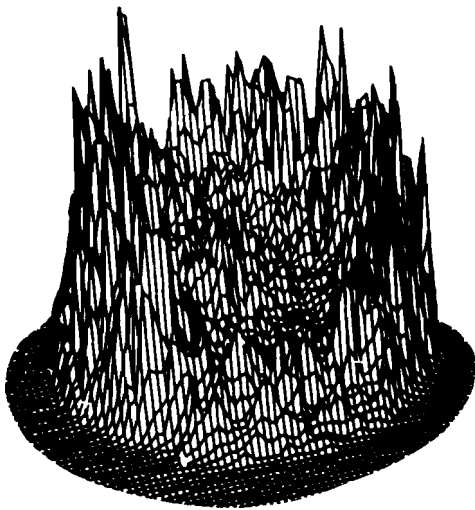UR
LLE

(true size)

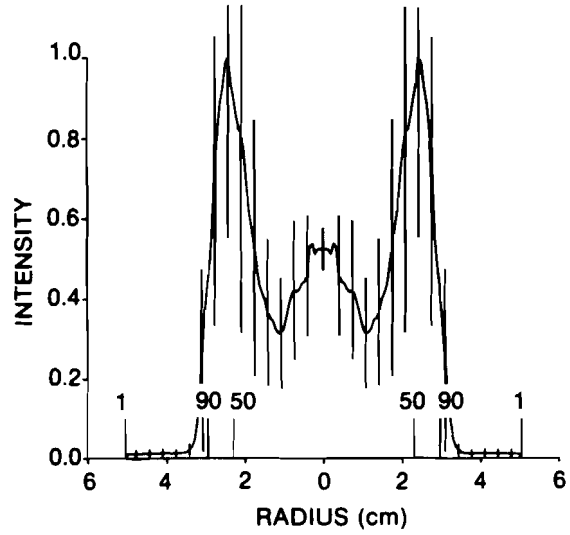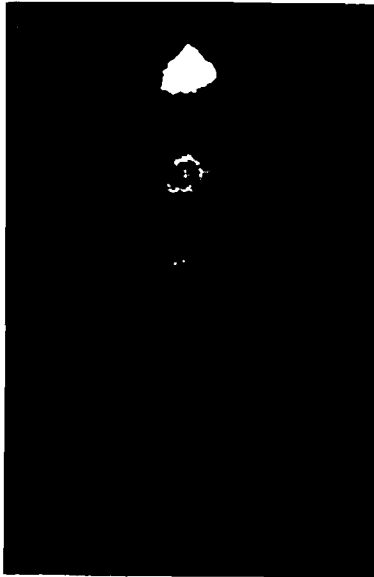fig. 4-16

UR
LLE

(true size)

fig. 4-17

direct comparison requires the assumption that the alignment of the laser system remained constant. A comparison between the negatives shows that most of the middle (0.2-2.0 lines/mm) and low (.02-0.2 lines/mm) frequency detail is recovered during reconstruction. The high (> 2 lines/min) frequency detail is veiled by various sources of noise. The azimuthally averaged plots show good agreement for the radial energy distribution, but indicate a nonlinear amplitude reconstruction. The peak-to-valley ratio is 50% greater for the reconstructed near-field distribution. The range of the high frequency variations, indicated by the error bars, is larger for the reconstructed near field distribution which, again, indicates nonlinear amplitude reconstruction. The iso-intensity plots best illustrate the effects due to the amplitude nonuniformities in the pulsed reference beam. Recalling Fig. 4-10, the reference beam intensity was largest at the top, right region, and was lowest at the bottom of the distribution. The pulsed and reconstructed contour plots differ the most at these same two locations.

The pulsed and reconstructed equivalent-target-plane photographs, Figs. 4-18 and 4-19, show strong similarities, despite the nonlinear amplitude reconstruction observed in the near field intensity distributions, and the phase variations observed in the shearing interferometry. The second image of each array was sufficiently dense for intensity correction and image processing. The azimuthally averaged plots are similar in shape, but indicate an even greater nonlinear effect. The reconstructed peak-to-valley ratio is about 90% larger than the pulsed ratio. The iso-intensity plots show a close resemblance, but the nonlinear reconstruction is apparent by the depression of the lower intensities. The first element of the reconstructed array shows an additional image to the
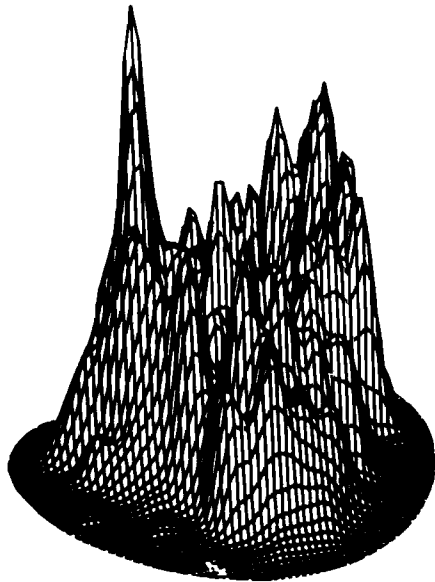
PULSED EQUIVALENT
TARGET PLANE

UR
LLE
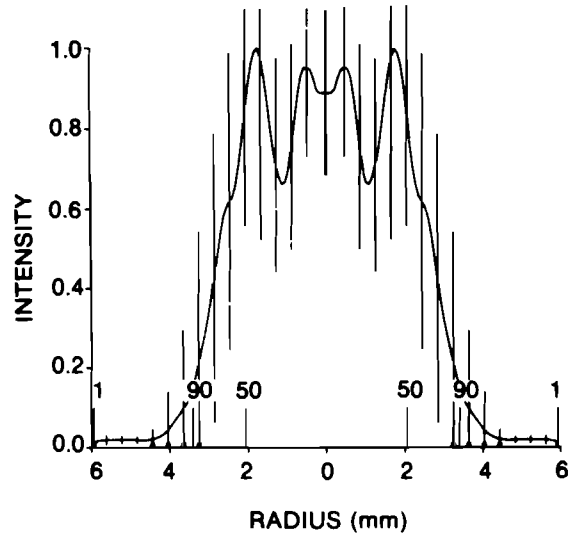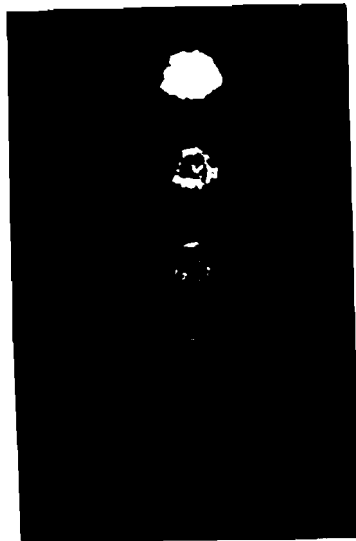
(true size)

INTENSITY

1.0

0.8

0.6

0.4

0.2

0.0

1   90   50   50   90   1

6   4   2   0   2   4   6

RADIUS (mm)

fig. 4-18

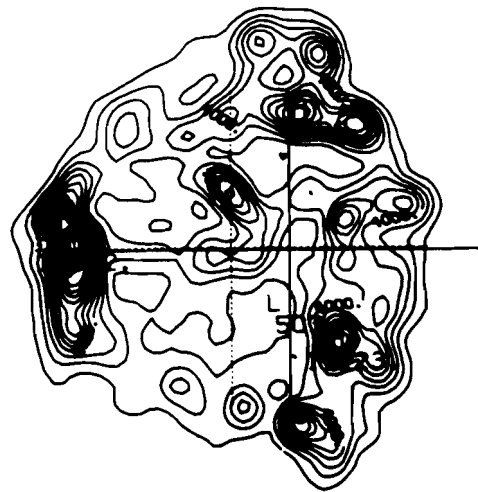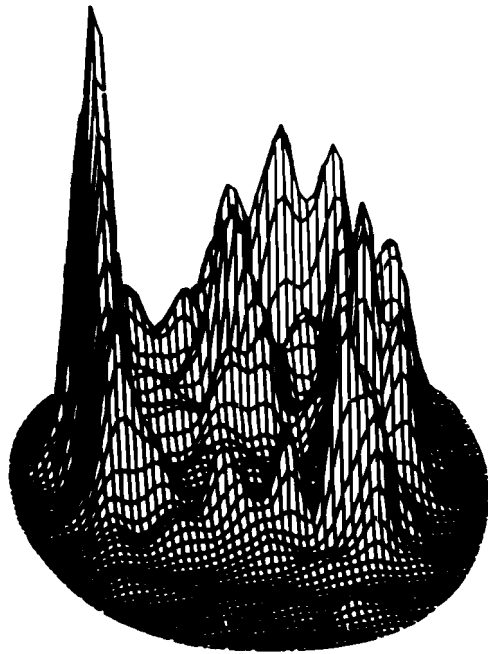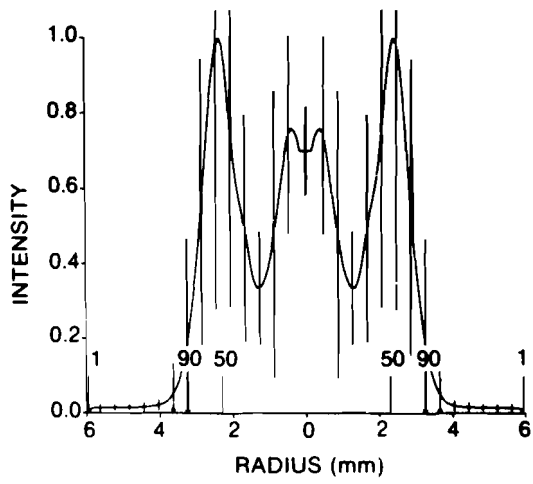# RECONSTRUCTED
EQUIVALENT TARGET PLANE

(true size)

fig. 4-19

left of the primary image. This could be a higher order reconstruction due to the nonlinear recording or a ghost reconstruction due to secondary reflection at the holographic plate during recording.

An interferogram obtained with the point diffraction interferometer, shown in Fig. 4-20b, represents the cumulative phase distortion due to the object beam, the holographic plate, the focussing lens, and the defocus introduced by the axial position of the PDI pinhole. Large variations in the fringe visibility, inherent in the application of the PDI to highly aberrated phasefronts are observed.

Figure 4-20a shows an interferogram obtained from a holographic interferometer at λ = 632.8 nm. In this case, the OPD variations of the holographic plate are removed from the interference pattern by passing the reference beam through the plate, coinicident with the reconstructed beam. Eight to nine defocus fringes are counted from center to edge. This corresponds to 8.5 wavelengths of defocus at λ = 632.8 nm, or about 15 wavelengths at λ = 351.1 nm. According to equation 4-5, the seven to eight fringes over half of the field of the shearing interferograms also corresponds to about 15 wavelengths of defocus at λ = 351.1 nm. With defocus as the measure of comparison, the shearing interferometry is in good agreement with holographic interferometry. Additionally, the two methods show comparable defocus in the vertical direction, thus they show comparable amounts of astigmatism.
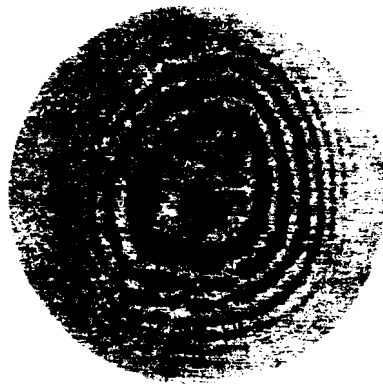
2-BEAM INTERFEROGRAMS

fig. 4-20a: Holographic

fig. 4-20b: PDI

4.9   Conclusions

Conventional wavefront measurement techniques were successfully applied to a frequency converted high-peak-power laser. Accurate near-field and quasi-far-field intensity distributions were photographically recorded. Lateral shearing interferometry was instructive in qualitatively determining the phasefront, and provided a point of reference for comparison with holographically reconstructed phasefronts.

The wavefront recording and reconstruction of a HPPL were successfully demonstrated. The usefulness of describing a focussed portion of the beam with Fourier transform theory was verified and spatial filtering impracticalities were overcome in creating a local reference beam. Despite nonlinear amplitude recording, reconstructed near-field and quasi-far-field intensity distributions closely resemble those obtained from conventional techniques. Accurate phasefront reconstruction was achieved, with the OPD variations of the holographic plate limiting the accuracy to between one-half to one wavelength (λ = 351 nm). Additionally, the application of PDI and holographic interferometers to the reconstructed phasefront demonstrated the feasibility of performing two-beam interferometry on the CW reconstruction of the pulsed wavefront.

REFERENCES

1. W. Seka, et. al., "High Power Phosphate-Glass Laser System: Design and Performance Characteristics", Applied Optics, Vol. 19, #3, Feb. 1980, P. 409

2. G.F. Albrecht and J. Bunkenburg, "Active-Passive Mode-Locked Oscillator Generating Nanosecond Pulses", Optics Communications, Vol. 38, # 5,6, Sept. 1981, p. 377

3. W. Seka, et. al., "GDL: A High Power .35 um Laser Irradiation Facility", IEEE-J.of Q.E., Vol. Q.E.-17, #9, Sept. 1981, p. 1689

4. S.D. Jacobs and J.A. Abate, "Compatability of Transmissive Optical Materials with High Intensity 0.351 um Laser Radiation", Poster Paper at CLEO(Th B11), June, 1981

V. CONCLUSIONS AND SUGGESTIONS FOR FUTURE RESEARCH

5.1   Conclusions

Holographic techniques have been successfully implemented on an ultraviolet, frequency converted, high-peak-power laser to obtain continuous-wave reconstructions for conventional wavefront measurement. Reconstructed near-field and quasi-far-field intensity distributions closely resemble those obtained from conventional techniques. Reconstruction of the near-field intensity profile was achieved with an overall resolution approaching 2 lines/mm, and an azimuthally averaged, peak-to-valley intensity modulation increase of about 50%. The resolution of the reconstructed quasi-far-field intensity profile was nearly the same, 1-2 lines/mm, but the peak-to-valley intensity modulation increase was 90%. The resolution was limited by both halation effects and scattering at the holographic plate. The intensity modulation increase is symptomatic of a nonlinearly recorded amplitude distribution, attributable to an excessive object-to-reference beam intensity ratio and amplitude nonuniformities in the pulsed reference beam.

Although the reconstructed intensity profiles closely resemble those obtained from conventional methods, we conclude that this technique does not presently reproduce the HPPL amplitude distribution with sufficient accuracy to replace conventional intensity measurement techniques. However, it is believed that several improvements can be made, especially with regard to system flexibility, that would greatly reduce the sources of noise and the sources of nonlinear amplitude recording. These im-

provements are discussed in this chapter as suggestions for future research.

Accurate phasefront reconstruction was demonstrated, with the optical path variations of the holographic plate limiting the measurement accuracy to one-half wave (λ = 351 nm) for the central 75% of the beam's area, and to one wave for the edge of the beam. Based on an accurate phasefront reconstruction and the successful application of CW, two-beam interferometry (point-diffraction and holographic interferometers) to this reconstruction, we conclude that a new technique is available for the phasefront measurement of a frequency converted HPPL. The accuracy of this technique can readily be increased by means of an improved system design that is described in the following paragraphs.

5.2   Suggestions for Future Research

Given that this technique is both promising and useful as a wavefront measurement tool, it is recommended that further development begin with necessary engineering improvements. A new holographic design, illustrated in Fig. 5-1, would incorporate several new features. The wedged beamsplitter which intercepts the HPPL beam from it's normal path should be rear surface coated; this would minimize the number of optical components, and deliver more energy to the spatial filter input aperture, thus allowing the use of filters to attenuate the reference beam. Three wedged reflectors, varying in configuration from a folded cross pattern to an open box pattern, would provide variable attenuation, by changing
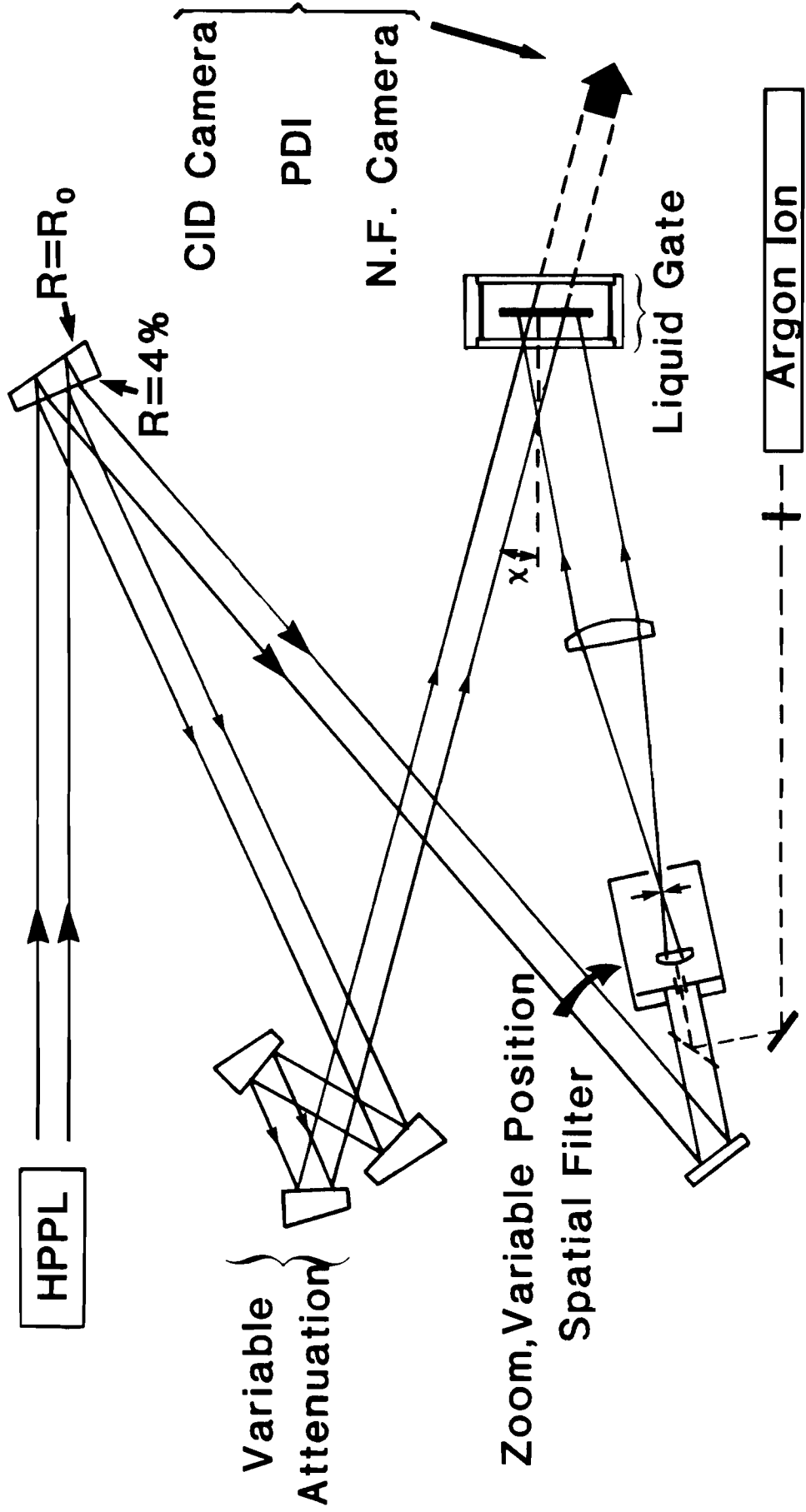
NEW HOLOGRAPHIC DESIGN

FIGURE 5-1

the Fresnel reflection coefficients, for the object beam. Variable attenuation in the object beam and the reference beam paths would provide the flexibility to choose the object-to-reference beam intensity ratio.

A system which provides a way to selectively choose and spatially filter a particular region of the original beam is needed to produce a uniform reference beam. The size and position of the region would be chosen based on the spatial frequency content of the local amplitude distribution. A combination zoom and variable position spatial filter would satisfy these requirements. The position and size of the input aperture, as well as the focal length of the objective, would be continuously adjustable, thus allowing the freedom to choose the degree of spatial filtering and the system magnification. Furthermore, the use of a liquid gate to contain the holographic plate would greatly reduce scattering, halation effects, and phase distortions, as discussed in Section 3.4., Sources of Noise. A liquid gate large enough to handle the full diameter of the beam should be designed and built.

Once the engineering modifications are made, a sensitometric approach should be taken towards each step of the holographic process. Amplitude transfer characteristic curves would be valuable in choosing a bias exposure and an object-to-reference beam intensity ratio that would optimize linear amplitude recording. Furthermore, they would provide a quantitative measure for determining the effects due to nonuniformities in the reference beam.

A final suggestion for future research involves the apparatus employed to record the reconstructed wavefront. Once the holographic plate is processed and returned to the liquid gate, further reliance on photographic methods is not necessary. Electronic detection of the wavefront,

by means of various size detector arrays, would circumvent the photographic image processing procedure. Direct digitization of a PDI interferogram, and ETP array, and possibly a demagnified near-field profile, would more readily provide quantitative capabilities. The measurement of the near-field amplitude and phase distributions and the quasi-far-field intensity distribution, together with a two-dimensional beam propagation code, would provide the means of completing the flowchart of Fig. 1-1.

In closing, the current interest in amplifying and frequency converting nanosecond, picosecond, and femtosecond lasers, where the wavefront quality is a principal concern, gives rise to an anticipation that the results from this study will encourage the use of holographic techniques in the wavefront analysis of various lasers in the high-peak-power regime.

APPENDIX A

The Image Processing System (IPS) at the Laboratory for Laser Energetics was used to digitize and intensity correct the photographic data, and to perform computer-based manipulations and statistical calculations on these images. The IPS consists of two computers and an image acquisition system. The International Imaging Systems (I^2S) apparatus includes the Video Image Processor (VIP), the Mark II digitizer, two monitors, a Sierra Minicon vidicon camera, and a light table. The I^2S is controlled by the HP-2100A computer, while the Cyber 175 computer is the host for the statistics and graphics packages.

The photographic images (density variations on transparent film) were placed on the light-table, and processed by converting the light transmitted through the film to the vidicon tube into digital values. The VIP acquired the image, while the digitizer converted the transmitted intensity into digital value. The HP-2100A transferred the digital image to magnetic tape, which was subsequently read onto disc memory at the Cyber 175. Vidicon and film calibration curves were generated at the Cyber in order to intensity correct experimental data that was in digital form. Figures A-1 and A-2 represent the Aerographic (4421) ultraviolet (λ = 351nm) film calibration curves for pulsewidths of approximately one nanosecond and one second, respectively.

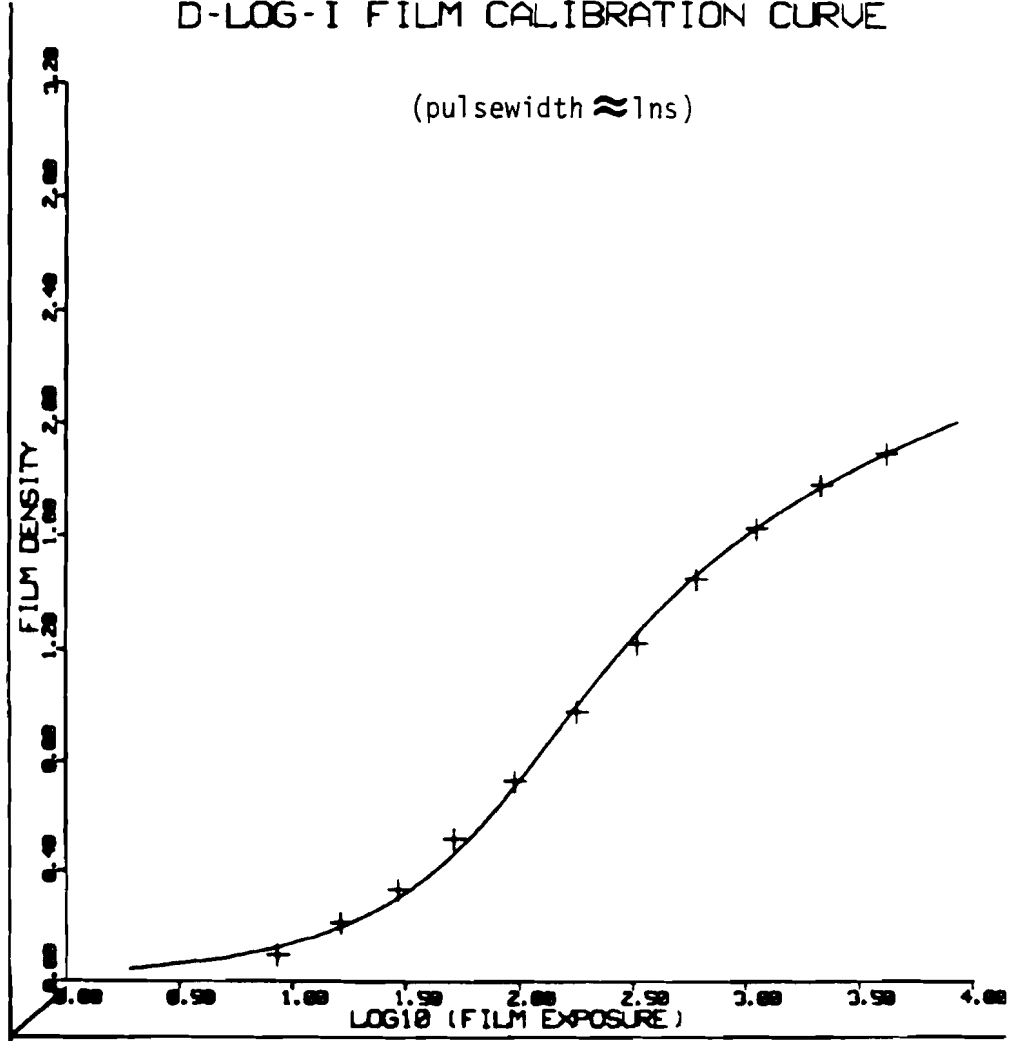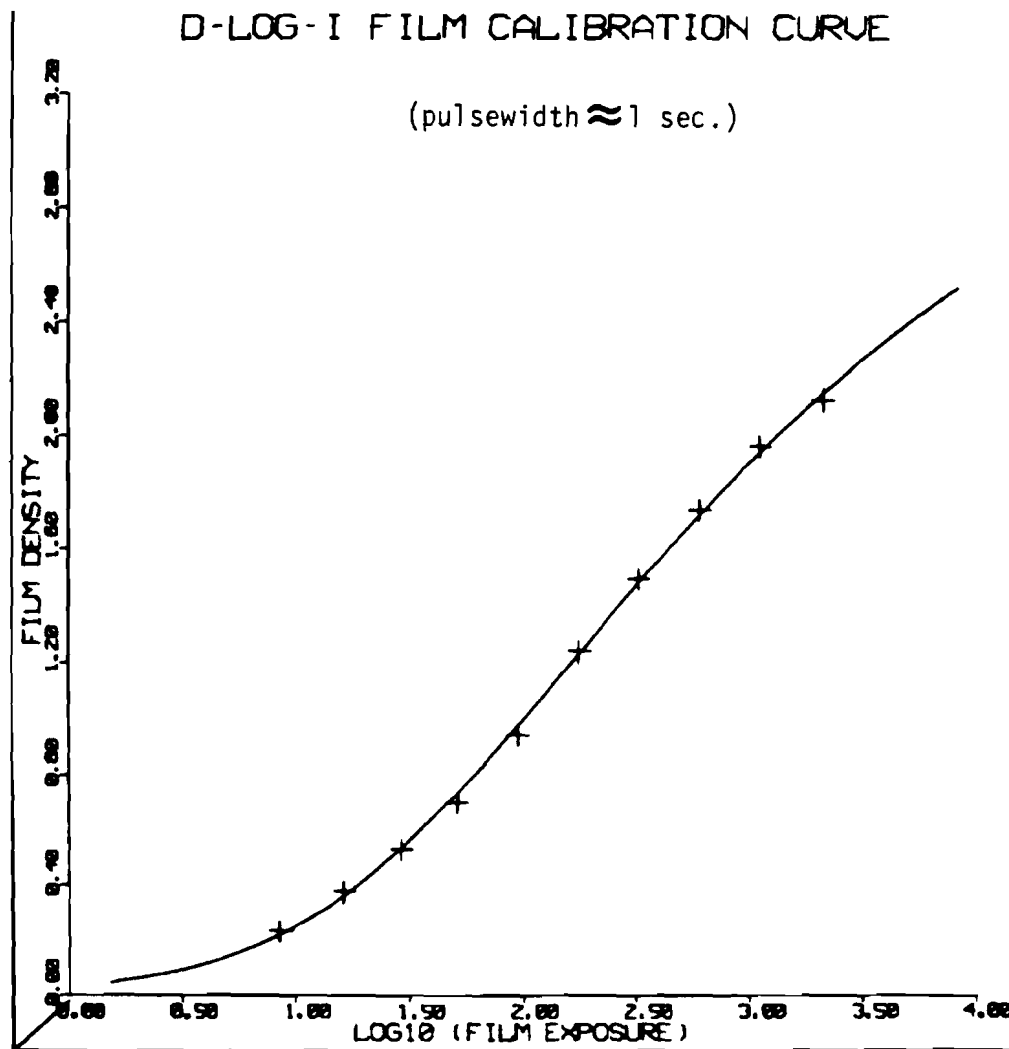# D-LOG-I FILM CALIBRATION CURVE

(pulsewidth ≈ 1ns)

FIG. A-1

D-LOG-I FILM CALIBRATION CURVE

(pulsewidth ≈ 1 sec.)

FIG. A-2

APPENDIX B

I. Aerographic (4421) Film Processing (20-21°C)

    a) Presoak in Kodak Photoflo 2000   - 30 sec.

    b) Develop in Kodak DK-50 with continuous   - 3½ min.
       agitation

    c) Stop in running water   - 45 sec.

    d) Fix in Kodak General Purpose Fixer with   - 5 min.
       continuous agitation

    e) Rinse with running water   - 2 min.

    f) Wash in Heico Perma Wash   - 1 min.

    g) Rinse with running water   - 2 min.

    h) Squeegee dry

    i) Heater dry

II.   Agfa-Gevaert 10E56 Plate Processing (20-21°C)

   a)   Develop in D-19 with continuous nitrogen   - 5 min.
        bursts

   b)   Stop in Kodak indicator stop bath with   - 30 sec.
        continuous nitrogen bursts

   c)   Fix in Kodak General Purpose Fixer with   - 5 min.
        continuous nitrogen bursts

   d)   Rinse in running water   - 2 min.

   e)   Wash in Heico Perma Wash   - 1 min.

   f)   Rinse in running water   - 2 min.

   g)   Compressed air dry

(Bleaching)*

   h)   Cupric-halide bleach   - time to clear plus 2 min.

   i)   Wash in running deionized water   - 5 min.

   j)   50% ethyl alcohol (agitate)   - 2 min.
        50% deionized water

   k)   75% ethyl alcohol (agitate)   - 2 min.
        25% deionized water

   l)   90% ethyl alcohol (agitate)   - 2 min.
        10% deionized water

   m)   Dry

* Reference: Pennington and Harper
             Applied Optics, July 1970
             Vol.9-#7, p. 1645